Development of a laser ion source at ALTO : Production of Ga and Ag beams

Anahí Segovia Miranda

Anahí Segovia Miranda. Development of a laser ion source at ALTO : Production of Ga and Ag beams. Nuclear Experiment [nucl-ex]. Université Paris-Saclay, 2023. English. NNT : 2023UPASP065 . tel-04210639

HAL Id: tel-04210639
https://theses.hal.science/tel-04210639v1

Submitted on 19 Sep 2023

Development of a laser ion source at ALTO : Production of Ga and Ag beams.

Développement d'une source d'ions laser à ALTO : Production de faisceaux de Ga et Ag

Thèse de doctorat de l'université Paris-Saclay

École doctorale n°576 Particules, Hadrons, Énergie et Noyau : Instrumentation, Imagerie, Cosmos et Simulation (PHENIICS)
Spécialité de doctorat : Physique Nucléaire
Graduate School : Physique, Référent : Faculté des sciences d'Orsay

Thèse préparée dans l'unité(s) de recherche : **IJCLab (Université Paris-Saclay, CNRS)** , sous la direction de **François LE BLANC**, directeur de recherche, la co-direction de **Carole GAULARD**, Maître de conférences.

Thèse soutenue à Paris-Saclay, le 28 Juin 2023, par

Anahí SEGOVIA MIRANDA

Composition du jury

Membres du jury avec voix délibérative

Amel KORICHI Directrice de Recherche, Université Paris-Saclay IJCLab, Orsay	Présidente
Pierre DELAHAYE Directeur de Recherche, Université Caen Normandie GANIL, Caen	Rapporteur & Examinateur
Xavier FLÉCHARD Directeur de Recherche, Université Caen Normandie LPC, Caen	Rapporteur & Examinateur
Thomas COCOLIOS Assistant Professeur, Université de KU Leuven	Examinateur

THESE DE DOCTORAT

NNT : 2023UPASP065

université
PARIS-SACLAY

ÉCOLE DOCTORALE
Particules, hadrons, énergie et noyau :
instrumentation, imagerie, cosmos
et simulation (PHENIICS)

Titre : Développement d'une source d'ions laser à ALTO : Production de faisceaux de Ga et Ag.

Mots clés : Physique des lasers, Ionisation résonnante par laser, Séparation isotopique, Noyaux exotiques, production d'ions, Ag, Ga.

Résumé : Cette thèse décrit le développement et l'upgrade de RIALTO, la source d'ions laser par ionisation résonante (RILIS), au sein de l'installation ALTO. RIALTO vise à produire des faisceaux d'ions purs en utilisant la technique d'ionisation résonnante (RIS), grâce à un processus d'excitation laser en plusieurs étapes. Le laboratoire laser est équipé de deux lasers Nd :YAG haute puissance fonctionnant à 10 kHz et pompant trois lasers colorants (540-850 nm), dont deux de Radiant Dyes et un de Lioptec. Ces lasers sont couplés à des cristaux BBO (270-425 nm), permettant le doublage en fréquence du 1er étage pour obtenir des schémas d'ionisation en deux et trois étapes. De plus, un banc de test hors ligne (ABU pour Atomic Beam Unit) est installé pour déterminer les paramètres opérationnels optimaux d'une utilisation en ligne avec un faisceau radioactif. L'ABU a été utilisé pour déterminer les paramètres opérationnels optimaux et le schéma d'ionisation laser pour la production d'argent selon un schéma en 3 étapes et 3 couleurs. Le système RIALTO amélioré permet la production simultanée de deux schémas d'éléments différents, ce qui a permis de générer avec succès des faisceaux stables de Ga et d'Ag. Ce travail comprend également des mesures de production d'ionisation laser de Ga radioactif, comparées aux estimations initiales, fournissant des informations précieuses sur les performances du système développé.

Title : Development of a laser ion source at ALTO : Production of Ga and Ag beams.

Keywords : Physics of lasers, ion production, Resonance Ionisation Spectroscopy, isotopic separation, exotic Nuclei, Ag, Ga.

Abstract : This doctoral thesis describes the development of RIALTO, the Resonant Ionization Laser Ion Source (RILIS), at the ALTO facility. RIALTO aims to produce pure ion beams using the resonance ionization technique (RIS), using a multi-step laser excitation process. The laser laboratory is equipped with two high-power Nd :YAG operating at 10 kHz and pumping three (540–850 nm) dye lasers, two from Radiant Dyes and one from Lioptec ; these lasers are coupled with BBO doubling units (270–425 nm), this laser system allows us to achieve two and three-step ionization schemes. Additionally, an atomic beam unit (ABU) is incorporated into the setup to determine optimal operational parameters for online operation with a radioactive beam. The ABU was used to determine the optimal operational parameters and laser ionization scheme for producing silver with a 3-step-3 color scheme. The upgraded RIALTO system enables the simultaneous production of two different element schemes, leading to the successful generation of stable Ga and Ag beams. This work also includes measurements of the laser ionization production of radioactive Ga, which are compared with the initial estimations, providing valuable insights.

Remerciements

Doing a PhD is complicated. Doing a PhD as a foreigner, in a country where you don't speak the language or know the culture, is even more challenging. Now, on top of this, add a global pandemic and an economic and political crisis... that's what I had to go through to be able to reach this day when I'm publishing this thesis.
In the following pages, as my work unfolds, it's important to remember that its achievements are not mine alone. They are the collective results of collaboration, guidance, and shared enthusiasm. Many people have been part of my journey, both in academia and in my general life, who helped me get through this time. I want to take this moment to try to thank them for their contribution to my academic, professional, and personal growth.

[Speaks french in spanish]

Tout d'abord, je tiens à exprimer ma gratitude envers les membres du jury. Vos retours éclairés et vos évaluations critiques ont été cruciaux pour améliorer la qualité de ce travail. Amel, pour avoir présidé ma soutenance de thèse, Pierre et Xavier, pour avoir lu mon travail et apporté votre expertise et vos perspectives au processus d'évaluation, notamment en rédigeant un rapport sur mon travail en si peu de temps. Et Thomas, pour les commentaires et questions qui ont suscité des discussions intéressantes.

Chaque doctorant a un directeur et je n'aurais pas pu trouver meilleur. Un grand merci à François, sans toi, cette aventure n'aurait jamais commencé. Merci de m'avoir fait confiance pour développer une source d'ions laser pour un laboratoire de physique nucléaire, à moi qui ne savais rien des lasers ni de physique nucléaire. Merci pour tout ton soutien, à la fois dans mon parcours académique et dans mon intégration au laboratoire et à la vie française. Je te suis extrêmement reconnaissante d'avoir retrouvé la bouteille que j'ai jetée à la mer.

Carole, ma co-directrice, nous avons commencé cette thèse avec l'idée d'étudier les propriétés magnétiques et de faire de moi une experte en cryogénie, mais nous avons fini par plonger dans l'administration et la bureaucratie française. Maintenant, tu es une experte en paperasse. Merci d'avoir toujours gardé ta porte ouverte. Je sais que je ne la franchissais que rarement et que c'était toi qui venais me chercher. Tu as toujours eu confiance en moi quand je doutais, et tes paroles justes m'ont souvent évité de m'égarer.

Je tiens à exprimer ma gratitude envers la direction d'IJCLab, Fadi, Achille, et Sébastien, pour leur soutien. De plus, je souhaite adresser mes remerciements à David, pour son accueil chaleureux au sein du pôle nucleaire et de l'école doctorale, ainsi que pour sa disponibilité constante à répondre à mes questions. Son aide s'est avérée particulièrement précieuse pour obtenir une extension de temps, qui s'est révélée essentielle pour la conclusion de ma thèse.

Un grand merci à tous les membres du groupe ex-NESTER, qui ont directement ou indirectement contribué à ce travail et rendu mon temps au laboratoire infiniment enrichissant. Merci, Céline, d'avoir toujours un sourire et d'avoir fait du laboratoire un endroit chaleureux. Enfin, un remerciement chaleureux à toute l'ensemble du personnel d'ALTO, qui a soutenu la concrétisation de ce projet, en particulier à Florian, pour son aide à l'alignement des lasers et sa disponibilité pour tous les balayages de masse.

Vladimir, I greatly appreciate all your support, your patience, and all your help. Thank you very much for taking the time to explain carefully every time I had a question, and for explaining again when you could see from my face that I hadn't understood. Thank you for the time you spent helping me with experiments, collecting data, analyzing and interpreting results, and also for listening when I needed to vent my emotions. I'm very grateful for having crossed paths with you during my academic career.

To my PhD colleagues, this journey wouldn't have been the same without you. Having someone to talk to, someone going through the same experiences, who understands what you're feeling, is extremely important. Thank you to those who shared an office with me: Rémy, Louis, Guillem – vous avez été patients et m'avez aidé à améliorer mon français de tous les jours. Then came Wenling, always with a smile despite tough times, and eventually Emile, merci de m'avoir aidé à mettre en place COeCO, même si nous n'avons pas finalement réalisé l'expérience, et pour toute ton aide avec root. Alessandro et Masyl, avec qui je pouvais toujours me confier, Damien, qui me sortait pour jouer à Pokémon, Sarah, je te suis reconnaissante pour tous les moments partagés autour d'un café, lors des expositions, et au fil de nos conversations chaleureuses, merci d'être une formidable amie. And to all the newcomers and interns who I couldn't spend much time with due to intense writing, yet you always invited me for coffee or pizza.

Quiero agradecer a todos mis amigos tanto a los que están cerca como a los lejos. A mi familia parisina, muchas gracias a todos por ayudarme con la integración a un nuevo país por hacerme sentir en casa estando tan lejos, por entender lo que significa ser migrante. Muchas gracias a mis amigos en México, que han mantenido la comunicación y el apoyo a pesar de la distancia, por estar ahí en las madrugadas porque para ustedes es la hora de comer.

Special thanks to my best friend in the whole world and the entire universe, Sarah. Thank you so much for all your caring packages, for being so present in my life regardless of distance or time, for your kindness.

El agradecimiento más grande es para mi familia. Papás, yo sé que a veces no entienden lo que estoy haciendo, pero siempre me han apoyado, no importa qué. Y gracias a ustedes he llegado hasta donde estoy, muchas gracias por nunca cortarme las alas y apoyarme a emprender vuelo. Ednna, muchas gracias por todo el esfuerzo que haces por ayudarme con mi salud mental y emocional a la distancia, por siempre estar ahí como pilar y nunca dejarme sola. Emmanuel, muchas gracias por haber venido a hacerme compañía cuando más lo necesitaba, justo antes de defender la tesis. No sé qué hubiera hecho si no hubieras estado allí. Y finalmente, muchas gracias a mis hermosos sobrinos, Miranda y Sebastián, que ayudaron a decorar mi oficina con sus cartitas y dibujos. Gracias a ellos, pude mantenerme calientito el corazón durante todo el doctorado. Muchas gracias familia, no habría logrado llegar tan lejos sin su amor incondicional y todo su apoyo desde el día en que nací.

Just in case I forget someone or if your name is not in there, it does not mean you were not an important part of my journey, or my life, but I would need to make another thesis just to name all the people around me and how, whether direct or indirect, have shaped my experiences and have ultimately culminated in the completion of this thesis.

Muchas gracias a todos.
[Cries in spanish]

Contents

List of Figures

List of Tables

Chapter 1

Introduction

Physics is a cornerstone of humanity's never-ending pursuit of complete knowledge. It has provided groundbreaking discoveries, theories, and predictions that have led to more complex questions. Over the last century, atomic, nuclear, and particle physics have become some of the most critical fields within the discipline, even though they focus on microscopic objects and their effects. Nonetheless, the progress and discoveries in these fields have far-reaching consequences that have changed our lives and perception of the world. Although chemists have studied matter since the 18th century, the concept of the atom as the fundamental constituent of matter only emerged in the early 19th century. Henri Becquerel's study of the fluorescence of uranium salts led him to the accidental discovery of radioactivity in 1886 by observing the radiation emitted by it. Marie Curie later conducted her doctoral thesis on radioactivity, discovering other radioactive elements such as polonium and radium. In 1903, Henri Becquerel, Marie Curie, and Pierre Curie were jointly awarded the Nobel Prize in Physics for discovering spontaneous radioactivity. Ernest Rutherford also researched radioactivity and identified that uranium produced two types of radiation: alpha and beta. He inferred that a substantial amount of energy is released during a disintegration and that the nature of the elements involved is modified. He received the Nobel Prize in Chemistry in 1908 for his work on alpha radiation. In 1909, Rutherford conducted scattering experiments that led him to develop the first atom model, which predicted a small, positively charged nucleus in the center of the atom, surrounded by negatively charged electrons on planetary orbits. Eventually, this model became the basis for the Bohr model, which included the first quantum mechanical interpretations. In 1911, he postulated that the atom must have a nucleus at its center that contains the majority of its mass and positive charge, leading to the birth of nuclear physics and the study of the properties of the nucleus.

Today we know that the nucleus is not indivisible and that it is composed of two types of nucleons: protons and neutrons. Protons have a positive charge, and neutrons are electrically neutral. We can go even further, the nucleons being themselves composed of quarks which are studied in particle physics. Its notation is designated by ^{A}X, where A is the mass number equal to the sum of protons and neutrons, A = Z protons + N neutrons, and X is the element determined by the number of protons. For example, a nucleus with 6 protons is a carbon nucleus, but there are several different carbons: ^{12}C with 6 neutrons, ^{14}C with 8 neutrons, etc. Nuclei with the same number of protons but varying numbers of neutrons are called isotopes.

To date, 118 different chemical elements and more than 3000 nuclides have been discovered [1]. The nuclear chart represents the nuclides by their number of protons on the ordinate and neutrons on the abscissa (Fig.1.1). The valley of stability, located in the chart's center, contains all the nuclei that do not disintegrate and can be found on Earth. About 80 of these elements have stable isotopes, while the remaining isotopes are unstable and are produced in nuclear reactions. These unstable nuclei are referred to as exotic nuclei and have a limited lifespan before decay. Those with excess protons or neutrons that lack sufficient binding energy to maintain their cohesion are classified as the limit of stability or drip line.

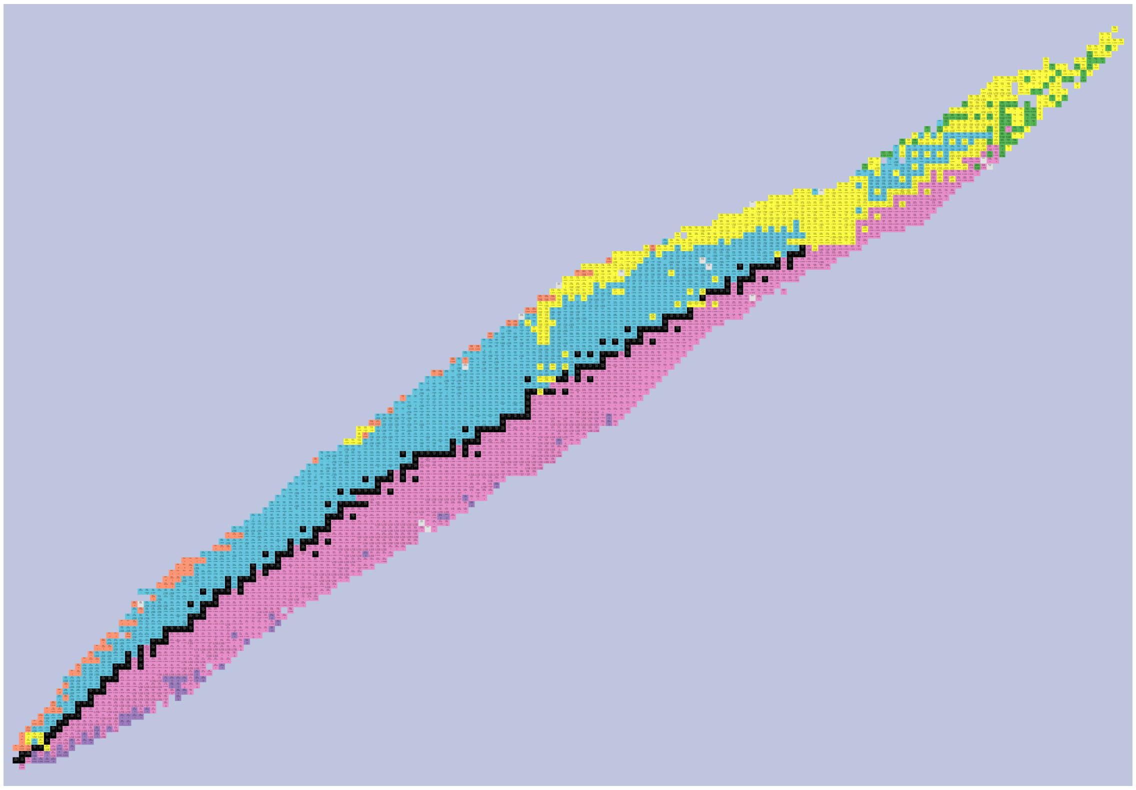

Figure 1.1: Chart of nuclides plotted with atomic number (Z) versus neutron number (N), with stable species indicated by black squares. The colors correspond to primary decay modes α (yellow), β+/EC (blue), and β- (pink). Neutron emission (purple), proton emission (orange), and spontaneous fission (green).

Nuclear and atomic physics research have made remarkable progress in recent years, resulting in significant breakthroughs such as lasers, nuclear fission, and an understanding of the fusion processes in stars. Nevertheless, these advancements have also brought new challenges, including understanding the creation of matter and the universe's formation. To address these challenges, nuclear and atomic physicists study the properties and interactions of atoms and particles, including their mass, radius, half-life, decay modes, and electromagnetic moments. This understanding is crucial in comprehending the formation of elements through various nucleosynthesis processes, which requires experiments on both stable and radioactive nuclides, including the most short-lived exotic species near the drip line.

The use of radioactive isotopes has been essential in nuclear physics research and has found many applications in various scientific fields. However, most radioisotopes are not naturally occurring, and specialized facilities such as Radioactive Ion Beams (RIB) have been established worldwide to produce these nuclides, including short-lived exotic ones. Recent developments in RIB technology have led to the exploration of isotopes with a proton-to-neutron ratio very different from stable isotopes in an unprecedented way. Nonetheless, producing these exotic nuclei is challenging, primarily due to low production cross-sections, overwhelming production of unwanted species in the same reaction, and very short half-lives.

Two complementary methods for producing high-quality RIBs have been developed: the isotope separation on-line (ISOL) technique and the in-flight separation technique. Both techniques transport the nuclei of interest to a well-shielded experimental setup where nuclear properties can be studied. During the transport process, the beam is purified and prepared to meet the requirements of different experiments. The final aim is to produce intense and pure beams of exotic nuclei with good ion optical quality, proper timing characteristics, and energies ranging from essentially rest (meV u^{-1}) to the highest energies (GeV u^{-1}) [2]. A more detailed description of the ISOL method is given in Chapter 2.

Achieving intense and pure RIBs requires a high production rate, efficiency, speed, and selectivity production sequence. The beam-target combination and beam energy must be optimized to attain the highest production rate of a specific nucleus. Any manipulation of the reaction products must be efficient, preferably close to 100%. Losses due to radioactive decay between production and arrival at the experimental setup should be minimal since one deal with short-lived exotic nuclei. The separation process should also effectively reduce the unwanted species and primary beam, as the isotopes of interest often form a minority in the nuclear reaction process.

Figure 1.2 gives an overview of existing ISOL and In-flight facilities and facilities in planning or construction.

Figure 1.2: Radioactive ion beams (RIB) facilities around the world [3].

ISOL facilities rely on converting reaction products to ions, extracting them as an ion beam, and filtering this ion beam downstream of the target and ion source assembly using an electromagnetic spectrometer. However, this process alone cannot ensure an isotopically pure ion beam for the experiment because of the presence of isobars (nuclear mass ambiguity) in the admixture of reaction products. In many cases, the isotopes of interest have lower yields than neighboring isobars, making it difficult to suppress isobaric contamination using magnetic separators' resolving power. Various beam purification techniques have been employed to address this problem, such as high-resolution magnetic separators (HRS), multi-reflection time-of-flight mass separators (MR-TOF-MS), and Penning traps (PT) [4]. Still, laser resonance ionization is considered an optimal technique for achieving isotopically pure ion beams due to its efficiency, speed, and complete element selectivity.

Various laser-based methods have been developed since the invention of lasers. They have been key in expanding our understanding of nuclear matter and have been utilized in various scientific fields. Notably, they are used to extract properties of nuclei, such as nuclear spins, magnetic dipole moments, electric quadrupole moments, and charge radii. Laser spectroscopy, which takes advantage of laser radiation's high spectral brightness and wavelength tunability to selectively excite quantum transitions in atoms and molecules, has been one of the earliest applications of lasers. The resonance interaction in laser spectroscopy also plays a significant role in the ionization of atoms. This technique provides exceptional capabilities for the spectroscopy of short-lived isotopes and manipulation with radioactive ion beams.

Laser-based techniques, such as collinear laser spectroscopy [5], in-source laser spectroscopy [6], and trap-assisted laser spectroscopy [7], are commonly used to study exotic isotopes at radioactive ion beam facilities. The sensitivity and resolution of these techniques are the main factors determining their applicability in different regions of the nuclear chart.

At on-line facilities, laser spectroscopic data is predominantly obtained using two complementary techniques: collinear laser spectroscopy (CLS) [8, 5] and resonance ionization (mass) spectroscopy (RIS/RIMS) [9, 10]. While CLS provides higher resolution, RIS/RIMS offers higher sensitivity. However, the sensitivity of CLS can be increased with particle detection, and RIS/RIMS can offer high resolution with continuous wave lasers. Mixed forms of CLS/RIS have also been demonstrated [11]. Laser spectroscopy is a valuable tool for extracting accurate experimental data on the properties of nuclear ground states and isomers without relying on a nuclear model.

Apart from being a tool of nuclear-structure physics, the described methods of laser spectroscopy have been applied to prepare beams and atomic samples. These applications include ion source development and the polarization of electronic and nuclear spins. Also, laser cooling and conventional storage techniques are involved in new experiments addressing fundamental aspects of the nuclear beta-decay.

This work will focus only on the resonance ionization process and its application to producing radioactive beams. A brief historical overview of the development of the method is given below, and a more detailed description of the process will be given in Chapter 3.

In 1971, Ambartzumian and Letokhov first demonstrated multi-step resonance photoionization through the two-step ionization of rubidium [12]. This led to the development and study of multi-step laser resonance ionization by numerous laboratories in the following years. In 1983, Alkhazov et al. applied this highly sensitive technique for the first time at the ISOL facility in Gatchina, Russia, creating the first operational resonant ionization laser ion source (RILIS) system at the IRIS laboratory in the Leningrad Nuclear Physics Institute (LNPI) [13]. Since then, RILIS has become a leading method in optical spectroscopic research on radioactive isotopes. RILIS is widely used as a laser ion source at ISOL facilities due to its efficiency and selectivity in achieving high radioactive ion beam purity without sacrificing isotope yield. Mass separation alone cannot distinguish between isobars, making element-selective ionization necessary. Additionally, performing element selection at the ion source location can help prevent the propagation of unwanted radioactivity downstream of the target assembly. This is especially important for ISOL facilities that use high-power targets. As a result of its effectiveness, RILIS is now a well-established technique at many of the world's leading on-line ion source facilities.

To implement a laser ion source at each facility, specific technical requirements and design constraints must be considered, including the type of RIB facility, the location, geometry, and environment of the laser/atom interaction region, and the minimum requirements for the laser system, such as pulse energy, repetition rate, and beam quality. The main requirements of a laser ion source for on-line applications are universality, selectivity, efficiency, reliability, and rapidity [14].

Two successful methods are used based on the front-end conditions of the target and mass separator:

- laser ionization of free atoms at low pressure in a hot cavity
- laser ionization in a cell filled with a buffer gas

The hot cavity RILIS principle, which uses a high-temperature surface ion source cavity as a laser interaction region, was successfully developed at the IRIS facility [13]. This approach is simple, robust, and effective because the atoms are confined inside a narrow tube while effusing from the target and transfer line. The cavity's dimensions (typically 3 mm diameter, 30 mm length) permit high ionization efficiency and fast atom transport, making it suitable for producing beams of short-lived isotopes [15]. The standard cavity is a resistively heated refractory metal (W, Ta, Re) or graphite tube. It helps the RILIS process by creating a confining plasma potential for the laser ions, reducing the likelihood of neutralization by wall collisions during their drift toward the extraction electrode. Despite its simplicity, reliability, and high efficiency, the hot cavity approach has a drawback because the competing surface ionization process greatly disturbs the purity of the resulting ion beam for many isotopes.

The laser ion source in a gas cell operates on an element-selective resonance multi-step laser ionization principle. Neutral atoms, produced in a nuclear reaction, are thermalized and neutralized in a buffer gas where the primary accelerator beam, recoil ions, and radioactivity create weak plasma. This method was developed at KU Leuven in the early 1990s [16, 17, 18]. The gas flow determines the extraction time of radioactive isotopes from the gas-cell-based ion source and is considerably shorter (up to 10 ms) compared to the global release time for a system using a hot cavity ion source. Additionally, the gas cell ion source does not rely on the chemical properties of extracted atoms, making it particularly useful for refractory atoms.

Figure 1.3 summarizes the RILIS facilities currently or are planned worldwide at RIB (Radioactive Ion Beam) facilities. With the exception of the FURIOS ion source at the IGISOL facility in Finland, GISELE within S3-LEB at GANIL, and the PALIS and KISS system in Japan, which uses a buffer gas-filled stopping cell, the remaining LIS are based on a hot-cavity source.

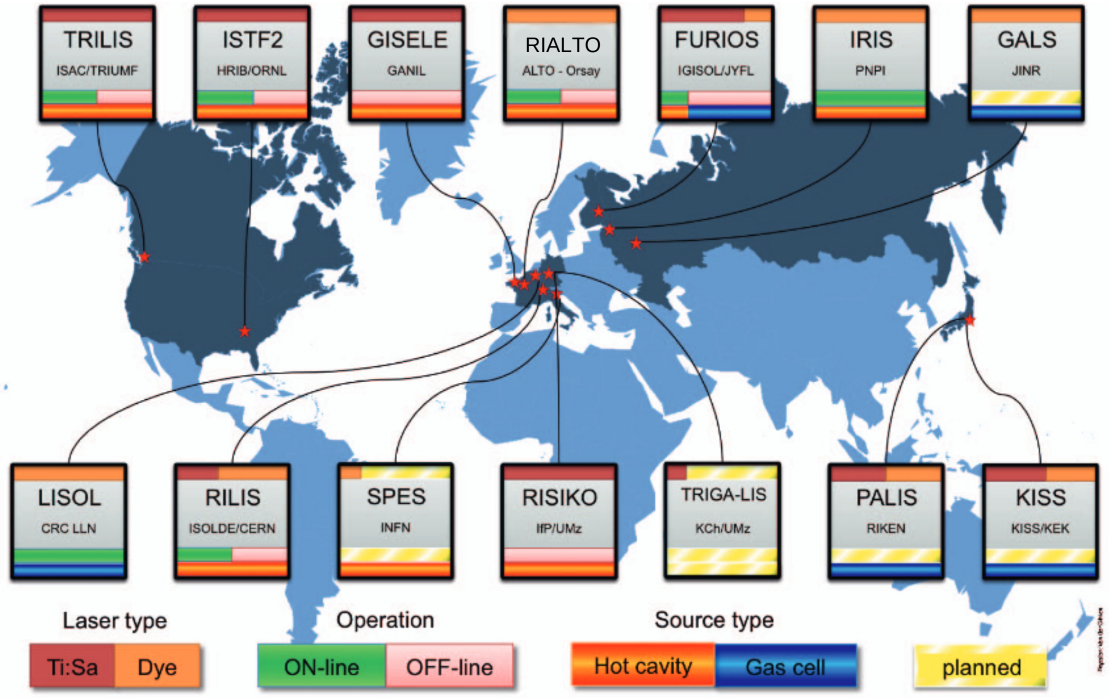

Figure 1.3: Existing and planned resonance laser ion sources worldwide [19].

Laser spectroscopy techniques have been extensively utilized to investigate over one thousand isotopes and isomers out of the roughly three thousand species generated at Radioactive Ion Beam facilities. Figure 1.4 shows a nuclear chart with all radioactive isotopes studied with laser spectroscopy at on-line facilities – and in a few cases off-line – to extract properties of the nuclear ground state or sufficiently long-lived isomers. These measurements have played an essential and irreplaceable role in studying the nuclear structure and inter-nucleon interactions, leading to significant scientific breakthroughs.

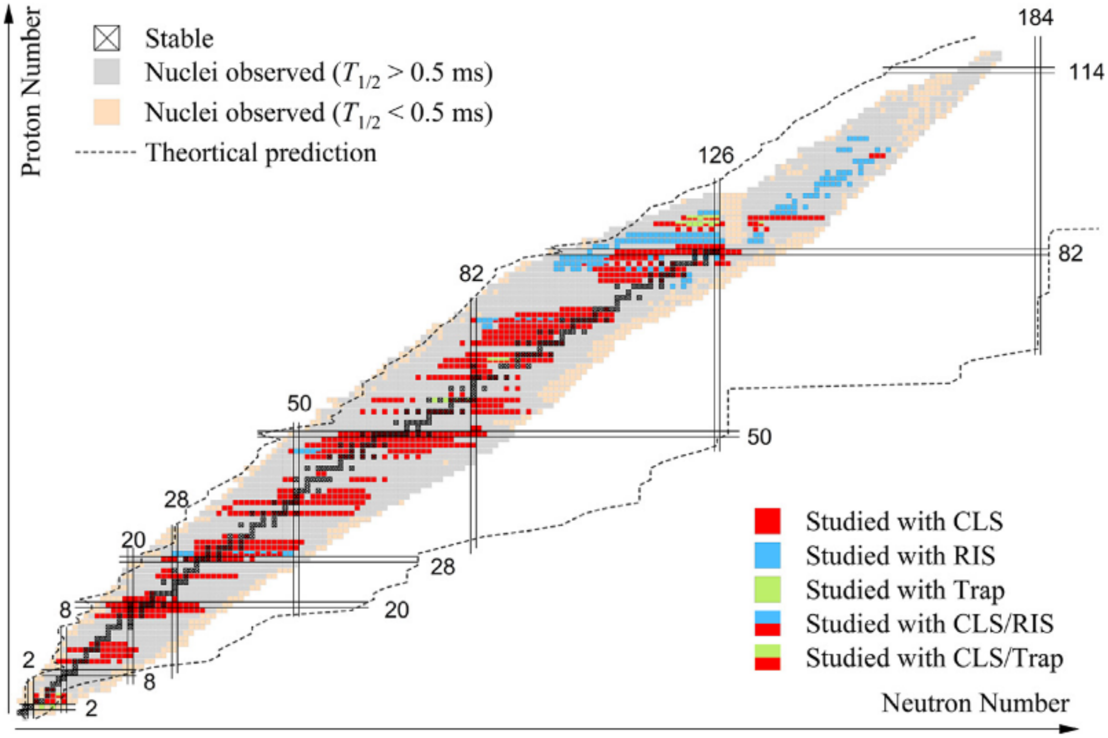

Figure 1.4: The chart of nuclides showing the radioactive ion beams resonantly ionized and mass separated at isotope separator facilities worldwide [20]. The nuclei studied by laser spectroscopy experiments are indicated with color squares depending on the technique employed, red, collinear laser spectroscopy (CLS), blue, resonance ionization spectroscopy (RIS), and green, in-trap studies.

ALTO (Accélérateur Linéaire et Tandem d'Orsay) is an ISOL facility that produces neutron-rich radioactive ion beams (RIB) from the interaction of a gamma flux created by a 50 MeV electron beam in a uranium carbide target (photofission) [21]. A magnetic dipole mass separator (PARRNe) and a resonance ionization laser ion source (RIALTO) allow the selection of the ions of interest. The "cold" nature of photofission allows producing exotic neutron-rich species of superior isobaric purity compared to the contaminant products of proton spallation. Despite the electron-induced fission fragments at ALTO, a nonselective ion source would still lead to significant isobaric contamination, which can hamper the experiments. To get a unique selection, we use a multi-step laser excitation process to excite the element of interest resonantly, each laser wavelength corresponding to an atomic level gap. The selection in Z is thus maximum, eliminating all but the residual isobaric contamination surface ionized by the hot cavity surfaces.

Chapter 2 provides an overview of radioactive ion beam (RIB) production through the ISOL (Isotope Separation On-Line) method and introduces the ALTO (Accelerateur Lineaire et Tandem d'Orsay) platform. Chapter 3 focuses on the RILIS (Resonant Ionization Laser Ion Source) method and discusses the RIALTO (Resonance Ionization Laser Ion Source of ALTO) laser system and its limitations. Chapter 4 details the upgrade of the laser system at the RIALTO laser laboratory and the commissioning using a Ga beam. Chapter 5 concentrates on the development of a silver beam using the laser ion source. Chapter 6 describes the production measurements for radioactive Ga, including the experimental setup and analysis procedures. Finally, Chapter 7 concludes the thesis work, summarizing the key findings and conclusions and offering an outlook for future research.

Chapter 2

Radioactive ion beams

Studying exotic nuclei (i.e., short-lived isotopes with far-off β-stability and extremely unbalanced proton-to-neutron number ratios -differs substantially from unity- on both the proton and neutron-rich sides of stability) allows us to understand the behavior of hadronic matter under extreme conditions. Radioactive ion beams (RIB) are an extraordinary tool in modern nuclear physics and provide a unique opportunity to study these nuclei.

A wide range of nuclear studies (e.g., nuclear structure, nucleosynthesis processes, etc.) depends on the availability of RIB. Their production is complex due to the low production cross sections and intensities, several orders of magnitude lower than for stable isotopes. The exotic nuclei must be effectively and efficiently separated from widely produced nuclei closer to stability. The non-selective production leads to contamination of the RIB, decreasing the experiments' reliability.

Different projectiles (protons, neutrons, heavy ions) and a wide variety of nuclear reactions, including fission, spallation, fragmentation (target, projectile), fusion evaporation, and deep inelastic collisions, are used to produce RIB. The need to select and separate the species of interest has led to two complementary approaches to producing an intense, energetic, radioactive beam: The in-flight method [22] and the Isotope Separator On-line (ISOL) technique (section 2.1). In the first one, a high-intensity heavy beam bombards a thin target. The second technique is used in this work and will be described in the next section.

2.1 ISOL method

The ISOL technique is a method of production of radioactive ion beams used at several facilities in the world, including ALTO, such as ISOLDE (CERN, Switzerland) [23], ISAC (TRIUMF, Canada) [24], SPIRAL (GANIL, France) [25], IGISOL (University of Jyväskyla, Finland) [26] and SPES (INFN, Italy) [27].

The ISOL method aims to produce a large number of exotic nuclei and select them with an excellent resolution to provide a high level of purity, then transport them to the experiments to study their properties [28].

The method consists in bombarding a thick target with a high-intensity primary beam with enough energy to induce nuclear reactions that produce radioactive atoms. The target is heated at temperatures ($> 2000\,°\mathrm{C}$) to enhance the diffusion and extraction of the radioactive atoms (the target must be porous enough to enable rapid diffusion and dense enough to optimize the luminosity of the reaction of interest). These radioactive atoms effuse from the target cavity towards the ion source, where they are ionized and then accelerated to create a beam of a few 10 keV. Finally, they are sent to a mass separator to form an isobaric beam that can be directly used in low-energy experiments.

Thick targets provide a significant advantage in ion production thanks to their capability to integrate cross-sections over a wide range of energy and angles, which increases the probability of producing ions through different reaction channels, such as spallation, fragmentation, and fission (Fig. 2.1). In contrast, ISOL facilities that use neutrons as an impinging beam result in a lower cross-section but a higher beam purity. However, producing high beam purity in ISOL is generally challenging, as it involves the simultaneous production of

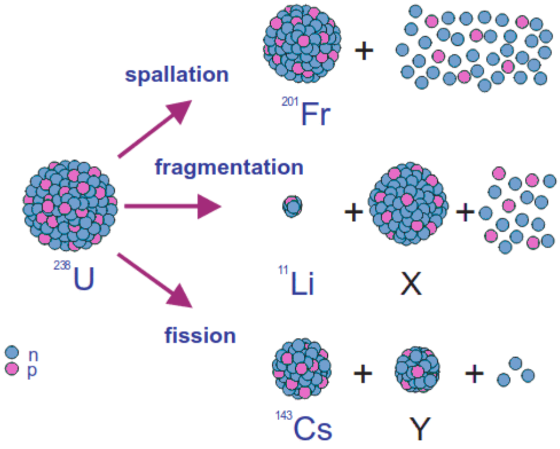

Figure 2.1: Main nuclear reactions for ion beam production in the ISOL technique. Image adapted from [29].

many isobars of different elements in the target. Achieving high beam purity also requires optimizing target material, driver beam energy, and ion source design, among other factors.

Depending on the target thickness, the ISOL method can provide high production yields and produce ion beams with good optical quality. However, short-lived isotopes might not be released because of the slow process by which the elements diffuse from the target. This technique is highly dependent on the chemistry between the reaction's products and the atoms constituting the target. For this reason, certain elements are not accessible, which is the case of refractory or chemically active elements with an evaporation temperature higher than the maximum temperature at which the target can be heated.

2.1.1 Ionization methods

Producing radioactive ion beams requires highly efficient, selective, and fast ion sources to minimize isobar contamination and decay losses of short-lived isotopes. For RIBs produced by the ISOL method, ion sources must operate steadily for extended periods in a high radiation area and at high temperatures ($> 2000\,°\mathrm{C}$).

The ionization method is highly dependent upon the chemical property of each element, such as its volatility and, most importantly, its ionization potential (IP). Figure 2.2 shows the most commonly used ionization methods; surface ionization, electron impact (plasma) ionization, and laser resonant ionization.

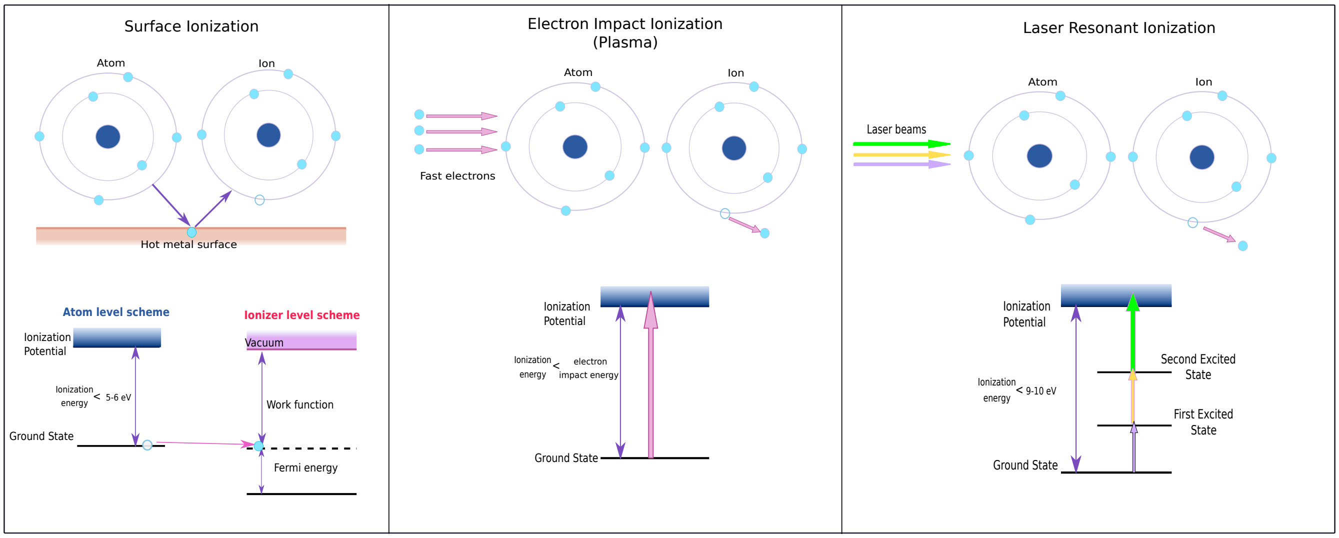

Figure 2.2: Ionization methods. Schematic representation of surface ionization, electron impact ionization (plasma ionization), and resonant photoionization.

Surface ionization is a highly effective method of ionizing elements with ionization potentials below or about equal to the work function of a metal surface, which serves as the hot ionizer. This technique is commonly employed in ISOL facilities to produce RIB's [15, 30, 31]. Surface ionization occurs when an atom with low ionization potential impacts a hot surface of a material with a high work function, such as a noble metal. This interaction significantly increases the probability of electron transfer from the atom to the metal surface, resulting in the atom's ionization. This process is temperature-dependent, particularly the surface temperature, as higher surface temperatures directly impact the thermal energy of atoms, increasing the probability of collisions between atoms and the surface. This facilitates the transfer of electrons from the atoms to the metal surface. With higher temperatures, more atoms acquire the energy needed to overcome the ionization potential barrier, improving ionization efficiency. To optimize surface ionization, ion sources are commonly operated at temperatures around 2000 °C. The voltage drop across the ion source generates a small electric field for multiple purposes. The current is used to heat the material, and the resulting voltage drop generates power. Additionally, the current facilitates the movement of ions toward the exit. This field ensures that the ions converge toward the middle of the source and minimizes the recombination of surface ions with electrons. This method enables selective and efficient ionization of alkalis (Rb, Cs) and is also suitable for rare earths, heavy alkaline earths, and heavy boron group elements, although with reduced efficiency.

When dealing with volatile elements with a high ionization potential (IP), electron impact ionization (plasma) is a suitable approach. Plasma ion sources use electron impact and atom-ion collisions for ionization, a non-selective process capable of ionizing almost any atom that enters the plasma volume, irrespective of its chemical properties. Therefore, plasma ion sources are often used when other ionization methods fail to produce the desired elements, particularly high-IP elements such as noble gases. In this technique, the plasma source confines fast-moving electrons with a magnetic field through which they effuse. However, this source type has a larger emittance than the surface source due to collisions on the extraction region. Therefore, it is best suited for gaseous elements, usually on the right-hand side of the periodic table of elements, such as noble gases, halogens, and oxygen.

Roughly speaking, surface ion sources are effective for ionizing elements in the first group of the periodic table, while the plasma source is used for the last groups and transitional metals. However, plasma sources have the disadvantage of being indiscriminate, compromising the ion beam's purity. The resonance ionization laser ion source (RILIS) can be used to overcome this limitation. The next chapter will provide a detailed explanation of this laser ionization technique.

2.2 ALTO

ALTO (Accélérateur Linéaire et Tandem d'Orsay) at IJCLab is a set of two accelerators located on the University of Paris-Saclay, campus Orsay, France. This ensemble includes a Van de Graff accelerator that delivers stable beams with a voltage of 15 MV to the ALTO-HEB (ALTO High Energy Beam) branch and an electron linear accelerator (LINAC) used to produce neutron-rich radioactive ion beams using the ISOL technique in the ALTO-LEB (ALTO Low Energy Beam) area (Figure 2.3).

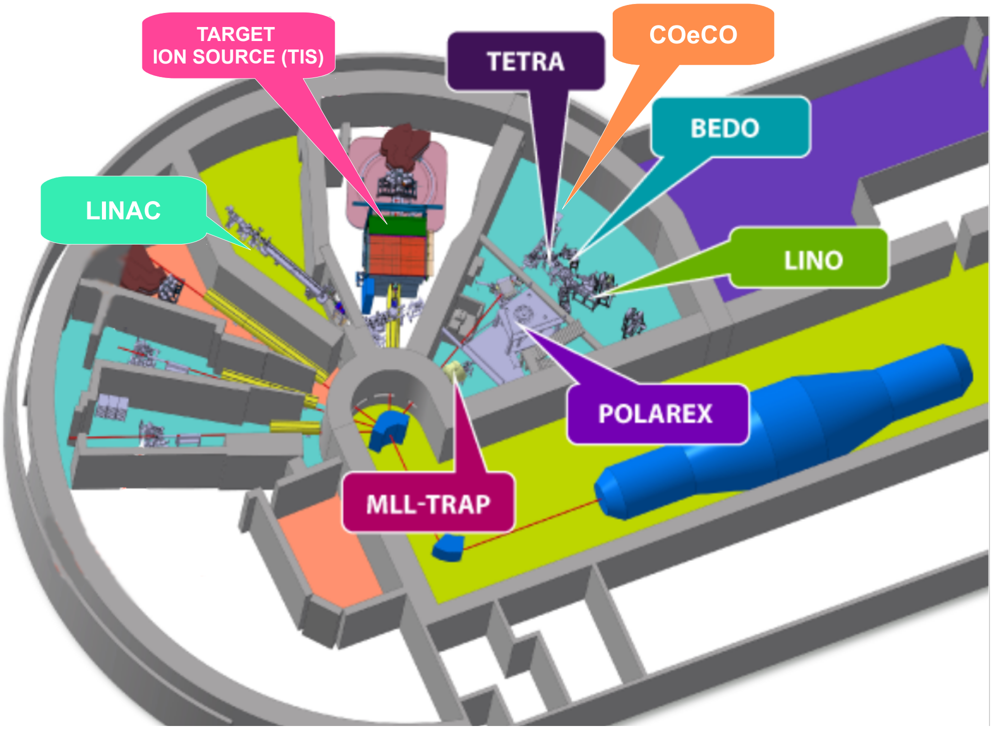

Figure 2.3: Layout of the ALTO Platform. The top right area is the LEB experimental hall.

At ALTO, in order to produce the radioactive atoms, photo-fission is used [21]. It starts by accelerating an electron beam to 50 MeV with an intensity of 10 µA using the linear accelerator (the first section of the old LEP injector) [32]. This beam bombards a 70g target of UCx, corresponding to a density of 3.36 g/cm^3 to induce photo-fission by Bremsstrahlung radiation [33]. The target is a series of UCx pellets in a graphite tube placed in an oven and heated to enhance the diffusion of fission products [34] (Fig.2.4). The intensities of the beams extracted from the UCx target are in the order of 10^2 to 10^8 pps (particles per second), depending on the isotope [35].

The atoms are then ionized by different techniques according to the needs (surface ionization, laser, plasma, see Fig. 2.2). At the exit of the ion source, a potential difference of 30 kV extracts the ionized species to send them to the magnetic spectrometer PARRNe (Production d'Atoms Radioactifs Riches en Neutron) with a resolution of R=$\frac{A}{\Delta A}$=1500. Once selected, the ions are guided by an assembly of electrostatic deflectors and lenses to the experimental platforms (Figure 2.5).

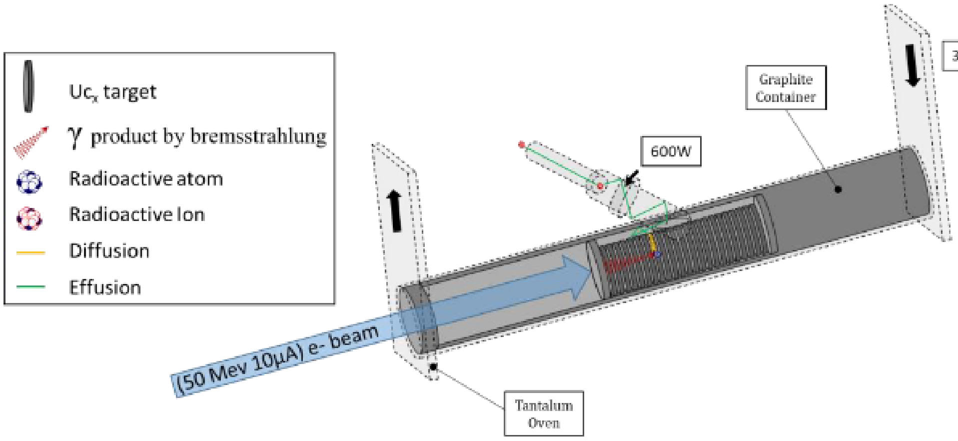

Figure 2.4: UCx Target ion source (TIS) ensemble diagram.

One of the installation's unique features is optimizing the radioactive beam, particularly in the development of uranium targets (Fig. 2.4). Recent studies at ALTO have shown drastic differences in the production rates of certain nuclei depending on the type of target used, whether it is the target's internal microstructure [36] or the radioactive material's density [37]. These studies provide beneficial information when designing an experiment as these new targets result in up to twice the production rate of some nuclei compared to targets typically used at ALTO.

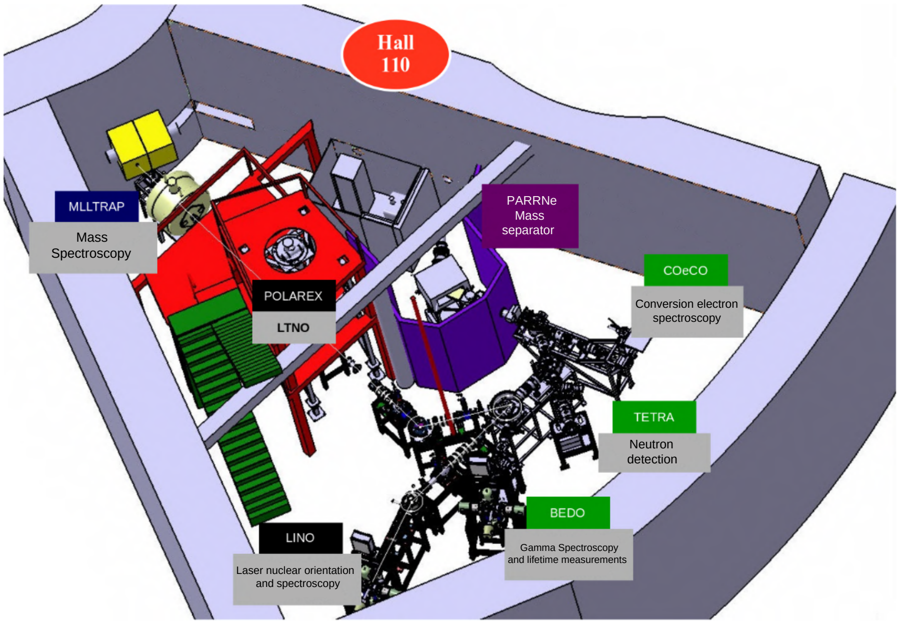

Figure 2.5: Experimental hall of the ISOL facility at ALTO.

The great interest of facilities based on the ISOL technique is to provide beams with low emittance at low energy. This optical quality allows using certain experimental methods which give access to a set of observables to study the nuclear structure. ALTO regroups several instruments needed to explore such observables:

- MLLTRAP [38]: is a double Penning trap mass spectrometer consisting of two identical cylindrical Penning traps inserted in a 7 T superconducting magnet. This trap is used for high-precision mass measurements and trap-assisted decay studies of ground state or long-lived isomers, particularly beta-decaying isomers. The first part is a cylindrical double Penning trap, where the ions are cooled and manipulated before being injected into the second trap. In the second module, the actual mass measurement takes place by determining the cyclotron frequency of the ions. This module is primarily designed to measure masses.

- PolarEx [39]: (Polarization of Exotic nuclei) uses the Low-temperature nuclear orientation technique (LTNO) combined with On-Line implantation of the radioactive beam and nuclear magnetic resonance to study spin and nuclear magnetic properties. It uses a ^{3}He-^{4}He dilution cryostat that permits the measurement of the nuclear orientation obtained by cooling nuclei to ~10 mK in a strong (10-100 T) magnetic field. A radioactive beam is directly implanted into a ferromagnetic foil in contact with the cryostat's cold finger to study short-lived nuclei. However, the LTNO technique cannot achieve instantaneous thermal equilibrium between the nuclei and the medium, which takes up to a few seconds to establish. To magnetize the foil, a superconducting magnet with a maximum field of 1.5T provides a constant field. Due to the host material, the implanted nuclei are oriented through the internal hyperfine field.

- LINO [40]: (Laser-induced nuclear orientation) is a setup for laser spectroscopy and has been successfully commissioned with a stable ^{23}Na beam in November 2019.

- BEDO [41]: (BEta Decay studies at Orsay) is a set of detectors dedicated to post-beta decay gamma spectroscopy and fast timing measurements. The detectors are designed for optimal γ selectivity, detecting weak channels and reducing background. The radioactive source is formed on an aluminized mylar tape that is periodically moved to prevent background from accumulated long-lived decay products. A cylindrical plastic detector covers about 70% of the solid angle and detects the electron signature of the β-decay. To detect γ-radiation, the plastic detector is surrounded by 4 HPGe detectors cooled with liquid nitrogen (77K).

- TETRA [42]: Tetra is a set of 90 neutron detectors arranged in 5 layers of a hexagonal shape designed to study beta-delayed gamma-neutron coincidences. Each detector comprises a ^{3}He-filled proportional counter, a moderator, a high-voltage input, and a preamplifier. The neutron detection principle relies on the $^3\mathrm{He}+\mathrm{n}\rightarrow{}^3\mathrm{H}+\mathrm{p}+780$ keV reactions. Neutrons are moderated to become thermalized and diffuse within the detector, where the counters can detect them. This technique excludes the cross-talk effect and is sensitive to thermal neutrons, with an energy threshold close to zero. The detectors measure the multiplicities and angular characteristics of neutrons originating in the decay of light neutron-rich nuclei.

- COeCO [43] : (COnversion electron Chasing at Orsay) an identification station for β-delayed conversion electron spectroscopy and production measurements. This new system enables the collection and study of a radioactive source produced by the ISOL technique and is optimized to reach very short-lived nuclei. The device uses a magnetic transporter to guide electrons far from the radioactive source and greatly improve its selectivity.

The POLAREX setup requires the beams to be extracted at 60 kV, as implantation is needed. For this reason, a major front-end upgrade was necessary. This entailed completely redesigning the target ion source ensemble within the FRISAL project (Front-end Robotisé pour ISOL ALTO) [44].

To conduct experiments in these setups, pure isotopic beams must be used. However, electron-induced fission fragments at ALTO can still result in significant isobaric contamination even with a selective ion source, as unwanted thermal ionization of atoms may occur on a hot surface, particularly if the ionization potential of the atom is low. The presence of surface-ionized isobars is the principal reason for the reduction of selectivity in hot cavity ion sources. A resonance ionization laser ion source (RILIS) is available at ALTO to address this issue and maximize the selection in Z. In chapter 3, we will discuss a detailed explanation of the RILIS technique.

Chapter 3

Resonant Ionization Laser Ion Source

3.1 Resonance ionization process

The resonant ionization laser ion sources (RILIS) are based on the photoionization (ionization by absorption of one or more photons) of atoms by laser beams. Optical atomic excitation occurs when the laser radiation frequency matches the specific frequency of an atomic transition [45], as shown in Figure 3.1. Since the atoms of each element have a specific level sequence (unique electron shell structure), the ionization process offers excellent element selectivity with high ionization efficiency compared to other non-specific ion source techniques.

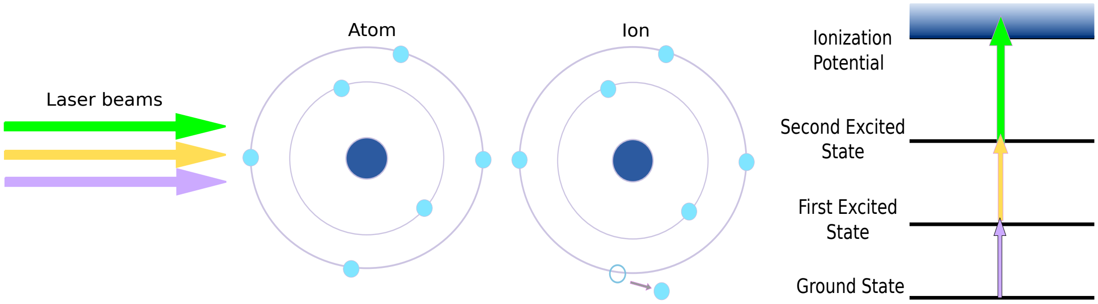

Figure 3.1: Principle of Laser Resonance Ionization. The resonance occurs when the laser frequency matches the atomic transition frequency, with the consequent excitation of the valence electron and ionization.

The resonant ionization process begins with the atom in its ground or low-lying thermally populated state. Valence electrons are stepwise excited by the resonant absorption of laser light. They are driven to a first excited state using a strong atomic transition. For most elements, transitions suitable for this excitation phase lie in the blue or ultraviolet wavelength regions.

Following the first excitation step, the atom is driven to a higher excited state by another strong atomic transition connected to the first excited state. In some cases, this second excited state can already allow ionization when it is near or above the ionization potential. Otherwise, a third excitation step will then ionize the atom.

The classification of ionization schemes depends on factors such as the number of radiation frequencies, resonant excitation steps, and ionization type. The final atomic transition is crucial for the efficiency of the method and can be achieved through several mechanisms. Figure 3.2 shows a diagram of the possible resonant step-wise excitation and ionization processes.

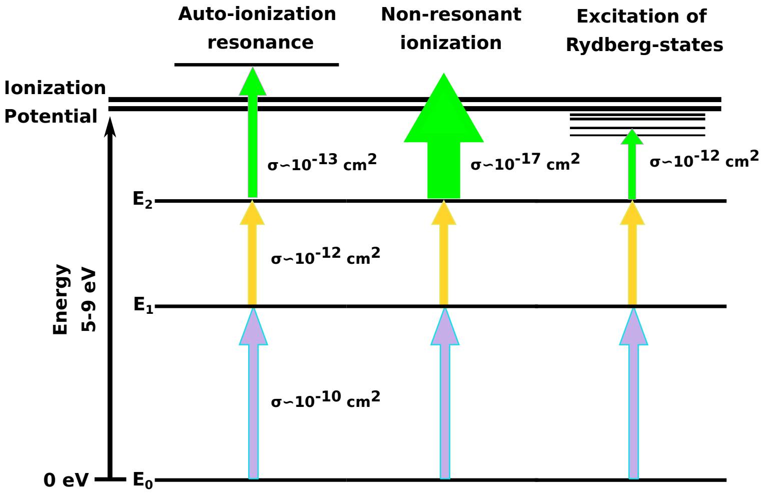

Figure 3.2: Schematic representation of Resonance Ionization. The arrows illustrate the stepwise optical excitation of an atom from its ground state to ionization. The last excitation step determines the ionization efficiency and can be reached by different mechanisms: non-resonant ionization to the continuum, Rydberg-states, or autoionizing states.

The probability of a single-step excitation process can be described as

$$P = \sigma \phi_{\gamma} \tag{3.1}$$

where σ is the atom cross-section and ϕ_{γ} is the photon flux density.

3.1.1 Autoionization states.

Autoionizing (AI) states are unbound atomic states that exist in multi-electron atoms above the ionization threshold, resulting from the excitation of two or more electrons. In the autoionization process, each electron undergoes a transition between discrete quantum states, contributing to the total excitation energy that exceeds the ionization limit. As a result, this excess energy is rapidly redistributed between the excited electrons in a non-radiative process, emitting a free electron and leaving the atom in an ionic state. The theoretical description of autoionizing resonances is further given in [46].

The cross-section for a transition to an auto-ionizing state is several orders of magnitude larger than for non-resonant transitions. The significance of these states is highly dependent on the laser system or application.

3.1.2 Rydberg states.

Rydberg levels are atomic levels that are energetically close to the ionization potential and have a high principal quantum number which is successively increasing [47]. Due to their long lifetimes and energy proximity to the ionization potential, Rydberg atoms are sensitive to external effects. Several mechanisms can be used to strip the electron from the Rydberg state, such as black body radiation, infrared lasers, collision with other atoms, or an electrical field. The high number of possible ionization mechanisms results in a high probability of ionizing the atom from the Rydberg states. The effectiveness of this mechanism is constrained by its strong dependence on ionization volume conditions, which can vary substantially across different experimental configurations, including factors such as the temperature of the ion source, the strength of the electric field, and the collision rate.

Information on the AI or Rydberg transitions can be obtained directly from the atomic databases [48, 49, 50].

3.1.3 Non-resonant ionization.

Some transitions are not accessible within the wavelength tuning range of the laser system. For other cases, there are no known transitions to connect the efficient excitation steps to autoionizing or Rydberg states. For this reason, high-power lasers are often applied in the last step for a non-resonant transition to the continuum [51].

This process is less sensitive to the laser frequency; the only condition for this ionization mechanism is that the photon energy must be higher than the energy difference between the excited state and the ionization potential.

The non-resonant process is the least efficient ionization mechanism. It has a relatively low cross-section (~ 10^{-17} cm^2), which is a disadvantage compared to the cross-section of the resonant transitions for auto-ionizing or Rydberg states (~ 10^{-12} – 10^{-13} cm^2). The transition's small σ makes it challenging to reach saturation, leading to a linear dependence of the ionization probability on the number of atoms interacting with the photons.

3.1.4 RILIS requirements

A resonant ionization laser ion source comprises two main components: the ion source and the laser system (Fig. 3.3). The ion source is located at the isotope production front end of the on-line mass separator and is connected to the hot furnace target area. It is based on a conventional surface ionization source and provides confinement of the radioactive atomic vapor until it is ionized. The laser system enables the resonant ionization of radioactive atoms and is installed in a temperature-controlled room separated from the target ion source area. The laser system consists of two or three tunable pulsed lasers that allow the selection of the proper wavelength for resonant photo-excitation with a high energy per pulse. The laser beams are transported from the laser room to the ion source through the mass separator and the extraction system. They overlap in space and time to enable ionization inside the ionization tube. Finally, the generated radioactive ion beams are extracted and mass selected.

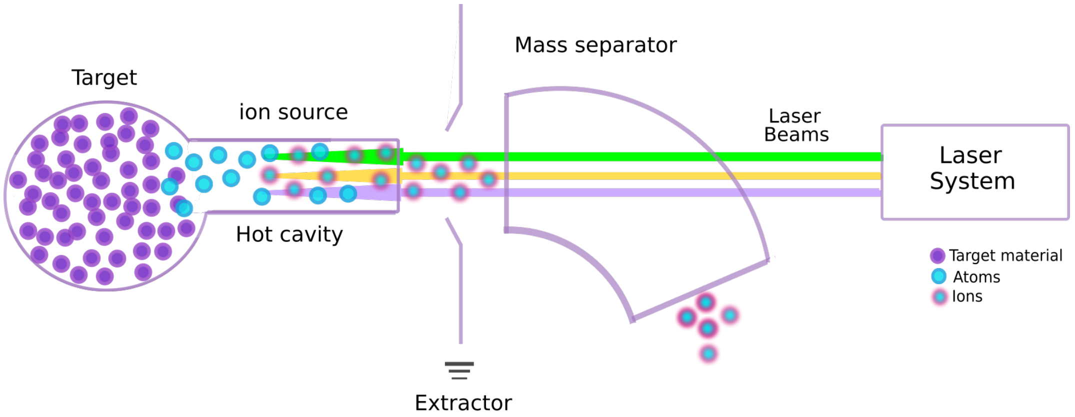

Figure 3.3: Resonant Ionization Laser Ion Source diagram. Radioactive atoms from the target enter the ion source, where laser beams resonantly photo-excite them to produce a radioactive ion beam. The laser beams are transported through the mass separator and extraction system to the ion source, where they overlap to ionize the atoms inside the ionization tube. The resulting radioactive ion beams are then extracted and mass-selected.

As mentioned in the introduction, an ion source for on-line applications must meet several requirements: universality, selectivity, efficiency, reliability, and rapidity [14]. The RILIS technique has a high universality, being able to ionize 80% of the periodic table's chemical elements. Its selectivity allows the ionization of one element at a time, which is its primary advantage over other ion-generation techniques [52]. The efficiency of RILIS depends on the chosen ionization schemes and atomic species, with ionization efficiencies ranging between 5% and 30% for most elements [53]. The long-term stability of the laser system is crucial for the technique's reliability, and its versatility allows for adaptation to various settings. The process's rapid nature reduces decay losses in the ion source, as the ionization time is negligible compared to the release and effusion time in the system.

RILIS is an efficient, selective, and powerful tool to increase absolute yields and reduce isobaric contamination. Almost universal since 80% of the chemical elements have an ionization potential between 5 and 9 eV (Fig. 3.4). The approximately 2 eV required for each atomic transition falls into the visible spectrum [54], making them accessible through this method if the excitation schemes are known. However, some elements are not accessible due to their high ionization potential (noble gases or some halogens). For some others, the first accessible excitation step requires a wavelength below 200 nm (this radiation will not transmit in the air due to UV absorption) or lays outside the tuning range of lasers.

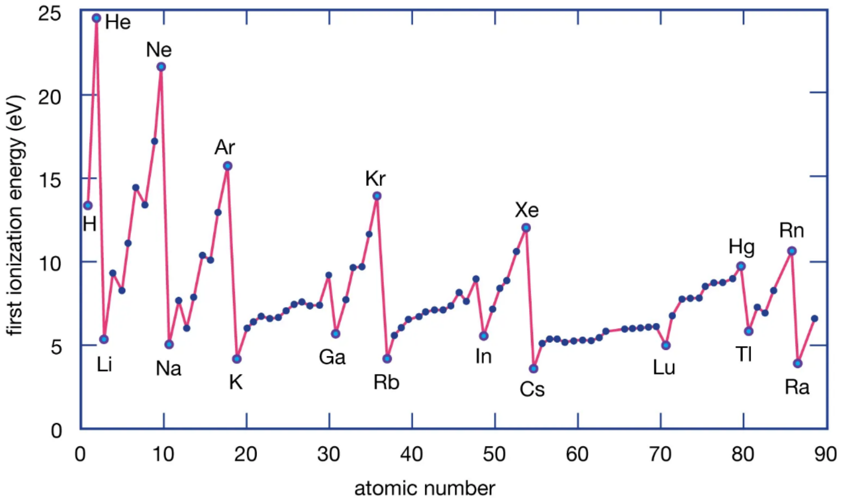

Figure 3.4: The evolution of the first ionization energy as a function of atomic number. For numerous elements, the ionization potential does not exceed 9 eV, thus accessible with laser ionization.

Given the advantages of RILIS, the ALTO facility created and implemented one several years ago. The specifications and operation of the main elements of this source are described in detail in the following sections.

3.2 RIALTO laser system

The laser ion source of ALTO (RIALTO) [55], located above the PARRNe mass separator, aims to produce pure ion beams using the resonance ionization technique.

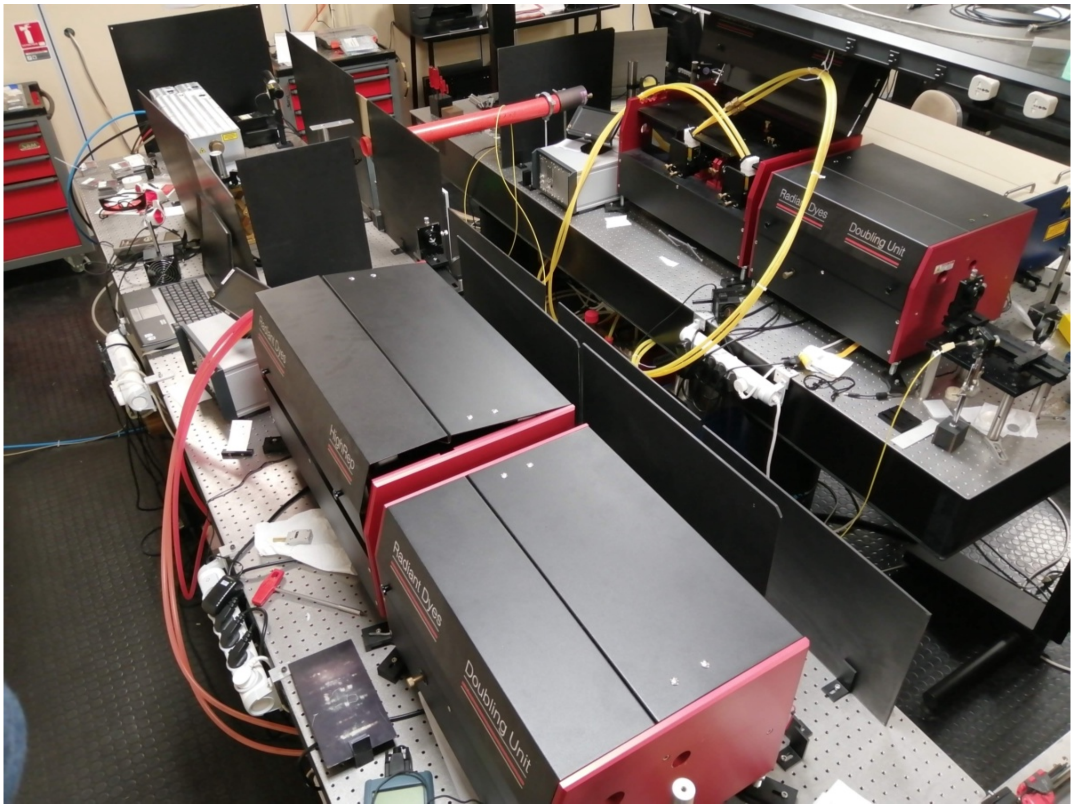

Figure 3.5: RIALTO laser system layout. Three tunable dye lasers pumped by a frequency double Nd:YAG laser.

The laser room is equipped with a frequency-doubled high-power neodymium-doped yttrium aluminum garnet (Nd:YAG) (532 nm, 100W), operating at 10 kHz repetition rate and pulse-width (FWHM) of ~ 10 ns, which pumps three grating tuned high repetition dye lasers (540–850 nm), two from Radiant Dyes [56] and one from Lioptec [57], with their BBO (Barium Borate BaB_2O_4) doubling units (270–425 nm) to achieve two and three-step ionization schemes (Fig. 3.5).

3.2.1 Nd:YAG pump laser

An Edgewave Q-switched diode-pumped solid-state Nd:YAG laser (Model INNOSLAB IS2011-ET [58]) in its second harmonic is used as a pump source for the dye lasers and as non-resonant ionization. The intracavity of the Nd:YAG produces light at a wavelength of 1064 nm. The frequency of this beam is doubled inside the laser with a nonlinear crystal to obtain an output green laser beam of 532 nm with up to 100 W average laser power [59].

For efficient resonant photo-excitation, the output power of the laser must be sufficiently high to transfer energy to the atomic transition. To satisfy the flux condition, the depopulation rate from the excited state through ionization into the continuum should be significantly greater than the rate towards other states, such as a metastable state [60]. Considering that the cross-section for non-resonant transitions is generally less than ~ 10^{-17} cm^2, a laser beam with a diameter of approximately 3 mm, derived from a frequency-doubled Nd:YAG laser, would necessitate several kilowatts of power to saturate a non-resonant transition. A pulsed laser can reach a peak power superior to this value (> 0.5 kW). The Q-switch technique can quickly generate pulsed laser beams that emit a large amount of light radiation, where the peak power depends on the pulse length. This technique is based on the accumulation of energy that the pump laser provides and its subsequent sudden release [61].

The pulsed operation of the system provides high peak powers, which are needed to excite weaker atomic transitions, and allows efficient higher harmonic generation in nonlinear optical crystals (section 3.2.2). Therefore, the Nd:YAG laser operates at a repetition rate of 10 kHz

[62], which is approximately the frequency required to ensure that atoms inside the ion source interact with at least one set of laser pulses before leaving this region.

Due to its top-hat beam profile, the IS2011-ET Nd:YAG laser is used to pump the dye lasers, providing a uniform intensity distribution over a large area. This uniformity helps to excite the laser medium evenly, leading to improved performance and stability.

Pulsed laser light allows sufficient peak intensities for single-pass frequency conversion, which, combined with the ability to pump dye lasers, allows uninterrupted spectral coverage between 350 and 900 nm.

The pump laser has a maximum average output power of P=100 W and is divided into three secondary beams. First, with a fixed Reflection/Transmission (50R/50T) ratio beam-splitter, the beam is divided into the beam used for the final ionization step (non-resonant step), and the rest of the power is equally distributed into two beams for pumping the dye lasers (Fig. 3.6).

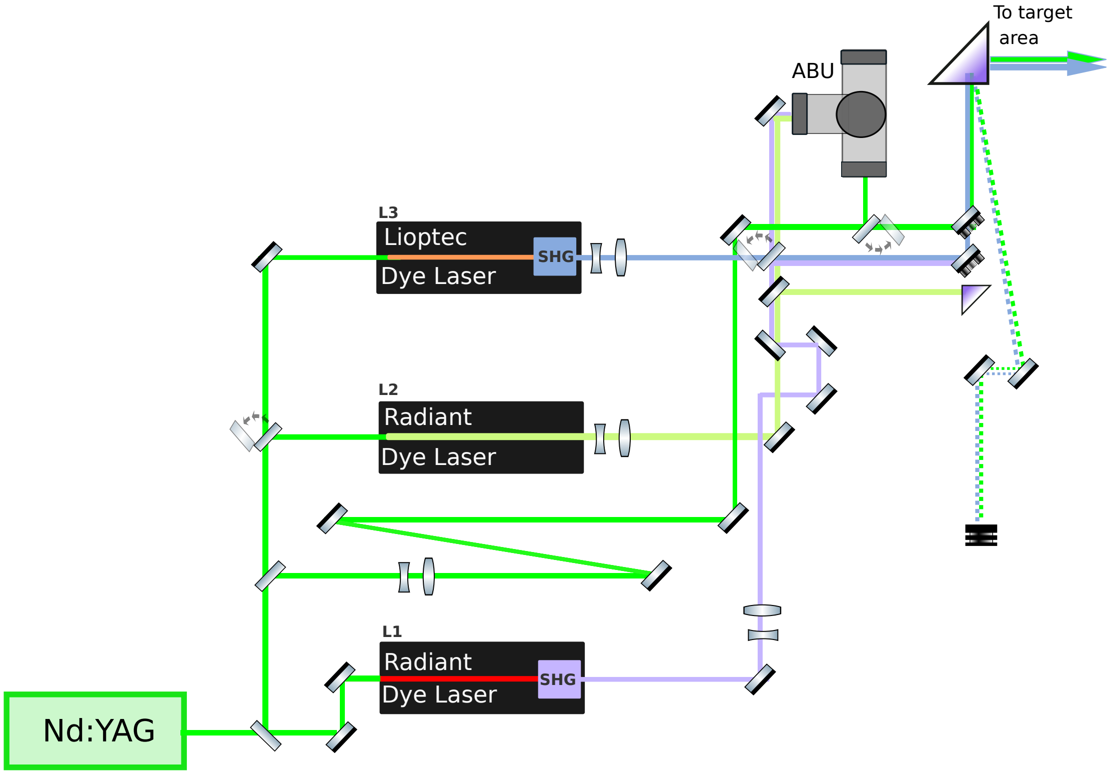

Figure 3.6: Schematic representation of old RIALTO laser system layout and beam distribution (not to scale). Three tunable dye lasers (L1, L2, L3) are pumped by a frequency-doubled Nd:YAG laser, also used for non-resonance ionization.

3.2.2 Dye lasers

As mentioned before, RIALTO is equipped with three grating-tuned high-repetition dye lasers. Each dye laser consists of a laser resonator, a power amplifier, and a single-pass doubling unit. An 1800 lines/mm grating works as a wavelength tuning element inside each laser resonator in a Littman configuration [63], which allows a tuning range of 350-900nm and a linewidth of the laser of about 3GHz (Fig. 3.7).

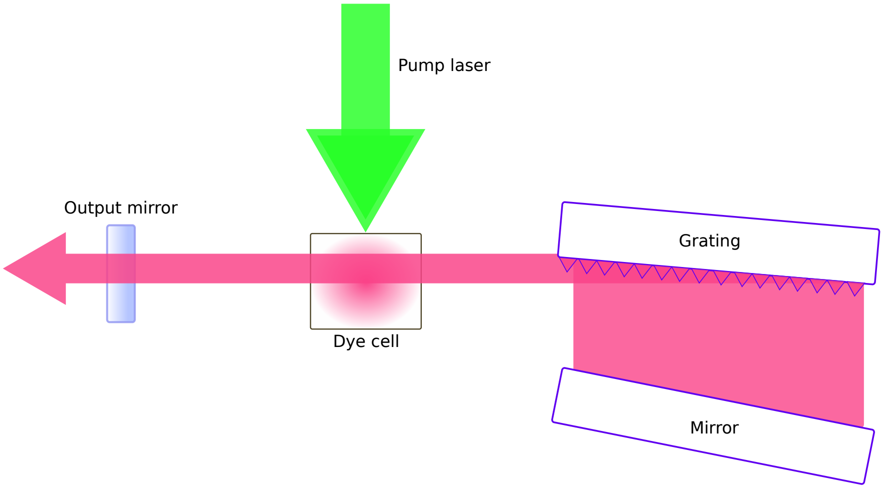

Figure 3.7: Dye laser cavity Littman configuration.

A dye laser uses an organic dye as a gain medium, a soluble, fluorescent carbon-based molecule dissolved in a compatible solvent to ensure even diffusion. This solution is circulated through a dye cell or cuvette, and a high-energy light source is used to "pump" the liquid beyond the lasing threshold. Due to the dye's high absorption, the pumping energy can be concentrated in a small volume of liquid. The laser's reflector cavity is water-cooled to prevent thermal shock in the dye caused by the high amount of near-infrared radiation. One limitation of dye laser systems is the decay of the gain medium's performance over time, which requires frequent maintenance. However, this issue can be overcome using pulsed laser systems. Pulsed lasers efficiently replenish the energy of the dye laser gain medium to prevent decay and depletion of its energy levels caused by spontaneous emission and relaxation processes. The pulsed laser delivers energy to the gain medium in short, intense bursts, enabling rapid absorption and elevation to a higher excited state. This minimizes the time available for energy decay, maintaining a sustained population inversion and preventing loss of gain. As a result, the dye laser system achieves enhanced performance with improved output powers and consistent coverage of the UV-NIR spectrum.

Dye lasers have a wide emission spectrum that ranges from 400 nm and can be extended to the blue and UV ranges through nonlinear crystals, allowing for second harmonic generation (SHG) or triple harmonic generation (THG) from the fundamental laser output light. Figure 3.8 shows the approximate working ranges of various laser dyes.

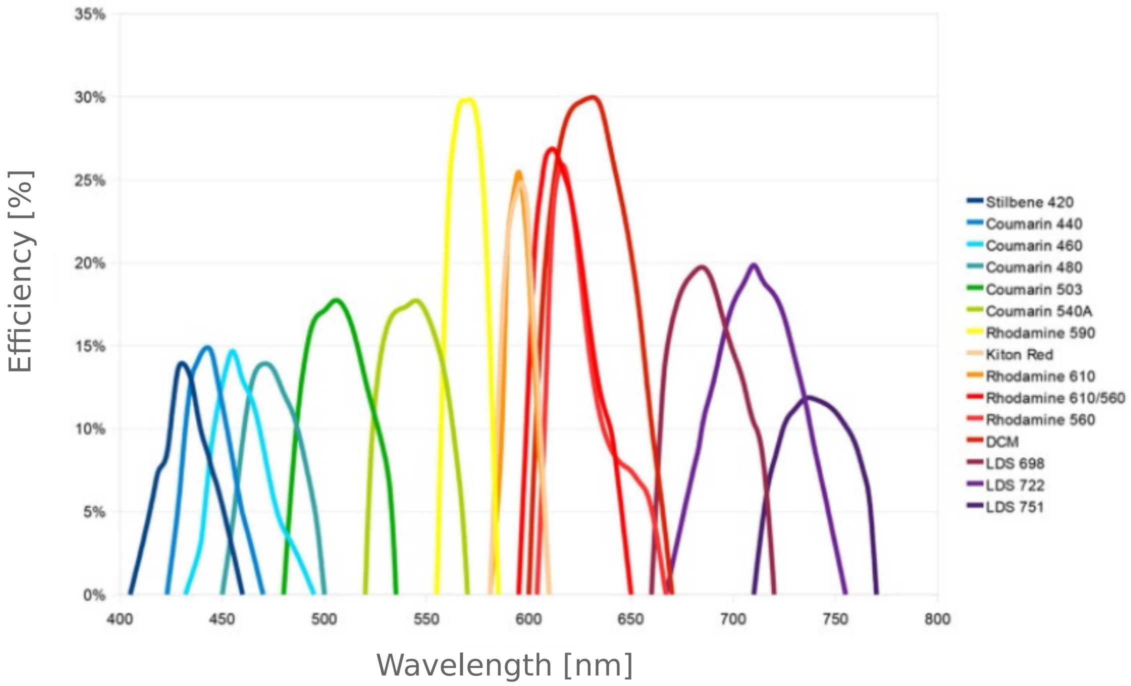

Figure 3.8: Dye tuning and dye efficiency curve of the Radiant laser pumped by Nd:YAG laser at 355 nm and 532 nm [56].

The RIALTO dye laser system consists of an oscillator and an amplifier, which use a dye cell containing a flowing dye solution. The oscillator generates a laser beam with a specific wavelength, followed by the amplifier, which amplifies the beam power. The dye solution is held in a cuvette, with mirrors on either side to create a cavity (Figure 3.9). The oscillator includes a dye cell close to a laser cavity and is pumped by a pulsed Nd:YAG laser. The oscillator dye cell generates a laser beam with a predetermined wavelength propagated through the cavity. It also includes a grating (G1) and an output coupling mirror (G2/M) to reflect and couple the beam out from the cavity. The output beam is spatially processed externally to the cavity to improve its coherence. The amplifier (K2/B) is pumped by a second pulsed Nd:YAG beam and is designed to couple optimally with the oscillator after an optical delay. A cylindrical lens (L5) focuses the oscillator beam into the active volume of the amplifier. The oscillator-amplifier distance is adjusted to match the oscillator beam's height to the amplifier's active dye volume, and the pump and input beams are synchronized by adjusting the optical path length of the pump. If the two pulsed YAG lasers are synchronized, the amplifier will amplify the laser pulse from the oscillator dye cell, both in frequency and transverse phase, resulting in an output that is spatially and spectrally coherent with increased power.

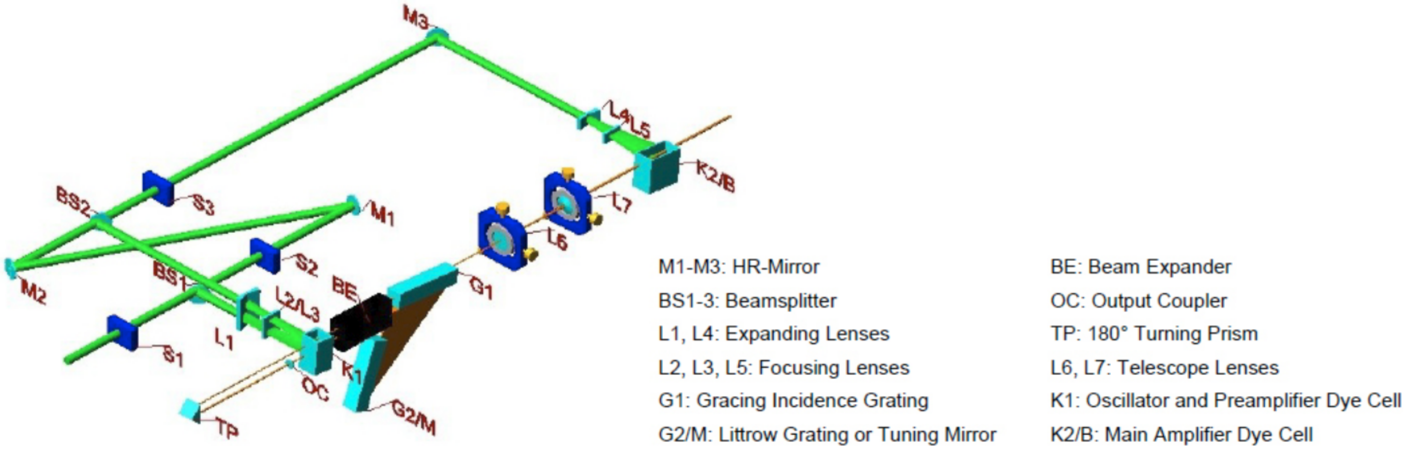

Figure 3.9: Optical layout of the Radiant Dyes Laser [56].

High harmonic frequency generation

One limitation of resonant photo-excitation using dye frequency radiation is the inability to access high-energy transitions. Since almost all elements' first excitation steps are typically in the blue to UV spectrum, a frequency conversion of the wavelength emitted from the dyes is necessary. This conversion is achieved through nonlinear polarization effects in nonlinear optical (NLO) crystals. To further extend the accessible wavelength range of the laser system, higher harmonic generation (HHG) and frequency mixing with NLO are employed. This technique is thoroughly understood and extensively documented in various literature sources [51, 47]; a brief summary of the basic principles of HHG is presented below.

The basic principle involves a nonlinear polarization response to a laser beam's oscillating electromagnetic field $E(t, \mathbf{z})$ in a nonlinear optical medium. The resulting polarization density can be described using a Taylor series,

$$P(t, \mathbf{z}) = \epsilon_0(\chi^{(1)}E(t, \mathbf{z}) + \chi^{(2)}E^2(t, \mathbf{z}) + ...), \tag{3.2}$$

where $\chi^{(n)}$ is the susceptibility of the order n. For two interacting photons, the electromagnetic field $E(t, \mathbf{z})$ can be expressed as

$$E(t, \mathbf{z}) = E_1 \sin(\omega_1 t + \mathbf{k_1 z}) + E_2 \sin(\omega_2 t + \mathbf{k_2 z}). \tag{3.3}$$

As the medium's nonlinearity implies $\chi^{(2)} > 0$, the quadratic term $E^2(t, \mathbf{z})$ gives rise to polarization density modulations, including sum and difference frequencies, $\omega_1 + \omega_2$ and $\omega_1 - \omega_2$. These modulated polarization densities induce oscillating electromagnetic fields that can interfere constructively, resulting in a macroscopic beam of laser radiation. To achieve this constructive interference at the desired frequency, $\omega_3 = \omega_1 \pm \omega_2$, the electromagnetic fields must have the correct phase relationship, known as the phase-matching condition, where the wavevectors satisfy $\mathbf{k_3} = \mathbf{k_1} \pm \mathbf{k_2}$.

However, chromatic dispersion can lead to a mismatch. To overcome this problem, the birefringence of the NLO crystal can be utilized to achieve correct phase matching. Two common approaches are 1) noncritical phase matching, where the crystal's temperature is adjusted to match the refractive indices for different polarizations, and 2) critical phase matching, where the crystal's angular orientation is used to adjust the extraordinary refractive index. The phase matching is denoted as type-I if both initial photons have the same polarization perpendicular to the resulting photon and type-II if the polarizations of the initial photons are perpendicular.

At RIALTO, second harmonic generation (SHG) is achieved using beta barium borate (BBO) crystals as the NLO material. The dye lasers are equipped with a frequency conversion unit (FCU) that utilizes a Barium Borate BaB_2O_4 crystal. The process is optimized through critical phase matching and type-I phase matching techniques.

The crystal is mounted on an automated motor, enabling a computer-controllable angle variation between the incident laser's polarization and the crystal's optical axis to achieve the critical phase matching in frequency doubling. A correlated automatic control of the grating and the BBO crystal allows continuous scanning of the second harmonic wavelength. An arrangement of 4 Pellin-Broca prisms separates the UV from the fundamental beam (Fig. 3.10).

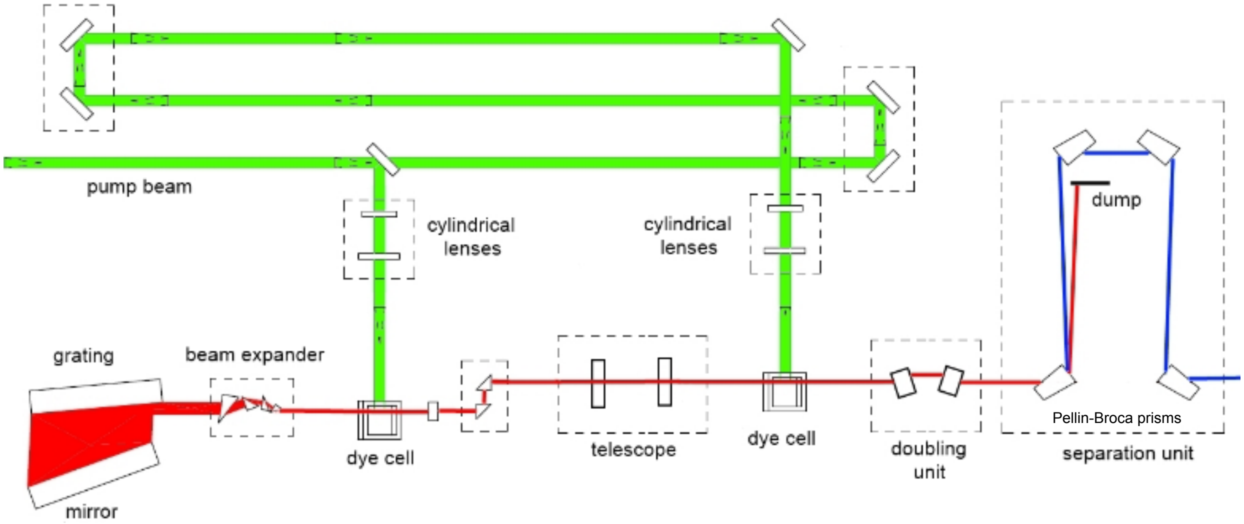

Figure 3.10: Optical layout Lioptec dye laser with frequency conversion unit [57].

3.2.3 Beam transport and monitoring

The laser laboratory is located in an unrestricted zone, in a temperature-controlled room requiring an optical path of about 20 m to transport the laser beam from the laser room to the target ion source area. We reduced the number of optical elements used to transport the laser beam to avoid power loss due to imperfect mirror reflections and to make tuning the system easier (Fig.3.6).

Each laser follows an independent optical path from the laser output to the ionizing tube, but they all merge in a dichroic plate at the outing of the laser room to be transported to the TIS area. The laser beam path and optics are arranged as shown in Fig. 3.6.

The laser beams are expanded using a Galileo telescope with divergent lenses to achieve an appropriate focus on the entire ionizing tube and achieve a small diffraction-limited spot size of 3mm after the long flight path. Specifically, L2 uses an f-25 lens (25 mm focal length), L3 an f-50 lens (50 mm focal length), and L1 and the Nd:YAG use an f-75 lens (75 mm focal length). Following the expansion, the laser beams are focused using convergent lenses. L3 is focused with an f+200 lens (200 mm focal length), while the other components utilize an f+250 lens (250 mm focal length). A Schematic of the telescope is shown in figure 3.11.

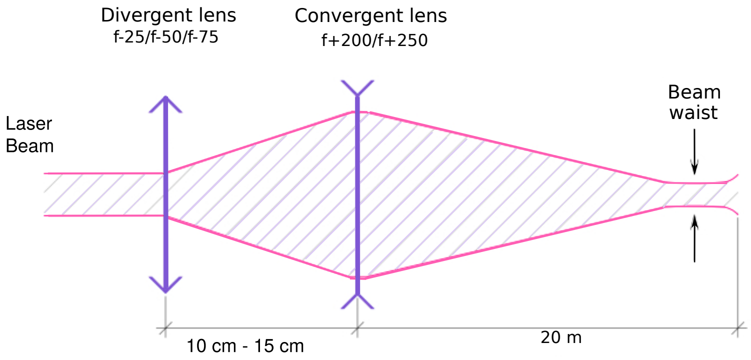

Figure 3.11: Diagram of Galileo telescope (not to scale). A divergent lens expanded the laser beams and then focused by a convergent lens to control the laser spot size at the ion source located at a distance of 20 m.

Two motorized mirrors are installed to fine-tune the laser beams. They use an actuator with a high-performance compact stepping motor to adjust the horizontal and vertical axes (Fig.3.12a). They are remotely controlled by PC using a program written in LabVIEW. They are installed on a wall-mounted laser table above a 90-degree bending prism positioned in the line of sight of the mass separator laser viewport and the laser ionization region.

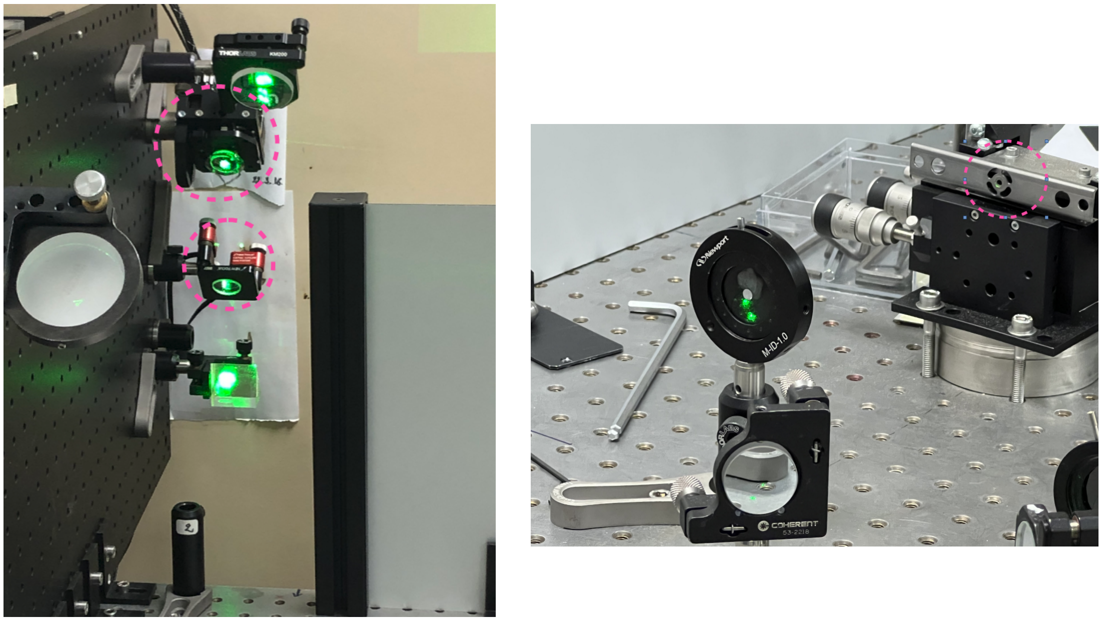

(a)

(b)

Figure 3.12: Beam transport and monitoring. a) shows the motorized mirrors(inside the pink circle) above the prism before the mass separator (last accessible point in the laser room). b) shows the reference tube (inside pink circle), set up at the same distance as the ion source from the prism and has identical dimensions and an iris that allow us to fix the beam position to ensure reproducibility.

By matching the total path lengths of the reference beams with those of the main beams at the ion source position, these reference beams are a reliable tool to estimate and optimize the focus and spatial and temporal overlap of the beams. They are used to establish the optimal conditions for the experiment. To control the position of the laser beams within the ionization tube, a partial reflection of the optical prism in front of the mass separator is directed to a screen located 8m upstream, which simulates the tube (Fig.3.12b).

After the beam transportation is optimized, the beam shape is marked on the beam spot screens, and several irises are set for fixed conditions. These measures ensure that the laser beam path is reproducible. This reflection spot also monitors the laser beam positions during radioactive beam production.

Several steps are taken to align the laser beams for ionization, including initial visual alignment, manual fine-tuning, and beam focusing. The process begins in the laser room and moves to the entrance of the mass separator, where the lasers access the ionization region via a vacuum window. An uncoated, UV-graded, fused silica prism is located before the lasers enter the separator. In the first step, the laser beam is roughly tuned by adjusting the mirrors to hit the central area of each mirror and pass through the laser room's reference tube. In the second step, the two beams are aligned at the entrance of the separator, ensuring they are still mixed up in the laser room. Finally, the beams are aligned in the ionizing tube using a graduated target (Fig. 3.13). The positions are optimized by monitoring the laser power with a power meter placed in the source. Once we are done optimizing the power, we compare it with the power at the lasers's output to calculate the power losses (Table 3.1).

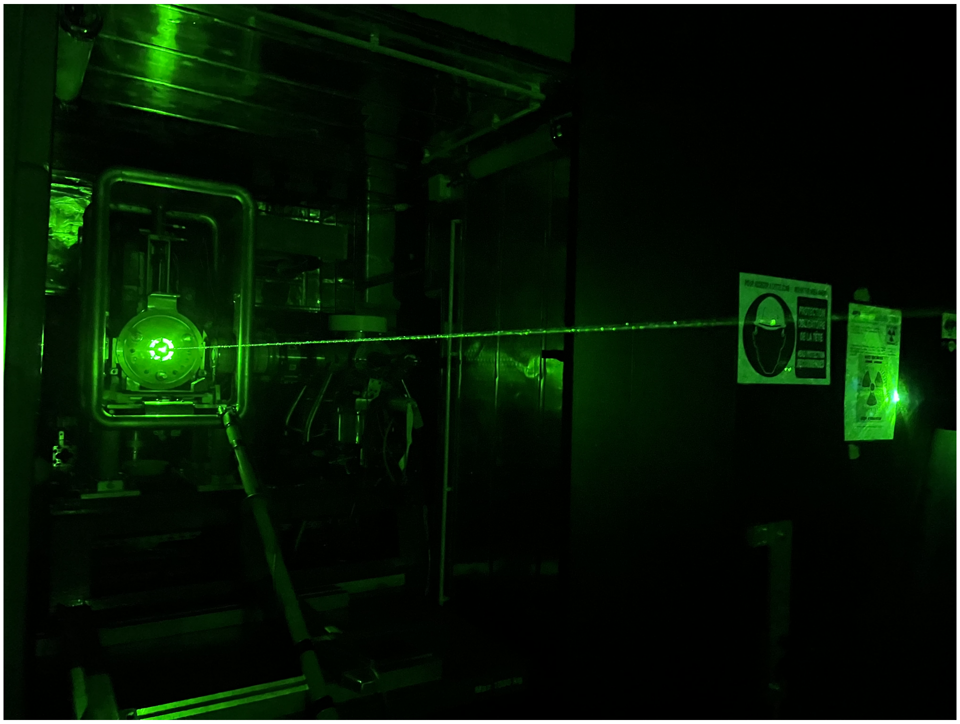

Figure 3.13: Laser beams going through the ionization tube. After passing through the mass-cycling magnet, the laser beams travel in the opposite direction of the beam ions. They are then focused into the hot-cavity ion source, which requires the removal of the target reservoir and opening of the transport tube. This allows the laser beams to pass through the ion source and reach the laser power meter.

	λ [nm]	$P_{\text{Laser room}}$[mW]	P_{source} [mW]	Transmission (%)
First step Ga	287.5	160	125	78
First step Ag	328.162	130	73	56
Second step Ag	546.702	250	100	40
Non-resonant step	532	32000	20000	58

Table 3.1: Power transmission from the laser room to the ion source in the tests presented in this work.

Based on the power values we obtained, we calculated each beam's power transmission coefficient. The overall values are: 78% for $\mathrm{UV_{Ga}}$, 56% for $\mathrm{UV_{Ag}}$, 40% for $\mathrm{Green_{Ag}}$ and 58% for the Nd:YAG. The transmission quality of our reference beam (Nd:YAG) is compromised due to the dichroic plate used to combine it with the UV beams.

To monitor the laser wavelengths for the ionizing scheme, we use a commercial HighFinesse WS6-600 [64] wave-meter that provides information on the spectral bandwidth and a precision of 600MHz at wavelengths between 350-1100nm. The wavemeter is calibrated with a frequency-stabilized He-Ne laser (Melles Griot N-STP-910-230 [65]). For calibration, the light from the laser is sent to the fiber that is connected to the wave-meter.

Besides the intensity of the laser radiation, using pulsed laser light adds another adjustable parameter, the timing of the individual laser pulses. The beams' temporal overlap strongly influences the efficiency of the source. When using multiple lasers, it is crucial to ensure a good temporal overlap between them and that their pulse timing jitter is kept low. It is also essential to consider the pulse lengths of the lasers and ensure that they do not exceed the atomic state lifetime. To achieve low jitter synchronization of solid-state pump lasers, a common master clock can be used to trigger the Q-switch drivers.

We use photo-diodes to monitor the timing signals on an oscilloscope to ensure the temporal overlap of the dye and Nd:YAG laser. Figure 3.14 shows the synchronization of three laser beams for a 3-step 3 color ionization scheme with a temporal overlap better than 5 ns. The jitter of each pulse is ~ 2 ns.

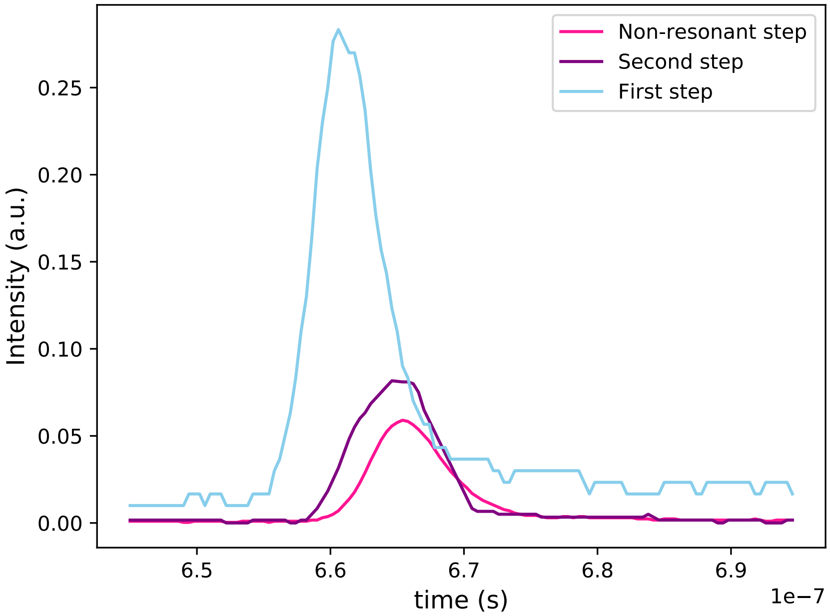

Figure 3.14: Temporal overlap of three laser beams for a 3-step 3 color ionization scheme. The FWHM for the first step is 5.6(6) ns, 7.4(9) ns for the second step and 6.4(1) ns for the non-resonant step.

When a shared laser is used to pump the dye lasers, and used as a non-resonant step, the synchronization can only be achieved through optical delays. This approach makes it almost impossible to re-synchronize the beams, if they drift during the experiment, without stopping the beam. To address this problem, an external frequency generator can be used to synchronize the beam without incurring power losses from additional optical components (see Section 4.2.1).

Long-term pointing and frequency stability is obtained passively by maintaining stable operating conditions for the Dye lasers, such as the Dye cuvette cooling water and the laboratory temperature. However, even with these measures, position drifts can still occur during long-term experiments. To address this issue, an active stabilization system is necessary (section 4.4).

3.2.4 Atomic Beam Unit

To test ionization schemes for different elements, an off-line test bench is available at RI-ALTO, equipped with an Atomic Beam Unit (ABU); its design is based on a prototype from the LARISSA group of Mainz university.

The ABU allows determining optimal operational parameters for on-line use of the radioactive beam by obtaining a qualitative validation of ionization schemes, providing confidence for the direct transfer of development results to on-line operating conditions.

An atomic beam of stable isotopes of the target element is created within the vacuum vessel to facilitate this process. The atomic beam is then probed using lasers to monitor all relevant laser parameters, including power, spectral behavior, and spatial and temporal overlap.

In the ABU, a stable sample of the element of interest is placed in a graphite oven enclosed in a tantalum filament wiring, heated by resistive heating with a current of up to 30 A to a temperature of up to 2000°C. A repeller plate with a positive voltage is installed in front of the oven to suppress surface-ionized ions. In preparation for ionization, the atomic vapor beam undergoes additional collimation using two collimation plates, as depicted in Fig. 3.15. The first plate, referred to as the ”Big plate,” features an opening diameter of 4 mm, while the second plate, known as the ”small plate,” has an opening diameter of 2 mm. These plate configurations aim to minimize the divergence of the atomic vapor beam within the ionization region. By employing the collimation plates, the range of atom directions reaching the ionization region is limited, allowing only a low divergent beam to enter this specific region.

The lasers will interact with the atomic vapor immediately downstream of the repeller plate, where the ion-free atomic vapor is dense. One more electric plate downstream will direct the laser-ionized ions toward an electron multiplier (SEM). A pre-acceleration electrode in the front of the electron multiplier pulls the laser ions upwards and couples them into the SEM (Model: ETP 14120), whose output current is measured by a picoampermeter (Fig. 3.15). The working pressure of the chamber is 10^{-6} mbar. The typical values for the ion-optical components are shown in Table 5.1.

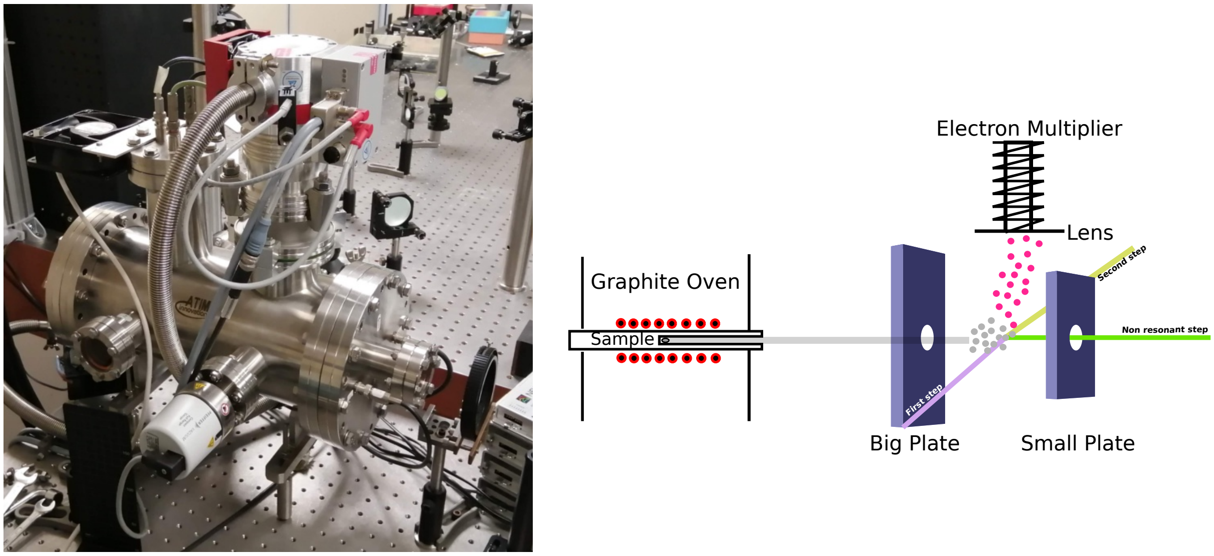

(a) RIALTO's ABU (b) Schematic representation of the ABU

Figure 3.15: Atomic Beam Unit (ABU). A sample of interest is placed in the graphite oven. Then it is heated to produce an atomic flux. The laser beams interact with this flux producing an ion beam. The SEM detects the ion beam.

The atomic beam unit was used to make the offline development of the silver ionization scheme and it will be discussed in chapter 5.

Chapter 4

RIALTO upgrade

4.1 Current layout

To improve the performance of the laser ion source at ALTO, we focused on four aspects:

- Quality of the non-resonant step.
- Beam distribution system.
- Beam stability.
- Ability to study more than one element at the same time

We acquired an Edgewave electro-optical Q-switched diode-pumped Nd:YAG laser (Model INNOSLAB, BX 80-2-G [66]) to use exclusively for non-resonant ionization (section 4.2). For the transport of the Nd:YAG lasers, we changed to a combination of half-wave plates ($\lambda/2$) and polarized beam-splitter cubes (section 4.3). Two beam-pointing stabilization systems are employed in the setup (section 4.4). A schematic representation of the upgraded system is shown in Fig. 4.1. The different elements will be described in the following sections.

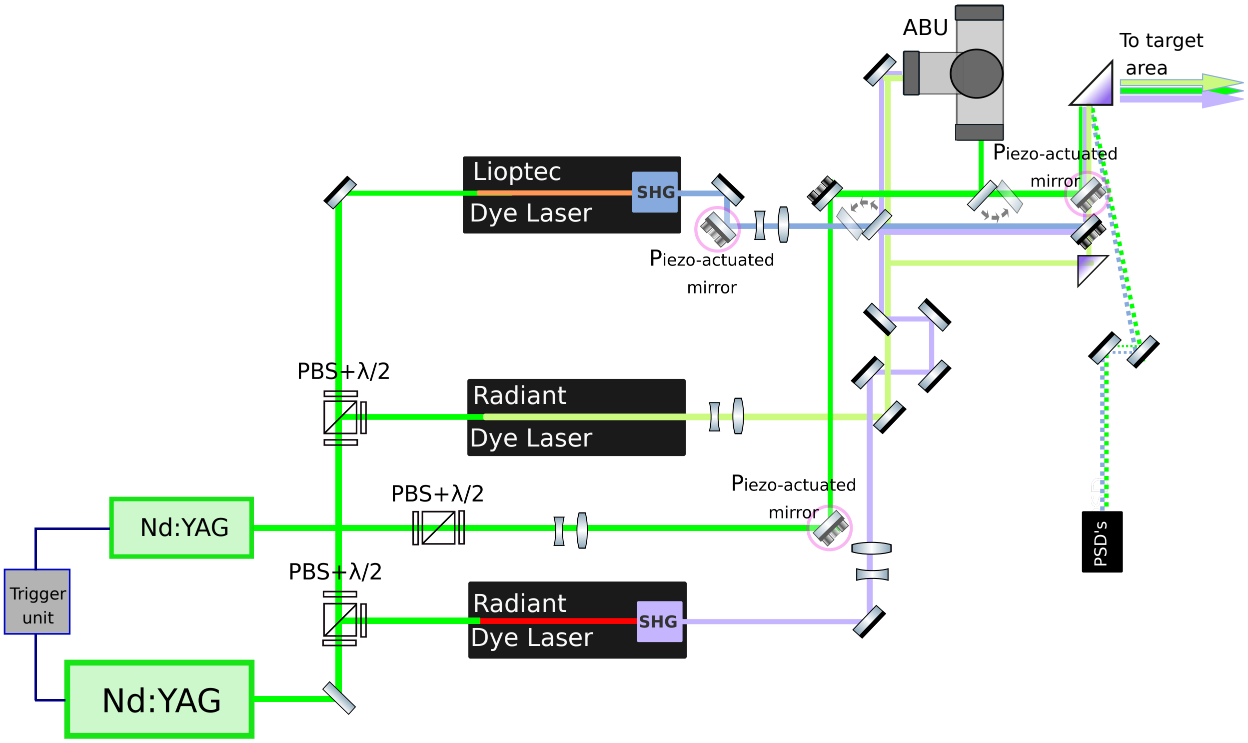

Figure 4.1: Optical layout of RIALTO upgraded system (not to scale).

4.2 New Nd:YAG laser

An Edgewave electro-optical Q-switched diode-pumped Nd:YAG laser (Model INNOSLAB, BX 80-2-G [66]) was recently installed at RIALTO, and it's being used for non-resonant ionization. This laser delivers a 532 nm beam, operating at 10 kHz with up to 32 W power average.

The new laser features a Gaussian profile beam suitable for ionization due to its high power density. This results in an improved ionization performance and a reliable ion beam output. The Gaussian beam profile, characterized by a concentrated intensity and energy at its central peak, provides stability and enhanced spatial resolution when focused on smaller spot sizes. Furthermore, the Gaussian beam concentrates a larger proportion of light near the center. This characteristic reduces losses during beam expansion and transport, resulting in more efficient and effective beam propagation.

Figure 4.2 shows the initial characterization of the power of the laser and the temporal pulse shape is shown in Fig. 4.3.

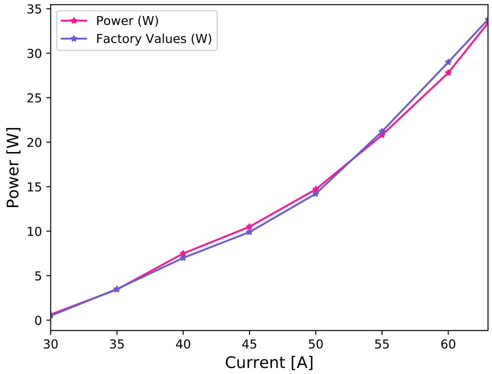

Figure 4.2: Initial characterization of the BX 80-2-G series Nd:YAG. The power-current curve at 10 kHz (internal trigger).

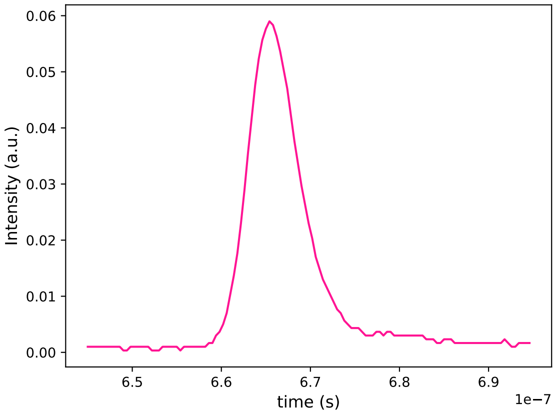

Figure 4.3: Temporal profile of the Nd:YAG Q-switched laser pulse with a FWHM pulse width of 6.4(1) ns and a jitter RMS of 1.5 ns.

Except for the cooling and dehumidifying system, the Nd:YAG components are not accessible, and the user-controlled parameters are adjustable only via the factory-recommended remote control interfaces. Therefore, an immediate solution in the event of a laser failure during an experimental run is impossible. For this, a third Nd:YAG laser (Green/UV output) has been ordered and will be installed at RIALTO.

4.2.1 Synchronization

The temporal overlap of the laser beams is crucial for the efficiency of the resonance ionization technique. To maximize the system's potential, synchronizing the output pulses of each laser with negligible jitter is essential. For this, we installed an external pulse generator (Berkeley Nucleonics Model 577 [67]) with a square-wave output that provides the 10 kHz external trigger and has 4 individual channels.

The multi-output pulse generator generates the TTL trigger signals for the pump lasers. This unit simplifies laser synchronization and does not cause a loss in the dye laser power. The timing synchronization of the dye lasers, with respect to the pump, is monitored with a photodiode connected to an oscilloscope, determining the synchronization to nanosecond precision. This is achieved by adjusting the delay on the pulse generator, which provides the Q-switch trigger for the pump laser. By adjusting the delay relative to the master trigger signal, it is possible to achieve precise synchronization of the laser pulses with minimal jitter ($<$ 1ns). This jitter primarily arises from the Q-switch electronics integrated into the laser system. Q-switching, which involves momentarily interrupting the laser's photon buildup and promptly releasing them, is a technique used to generate laser pulses that are both short and powerful.

4.3 Laser beam transport

The optical system for collimating and transporting the laser beams to the ion source was not optimal. In the initial approach, fixed-ratio beam splitters and flippable mirrors were employed to distribute the power of the Nd:YAG laser. Moreover, optical delays were introduced to adjust the beams' temporal overlap, resulting in power losses attributable to including extra optical components. To address these limitations, the Nd:YAG laser beam transport to the dye lasers and the target was redesigned to fulfill the following requirements:

- To reduce power losses and increase the laser power injected into the ion source.
- Allow switching between two different element schemes.

Now, instead of using flippable mirrors and fixed-ratio beam splitters, we changed to a combination of polarizing beam splitters (PBS, CCM1-PBS25-532-HP/M [68]) and half-wave plates (WPMH10M-532 [69]), from Thorlabs, to distribute the beams as shown in Fig. 4.1. A detailed description of these elements is provided in the following.

4.3.1 Waveplates

Optical waveplates are used as polarization rotators to transmit the light and modify its polarization without attenuating, deviating, or displacing the beam.

Waveplates are made of birefringent materials, which have different refractive indices for two orthogonal axes. This causes a velocity difference between light polarized along the wave plate's fast and slow principal axes. The fast principal axis has a lower refractive index, allowing light polarized in this direction to travel faster. Conversely, the slow axis has a higher refractive index, causing light with this polarization to travel slower. As light passes through a wave plate, this velocity difference leads to a phase shift between the two orthogonal polarization components. The actual phase shift is determined by the material's properties, the thickness of the wave plate, and the wavelength of the signal and can be mathematically described as [70]:

$$\Delta\phi = \frac{2\pi d(n_1 - n_2)}{\lambda} \tag{4.1}$$

where n_1 is the refractive index along the slow axis, n_2 is the refractive index along the orthogonal fast axis, d is the thickness of the wave plate, and λ is the signal wavelength.

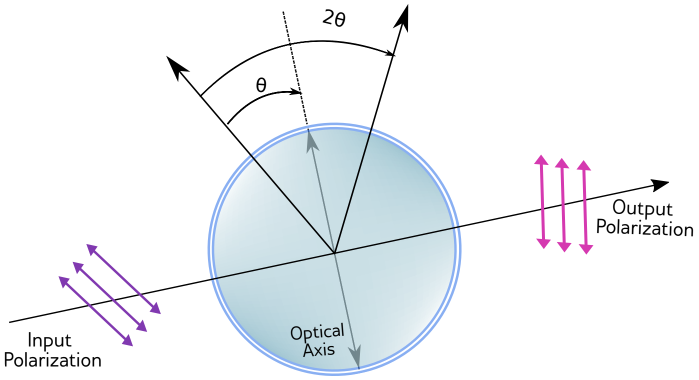

Figure 4.4: Half-wave plate. A collimated, linearly polarized beam passing through a half-wave plate with an angle θ between the waveplate's optical axis and the beam's polarization results in a 2θ rotation of the output polarization. Image adapted from [69].

When a linearly polarized beam is directed onto a half-wave plate, and the direction of polarization of the beam is not aligned with either the fast or slow axis of the wave plate, the output polarization will be linear and oriented at a different angle from that of the input beam. The angle between output and input polarization will be twice the angle between the input polarization and the wave plate's axis (Fig. 4.4). When the polarization of the input beam is directed along one of the axes of the wave plate, the polarization direction will remain unchanged.

4.3.2 Beamsplitters

Beamsplitters (BS) are optical components that divide incident light into two (or sometimes more) beams, typically at a specific ratio. Different types of beamsplitters exist; Fixed-ratio beamsplitter cubes do not rely on polarization and therefore do not modify the polarization of the two beams. As a result, the ratio of the split beams cannot be adjusted without replacing the entire beamsplitter and requiring realignment. Another type of BS is the polarizing beamsplitter cubes (PBS). These PBSs consist of two right-angled prisms cemented together, with an all-dielectric, polarization-sensitive coating on the hypotenuse of one of them. This coating enables the prism to reflect the light of one polarization state while transmitting the light of the other (Fig. 4.5). When light (unpolarized or polarized) enters the polarizing beamsplitter cube, it splits into two beams. The p-polarized light is transmitted through the cube, while the s-polarized light is reflected at a 90-degree angle (p-polarized -from the German parallel- light has an electric field polarized parallel to the plane of incidence, while s-polarized -from the German senkrecht- light is perpendicular to this plane). Polarizing beamsplitter cubes have high polarization extinction ratios, so they can efficiently separate the two polarization states. They allow maximum transmission of polarized light in the plane of incidence aligned with the input beam's polarization (maximum polarization). Conversely, the cube can reflect the power proportionally to the angle of the polarization to the plane of incidence for other polarization directions, reducing transmission. The transmission reaches a minimum at the perpendicular position to the maximum polarization.

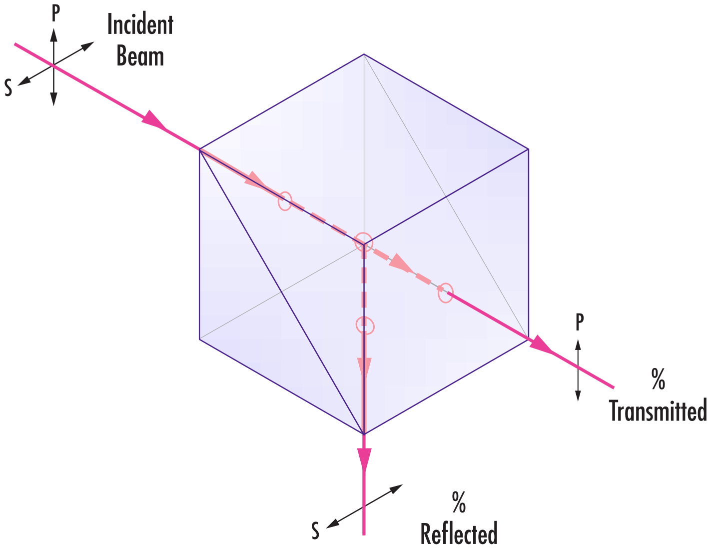

Figure 4.5: Polarizing beamsplitter. Image adapted from [71].

4.3.3 RIALTO's beam distribution

To split a polarized laser beam into two parts, a commonly used method is to use a half-wave plate to rotate the polarization to an arbitrary direction and then pass the light through a polarizing beamsplitter, as shown in Fig. 4.6. Because the half-wave plate generates a precise 180-degree retardance, the amount of power leaving each port of the beamsplitter can be smoothly adjusted to any value between 0% and 100% by simply rotating the plate. This allows for greater control over the light beam and efficient separation of the two polarization states.

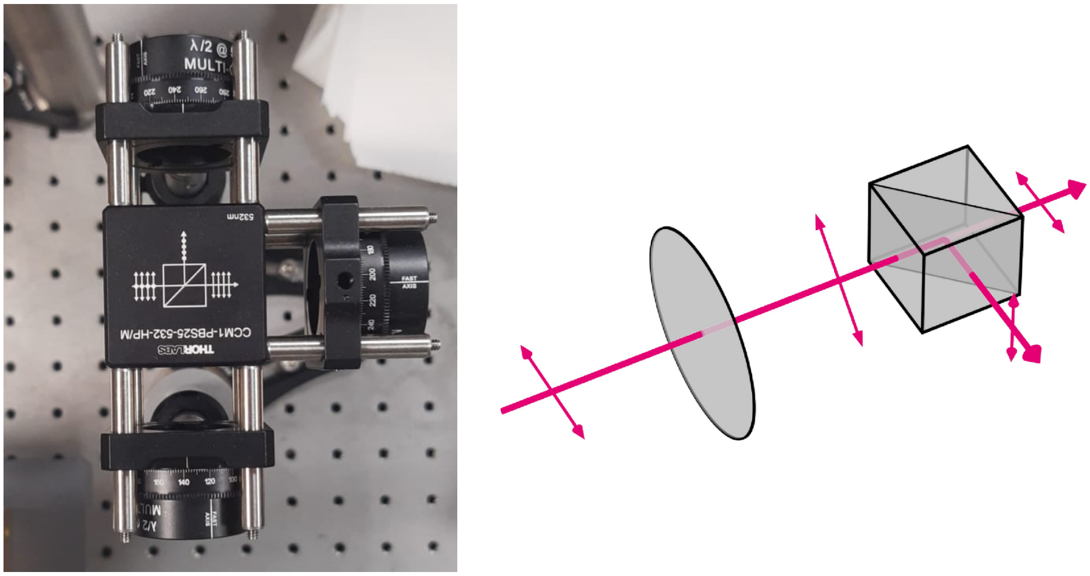

Figure 4.6: Rotating waveplate and polarizing beam splitter cube. A horizontally polarized beam is separated into its vertical and horizontal components by a rotating waveplate and a polarizing beamsplitter. Image adapted from [72].

This system functions by rotating the waveplate to change the plane of polarization of the laser light. The result is a split in the laser beam's horizontal and vertical ratio, allowing the power to be attenuated. The process begins with the half-wave plate setting the incoming laser beam to a particular polarization. If the laser beam is p-polarized, the beamsplitter cube allows the light to pass through it straight ahead. If the laser beam is s-polarized, it is reflected at a 45-degree angle, similar to how a mirror reflects light. When the laser beam's polarization is somewhere between s and p, the pump lasers split into two beams at a specific ratio depending on the angle of the half-wave plate. This allows the power of the pump laser to be controlled, sending a specific amount to each dye laser from a single pump laser without modifying the general pump power.

The combination of a polarizing beam splitter (PBS) and a waveplate also allows for reducing laser intensity while maintaining the full beam profile during the alignment of the non-resonant step (Nd:YAG) and minimizes potential hazards and the risk of exposure to hazardous levels of laser emission. Otherwise, adjusting the current to change the pump laser power can affect the timing and beam profile of the pump pulse. In our configuration, a second waveplate is placed after the PBS, which offers the advantage of readjusting the polarization state and optimizing the transmitted or produced power for all lasers.

In the non-resonant regime, the PBS becomes indispensable as the only means of attenuating a high-power pulsed laser, as alternative methods for power saturation curves are unavailable.

Additionally, this setup enables the distribution of pump power to the three different dye lasers, providing the flexibility to choose between different element ionization schemes without needing beam realignment. Nonetheless, the approximate 6% power losses resulting from the PBS's imperfect extinction ratio (Tp/Ts) are worth considering. These losses may be attributed to the elliptical polarization component of the Nd:YAG laser, which prevents complete transmission through the PBS. This extinction ratio has been measured to be 27 for the RIALTO pump laser.

4.4 Stabilization system

Laser beams tend to have spatial movements over time due to several factors, such as air temperature drifts, air density fluctuations due to air currents forming between rooms, power variations, and heating effects in optical elements and the lasers themselves. Maintaining precise laser alignment is crucial for developing a laser ion source, particularly for long-term on-line operation in high-risk experimental areas that may be inaccessible during beam time.

Because of the long distance (~ 20 m), even minor variations in the beam near the emission point can cause it to miss the downstream optics. A beam stabilization control system with steering mirrors and position-sensing detectors can mitigate these factors. For this purpose, a beam position stabilization system from the company TEM Messtechnik (Aligna/BeamLock 4D) was integrated into the beam path of the laser. The system can stabilize the laser beam position and angle by compensating for the factors mentioned earlier using a four-dimensional stabilization; two translational degrees of freedom in the plane perpendicular to the propagation direction and two rotational degrees of freedom, i.e., two beam positions (X and Y) and two angles (α and β), as shown in Fig. 4.7.

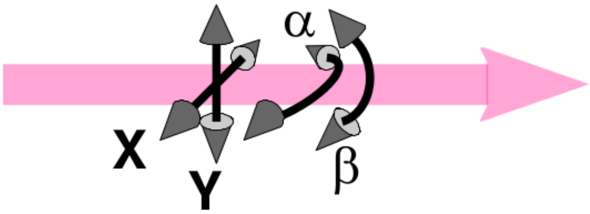

Figure 4.7: Four-dimensional degrees of freedom (DoF). The beam propagation direction here is oriented along the z-axis. The translation is represented by motion in the x and y directions, and rotation is represented by rotation through angles α and β. These four degrees of freedom of the beam are usually coupled to each other.

A change in the tilt angle of a mirror causes an angular change in the beam and a positional shift in a downstream plane perpendicular to the beam propagation. A combination of angle and position adjustments is required to correct a beam drift. This can be achieved using two mirrors, each adjustable in two directions (horizontal and vertical axis). By manipulating the position and angle of the mirrors, the laser beam can be redirected and maintained in the desired position and angle.

The system uses position-sensitive detectors (PSDs) to detect laser beam movement. The detectors are connected to control electronics, which determine the deviation of the beam position from a predetermined zero point and calculate the positional and angular displacement. The control electronics then signal two piezo-actuated mirror mounts to adjust the beam's position and angle to align with the detectors' zero point. This correction ensures the laser beam stays stable and maintains its intended trajectory.

The mirror mounts are controlled both by stepper motors and piezo actuators. The stabilization system operates differently depending on whether the motors or piezos regulate the beam. When the motors operate independently, they use the position-sensitive detectors (PSD) signals as input. Similarly, when the piezos act alone, they use the PSD signals as input. However, when combined, the piezo regulators' outputs act as the motor regulators' input [73]. This allows the piezos to compensate for all disturbances and regulate all frequencies within the system's bandwidth. When the regulator outputs reach the preset threshold, the motors begin regulating until the piezos return to their middle range. This approach ensures that the motors remain inactive and only assist when the system drifts out of range, typically taking seconds to hours.

Piezo actuators excel in faster response times and higher precision, making them ideal for correcting short and instantaneous fluctuations, while motors are better suited for addressing long-term drifts. As a result, piezo actuators are commonly used for quick and precise adjustments, while motors are employed for gradual and sustained corrections.

4.4.1 Integration in RIALTO

Despite the long optical path to the ion source, the beam stabilization system requires only two-dimensional (one detector) stabilization. The required angles for optimal performance are close to zero, and the system may experience instability if subjected to a four-dimensional mode. A schematic diagram in figures 4.8 and 4.9 illustrate how the beam position stabilization was integrated into the previous beam path. The detector system was positioned parallel to the reference tube at the same distance as the ion source from the prism in front of the mass-cycling magnet to maintain the beams' foci and avoid the use of additional lenses (section 3.2.3).

To better integrate the stabilized mirror mounts into the high-density laser-path layout, the motorized mirror mounts were installed near the output of the lasers. This decision was made due to the mounts' dimensions, making them difficult to incorporate when two laser schemes were set up in parallel. An additional mirror for the Nd:YAG system was placed in the last position available in the laser room to minimize the distance to the stabilization point (Fig 4.8).

A beamsplitter was employed to extract a beam from the reflection beam path to the reference tube and direct it into the PSD detector. Another beamsplitter guides the YAG beam into its corresponding PSD, while a prism separates the UV beam from the reflected beam and directs it to its corresponding PSD (Fig. 4.9). The uAligna controllers then utilize the position information from the beams to make the necessary corrections to the mirror mounts for beam stabilization.

PSD's offer the advantage that hitting the exact center of the detectors is not critical. They generate a linear signal proportional to the spot position within the detector area, regardless of the spot size and shape. As a result, precise alignment of PSDs in X and Y positions is not necessary. The servo loop can choose the operating point by applying an electrical DC set point signal (X and Y, α and β) to the regulator electronics. This allows the detectors to accurately detect the center of the beam and calculate an average intensity.

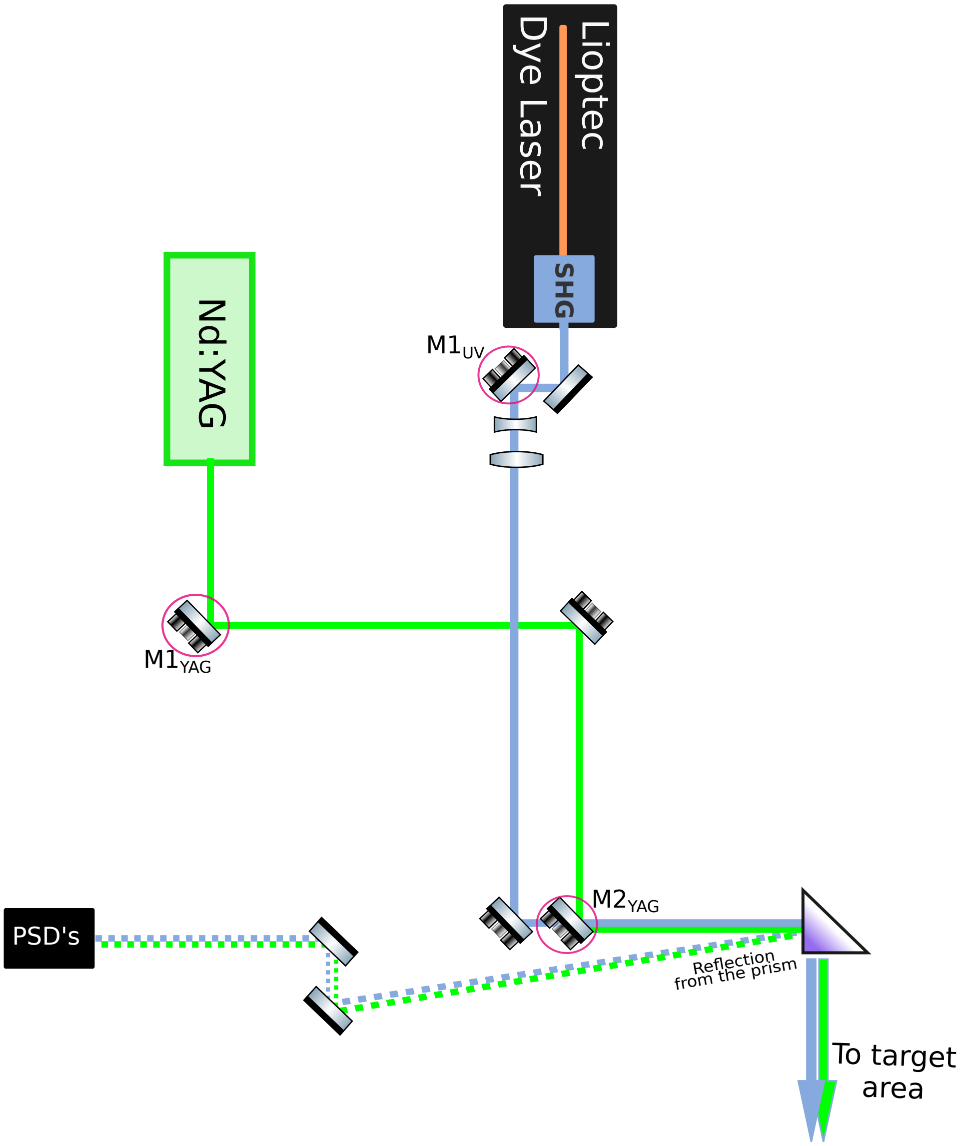

Figure 4.8: Optical layout of integrating the stabilization system to the previous beam path (not to scale). Two motorized mirrors (M1$_{\mathrm{YAG}}$, M2$_{\mathrm{YAG}}$) were added to the Nd:YAG path, and one mirror (M1$_{\mathrm{UV}}$) to the first excitation step for Ga.

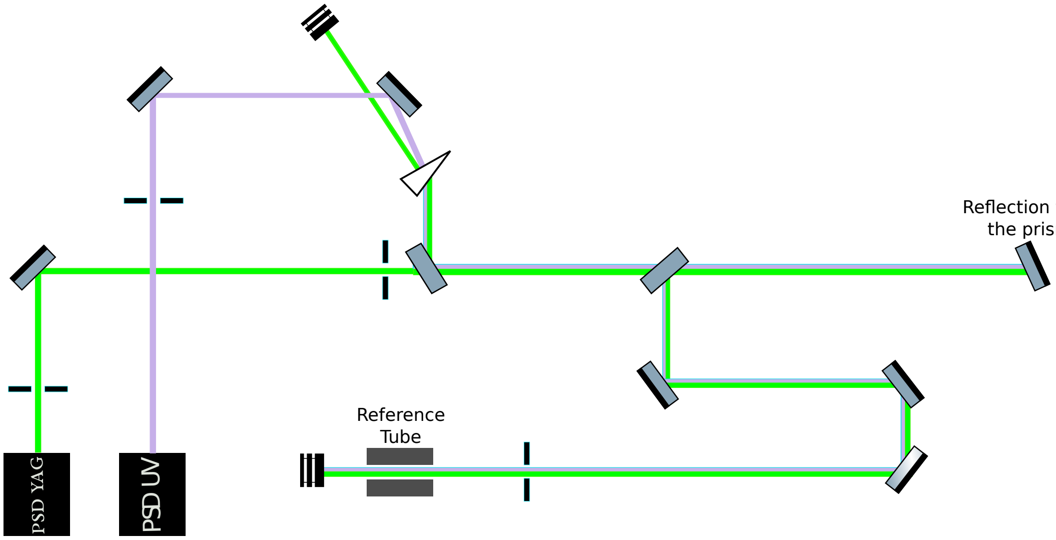

Figure 4.9: Optical layout of the reflection beam path and beam separation (not to scale). The PSDs are placed alongside the reference tube to simulate the positions of the source.

4.4.2 Kangoo software

The system's control unit enables communication and control between the detectors and mirror motors. We can customize this functionality to meet our specific requirements for the experimental setup using the manufacturer software "Kangoo".

The software features a BeamLock Basic interface that enables laser beam monitoring (Fig.4.10). This feature allows the adjustment of the reflections to the detectors and the activation of stabilization. It also enables adjustment of the experiment's parameters, such as the repetition rate of the laser to be stabilized and whether it is continuous or pulsed.

The system is equipped to detect two laser beams. However, as mentioned, in our specific setup, only 2D stabilization based on position is required, and hence only one detector is activated, rendering the other spot irrelevant. It is worth noting that the actual beam is significantly larger than the spot, the latter indicating only the center. While the spots may still exhibit some movement around the green square, the system is designed to maintain the beam's center position. Given that our experiment employs dye lasers, the apparent fluctuations in the spot position due to intensity fluctuations across the beam spot may be strong, but they are not expected to significantly impact the ionization efficiency as long as the beam's average position is close to the reference point.

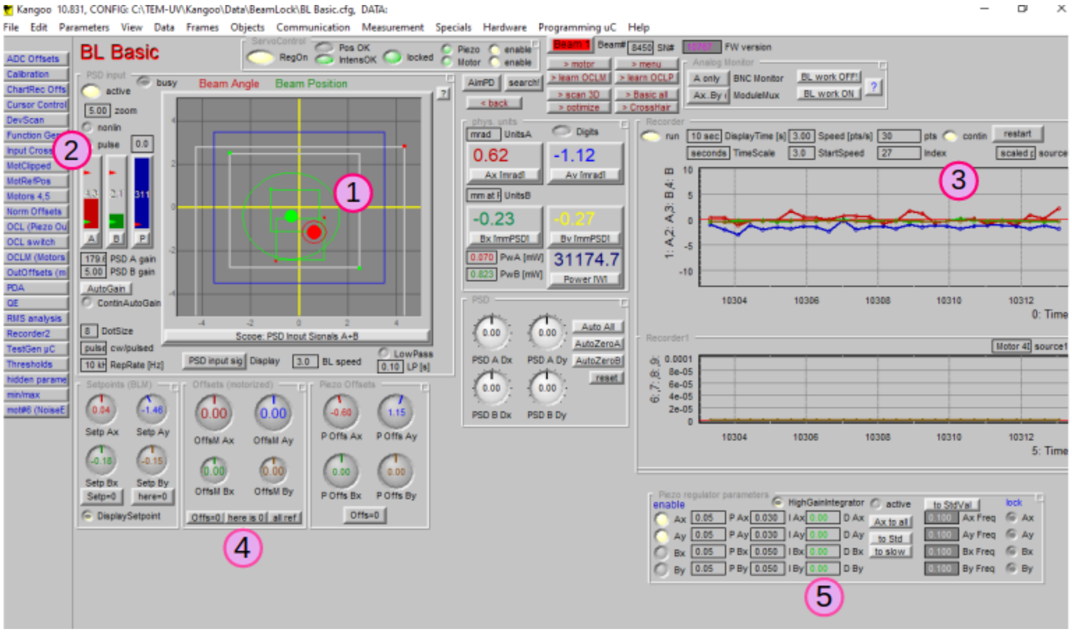

Figure 4.10: BeamLock Basic. 1) The green and red spots correspond to the actual position and angle of the beam, respectively. The green square around the spots indicates the reference position for the optimum alignment. The stabilization system tries to keep the spots in the center of this square. 2) The green and red bars are indicators of the beam intensity; a low value indicates low power or possible misalignment. 3) Shows the plot in real time of the movement of the beam. 4) Adjust the offset of the mirrors to define a "zero" position. 5) Adjustment of piezo gain.

Learning process

Kangoo offers a routine that measures the effect of all mirror axes on actual beam movements using a matrix M. The inverse of M is required to control the laser position, which is obtained through singular-value decomposition (SVD) to get the pseudo-inverse M^{-1}. The manufacturer names this matrix the “Output Crosslink matrix” (OCL), which enables the calculation of the 4-dimensional orientation of the laser beam and the orthogonalization of the system. This allows independent steering of the laser beam in all four dimensions (Fig. 4.11). A process to optimize the system can be initiated by linking the motion of the mirrors to the beam motion. This process involves determining how the mirrors should be adjusted to produce a pure angular or positional shift. The obtained information is then stored in the OCL matrix for future use.

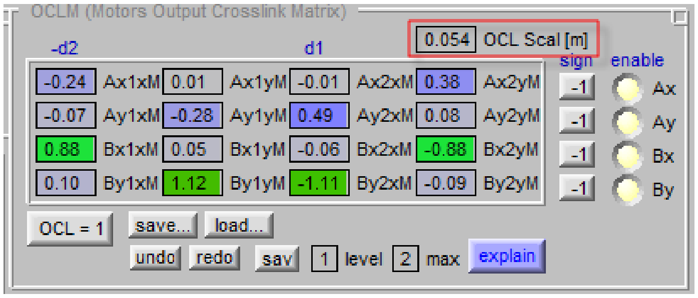

0.054 OCL Scal [m]

-0.24	Ax1xM	0.01	Ax1yM	-0.01	Ax2xM	0.38	Ax2yM	-1	Ax
-0.07	Ay1xM	-0.28	Ay1yM	0.49	Ay2xM	0.08	Ay2yM	-1	Ay
0.88	Bx1xM	0.05	Bx1yM	-0.06	Bx2xM	-0.88	Bx2yM	-1	Bx
0.10	By1xM	1.12	By1yM	-1.11	By2xM	-0.09	By2yM	-1	By

1 level 2 max

Figure 4.11: OCL matrix. Allows the decoupling of the four degrees of freedom. It defines the combination of movements of the four output actuators to achieve pure position or angle displacements.

All of the four basic beam movements (beam angle shift in X and Y “Ax”, “Ay,” beam position shift in X and Y, “Bx,” “By”) need linear combination movements of the four actuators “1x”, “1y”, “2x”, “2y” at the two moved mirrors “M1” and “M2”. These linear combinations are described by the 4x4 OCL matrix with 16 elements, as shown in Fig. 4.11. This matrix contains information on the distance between the mirrors and the detector unit and the relative mirror arrangement. In BeamLock Aligna systems with both motors and piezo actuators, there are two independent OCL matrixes, OCL (piezo) and OCLM (motors). For our 2D system, there is just one motorized or piezo-based actuator that influences the spot position, depending on which PSD (A or B) and which actuator(s) is/are used (M1, A1, or M2, A2). The resulting OCL matrix is just of the rank 2 x 2. Same for the piezo OCL.

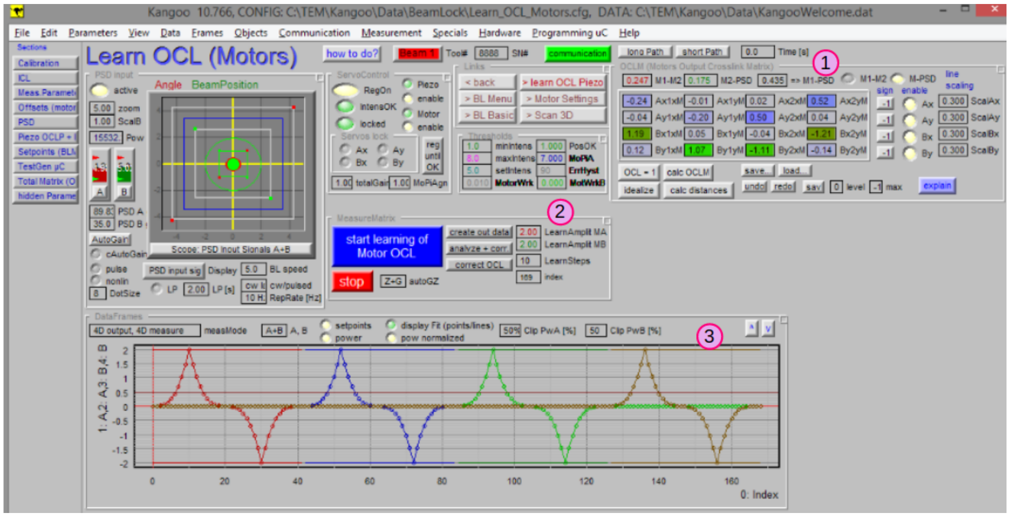

Figure 4.12: Learn OCL (Motors or Piezo). 1) Enables the calculation of the "Output Crosslink" (OCL) matrix. 2) Allows choosing the amplitude of the movements during the learning process. 3)The four triangular curves show the detector outputs (Ax, Ay, Bx, By) while the actuators perform combination movements. Ideally, an Ax combination movement only influences that detector channel, the same for the other three. In this section, we can also choose whether we work with a 2D or 4D system and which PSD is used.

Due to the significant distance between the motorized mirrors and the detector unit in the current setup, the maximum amplitude the motors are moved during the learning process should be reduced (0.2 to 0.5 in relative units in the program). This is because even small angular displacements of the mirrors can lead to substantial beam displacements on the detectors. Using large amplitude values can result in inaccuracies during the learning process, particularly when the beam is moved too far to still hit the detector. This, in turn, impedes proper beam position correction. Upon completion of the learning process, the control can be activated, and after a short settling phase, the beam is stabilized. Figure 4.12 shows Kangoo's OCL learning interface to optimize the stabilization system.

The control electronics automatically save all current parameters when switched off and recalls them the next time the system is switched on. However, the system cannot save these parameters permanently if disconnected from the mains voltage for an extended period. To solve this issue, the software includes a “User Script” feature that enables users to store all parameters, including the OCL matrix, as a preset. This preset can be loaded when the electronics are switched on, ensuring all necessary parameters are available even after a prolonged disconnection from the mains voltage.

Investigation of the beams’ position

We investigated the position stability of the laser beams, Nd:YAG (λ =532 nm) and first step excitation for Ga (λ =287.5 nm) with and without the stabilization system by monitoring the laser position after the travel distance of 20 m. The results are shown in figures 4.13 for the Nd:YAG and 4.14 for the UV beam.

As previously mentioned, the ionization tube has a diameter of 3mm, while the size of the beams ranges from 1 to 2 mm. The plots on the left side depict the beams’ behavior without the stabilization system, showing significant short-term fluctuations and long-term drifts on the order of 1 mm or more. This suggests that, during extended experiments, the beams could move beyond the tube, resulting in power or signal loss. However, we observed a complete correction of long-term drifts and a partial correction of short-term fluctuations using the stabilization system (plots on the right), leading to a more stable ion beam.

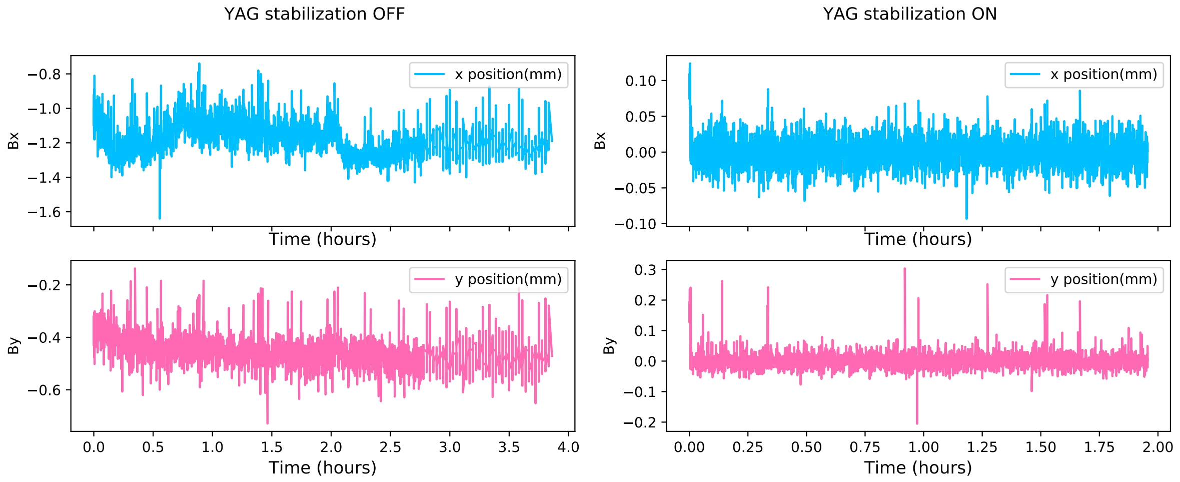

Figure 4.13: Nd:YAG position (mm) without and with the stabilization system (x position in blue, y position in pink).

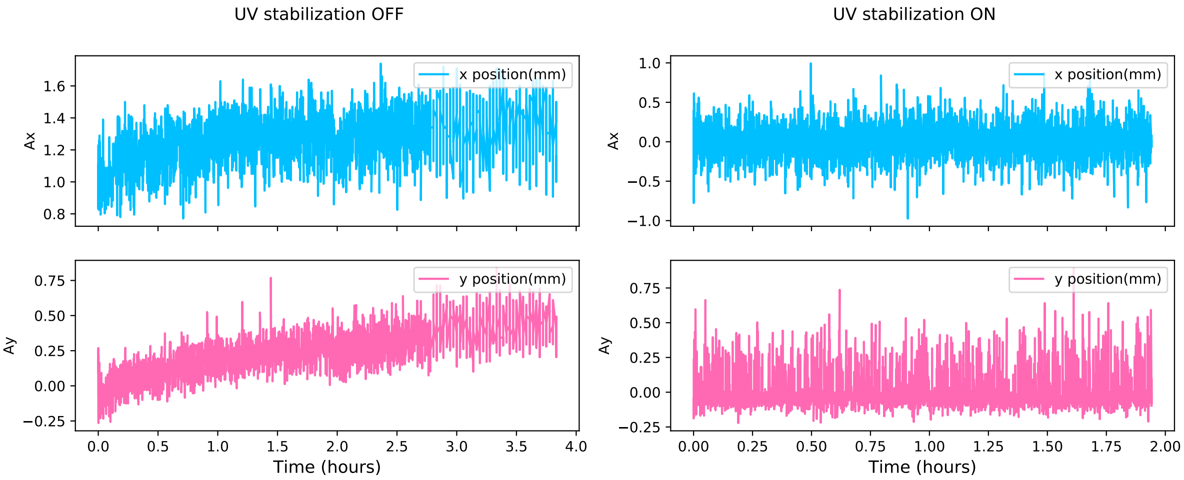

Figure 4.14: First excitation step of Ga position without and with the stabilization system (x position in blue, y position in pink).

To commission the upgrade of the RIALTO system, we produced Ag and Ga beams. A detailed description of this production will be provided in the subsequent chapters, offering a comprehensive account of the procedures and methodologies employed during the process.

Chapter 5

Implementation of a three-step laser ionization scheme of silver

Silver is one of the elements that are not produced optimally with surface ionization due to its high ionization potential of 61,106.45 cm^{-1} (7.6 eV), while with plasma ion sources, as the elements with high ionization potential are very efficiently ionized, the isobaric background would be very important. This is why resonant laser ionization was chosen to produce it.

The nuclear structure study of radioactive neutron-rich silver isotopes and the isotopes in the region of the N=Z line has been of considerable interest for several years. The silver isotopes accessible at ALTO will be used to study beta-decay properties of neutron-rich Ag isotopes towards the r-process path [42] and for high-precision mass measurements in the silver isotopic chain for an accurate determination of the nuclear binding energy [38]. A more detailed description of the neutron-rich silver program for ALTO is given in section 7.2.

5.1 Silver ionization scheme

We used a 3 step-3 color scheme to ionize silver with a non-resonant last step as shown in Figure 5.1. This scheme has been developed by RILIS at ISOLDE, and a maximum efficiency of 14 % was reached [74]. The first transition is an excitation of the electron from the electronic ground state $4d^{10}\,5s^1\,S_{1/2}$ to the intermediate excited state $4d^{10}\,5p^1\,P_{3/2}$. For this step, the UV laser with a wavelength of 328.16 nm is used. The second step is the ionization from the $4d^{10}\,5p^1\,P_{3/2}$ to $5d^1\,\mathrm{D}_{5/2}$ level with a wavelength of 546.7 nm and finally from this level to the continuum using non-resonant ionization with a Nd:YAG laser with 532 nm wavelength.

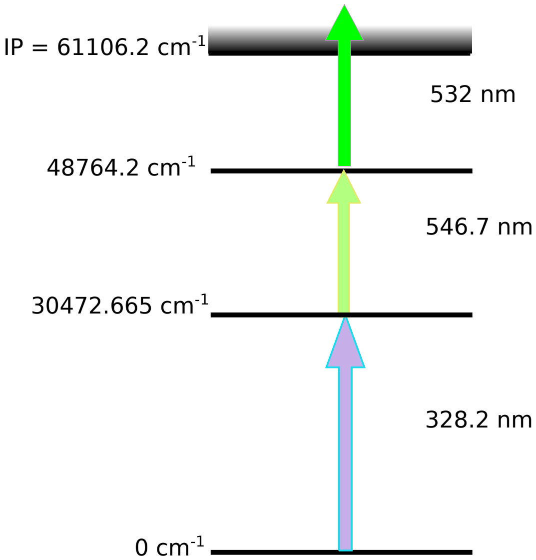

Figure 5.1: Silver ionization scheme using a two-step resonant excitation followed by nonresonant ionization [50].

The laser system used for Ag consists of the two Radiant dye lasers pumped by a high-power Nd:YAG. The first step was generated by the use of a BBO non-linear crystal. The laser light is focused on the crystal, and then we optimize the crystal angle, crystal position, and laser focus until achieving maximum power for the UV beam. This scheme poses two significant challenges. The first step (328.2 nm) must be generated with sufficient energy to saturate the level, while the second step (546.7 nm) is located at the operational limit of a 532 nm pumped dye laser. Tuning this wavelength is particularly difficult due to the high Amplified Spontaneous Emission (ASE) level and its proximity to the pump wavelength.

The dye used for generating the fundamental wavelength (λ =656.326 nm) for the first excitation step (λ =328.2 nm) was DCM with a concentration of 0.176 g/l in DMSO for the oscillator and DCM with a concentration of 0.096 g/l in methanol for the amplifier.

For the second step (λ =546.7 nm), the dye used for the oscillator was fluorescein with a concentration of 0.642 g/l plus a 200 mg of NaOH dissolved in methanol added to the volume, while for the amplifier, the fluorescein had a concentration of 0.349 g/l in ethanol plus 200 mg/l of NaOH.

5.2 Offline silver production

To evaluate the efficiency of the chosen silver ionization scheme, we used the Atomic Beam Unit (ABU, section 3.2.4) that provides a well-collimated beam of atoms evaporated from a hot cavity into a high vacuum environment.

We prepared a sample of silver by adding 75 μl of Ag solution on a 1 cm^2 tantalum foil. With the help of a normal lamp, we let the sample slowly dry for about 8 hours. Afterward, the foil was folded several times to fit in the crucible: we folded it two times from the center of the square and then rolled it, starting from the open side of the square, and placed it into the graphite tube (Fig. 5.2).

The ionization chamber of the ion source is a 30-mm long graphite tube of 3 mm inner diameter and 1.6 mm thick wall, which acts as a capillary cavity and is resistively heated to high temperatures.

As in previous uses of the ABU oven, we installed a Ta shield that surrounds the graphite tube. This shield was made with a thin foil (30 μm) of Ta; we made three turns around the tube and held it with Ta wire, avoiding touching the Ta filament as shown in Fig. 5.2.

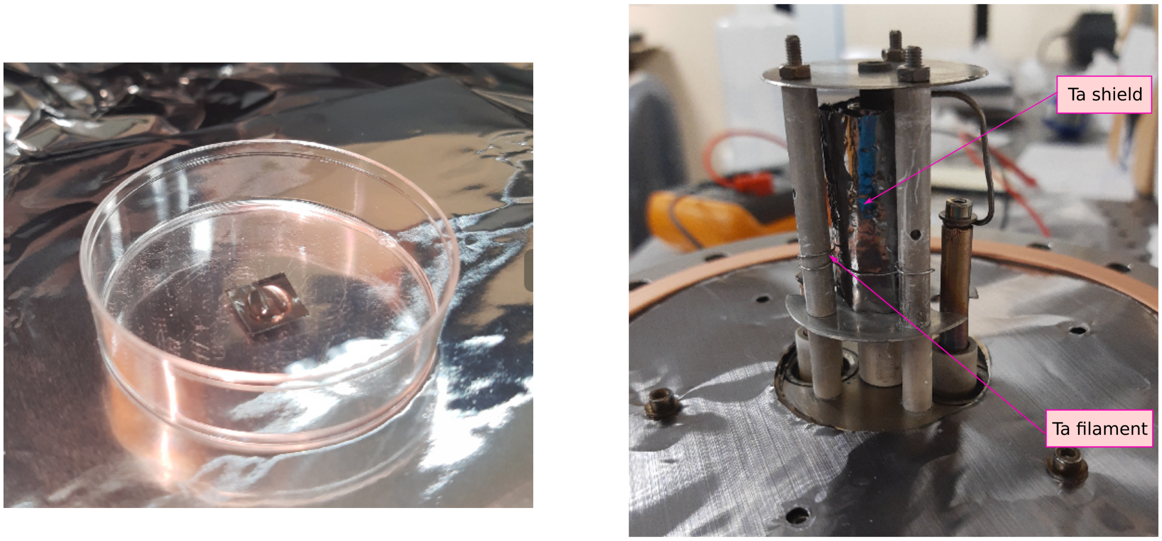

(a)

(b)

Figure 5.2: Silver preparation. Figure a) shows the silver sample dropped into the Ta sheet. In b), we can see the ionization graphite tube with the Ta shielding.

This method of folding and placing the sample with the shielding allows an exceptionally high temperature and uniform temperature distribution of the ionizer tube, resulting in highly reproducible sample evaporation and precise vapor pressure control.

The whole ensemble was placed under vacuum and pumped for 24 hours to reach the high 10^{-8} mbar range before heating the oven.

To achieve the necessary vacuum conditions for the experiment, the system must undergo a bake-out process to remove residual gases, mainly water, that are adsorbed to the chamber walls. The first heating cycle of the oven was slower than usual as it was also employed as a bake-out step, providing sufficient time to remove water and other impurities. As a result of outgassing, the pressure in the chamber increased to 10^{-6} mbar. The water was gradually desorbed at temperatures ranging from 200 °C to 400 °C and pumped away until the pressure returned to 10^{-8} mbar.

Using an optical pyrometer, we performed a temperature versus electrical current calibration to estimate the oven temperature. By focusing on the tip of the graphite tube through the lateral viewport, we obtained an initial reading of ~ 349 °C. Consistently we started to see some ions at around 10 A of heating current (~ 650 °C). Additionally, we measured the temperature as a function of the heating current, both with and without the presence of Nd:YAG; we noticed a heating effect of the Nd:YAG of ~ 200 °C when hitting directly into the graphite tube.

During the measurements, the sample was vaporized under vacuum (10^{-6} mbar) using a resistive heating current of approximately 13 A (~ 900 °C). The multiplier gain is approximately 10^5. Fast negative ion signals from the SEM are amplified and discriminated from the background noise (~ −0.7 nA).

The voltages used for the ion-optical elements and the detector are shown in table 5.1. The applied voltages have been optimized experimentally to provide the maximum ion counting rate on the SEM.

Detector		Electrostatic Lenses	
Voltage (V)	SEM lens (V)	Big plate (V)	Small plate (V)
−1400	−250	0	35

Table 5.1: ABU typical values for the ion-optical elements (Fig. 3.15).

In order to maximize the efficiency of the ionization process, all laser beams must be overlapped in space and time inside the ion source. The laser beams must be focused at the oven for a total distance of around 4 meters. Each excitation step has an independent optical path with optics adapted to the required wavelength.

We made the geometrical alignment of the beams with the chamber open, using mirrors and a telescope to control the size of the beams and focus on the interaction region. We utilized a low-pass dichroic mirror to combine the two resonant steps beams, which offered the advantage of residual reflection/transmission of the UV/green beams, respectively. This residual feature allowed us to obtain reference points outside the ABU, an essential component of our beam alignment and focusing process.

To measure the temporal overlap, we used diodes installed in front of each viewport and an oscilloscope to monitor the signals. In each case, we used the second step as our reference signal. For the UV measurements, we placed the diode at the chamber entrance. In the case of the Nd:YAG measurements, we installed a mirror at a 45° angle and used it as an attenuator to direct the transmitted beam into the diode. We conducted these measurements at the operational current of 59 A because we observed that varying the pump laser current led to an earlier relative emission from the dye lasers, resulting in changes to the beams' arrival time. The ABU temperature was around 1000 °C.

We initially obtained a maximum power of 400 mW for the second step ($\lambda = 546.7\,\mathrm{nm}$) and 330 mW of UV ($\lambda = 328.2\,\mathrm{nm}$) for the first step. When we performed the measurements, the power was of 40 mW for the UV, 300 mW for the 2nd step, and about 20 W for the non-resonant step at 532 nm. Each window from the ABU viewports has an absorption of 16% for the UV and 4.8% for the green/Nd:YAG.

5.2.1 Wavelength scan

The ABU allows tuning the different laser wavelengths by measuring the current of the ions of interest obtained by the interaction of lasers and an atomic beam.

We performed laser wavelength scans over the first and second excitation steps to verify the atomic transitions' frequencies in the Ag ionization scheme. The measurement was made by scanning the wavelength of an atomic transition while the other was kept at a fixed frequency.

We studied the ion intensity as a function of the wavelength, as shown in Fig. 5.3. We found that the optimal wavelength for the transition is, 328.162 nm for the first excitation step and 546.702 nm for the second one.

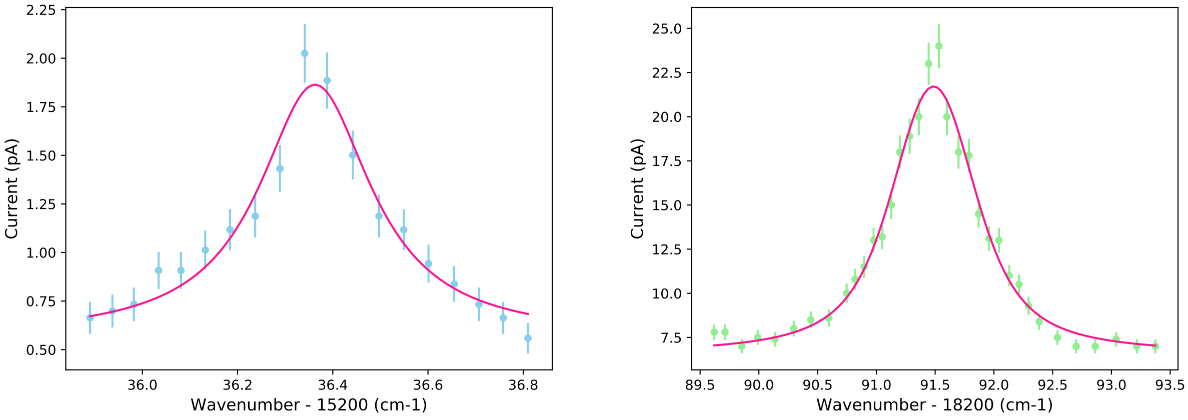

(a) First resonant step.

(b) Second resonant step.

Figure 5.3: Wavelength scans of the resonant steps for the ionization scheme of silver. a) First resonant step with center fundamental wavenumber 15236.362(9) cm^{-1} corresponding to the second-harmonic wavelength λ =328.162 nm, and b) second excitation step with a center wavenumber 18291.486(1) cm^{-1} which corresponds to λ =546.702 nm. The pink line represents the best Voigt fit to the data points.

5.2.2 Power saturation measurements

The saturation requirement of a resonant transition is determined by varying the laser power provided to the ion source for the transition and measuring the ion current, keeping all other experimental parameters (laser beam positions and wavelengths, ion source and mass marker heating, and the laser power delivered for the other applied transitions) constant.

In order to measure the efficiency of the transitions, we performed saturation measurements. We measured the ion current intensity as a function of the laser power. It is essential to know the saturation behavior of the excitation steps in order to estimate the influence of changes in the laser power on the ionization efficiency during ion-beam production.

For measuring the power saturation, the laser power for the respective excitation step was varied using filters placed in a filter wheel, and the attenuation was measured with a power-meter to calibrate the filters for each used wavelength. The other involved transitions were kept saturated during each measurement. The equation 5.1 describes in good approximation the dependence of the ionization efficiency on the laser powers and is used to fit the measured values of Fig 6.4. This function relates the signal, $I(P)$ to the laser power, P, delivered for each resonant transition by determining a saturation parameter [75]:

$$I(P) = a\frac{\frac{P}{P_{\text{sat}}}}{1+\frac{P}{P_{\text{sat}}}} + \beta P, \tag{5.1}$$

where β is a constant factor, a is the maximum ion current with a fully saturated transition, and P_{sat} is the saturation power. The first term describes the behavior of the ion current in saturation of a resonant transition, while the second term adds a linear dependence caused by possible non-resonant ionization.

The count rate of silver ions was measured before, during, and after the attenuation of the laser power to account for possible variations in the evaporation rate from the filament.

In Figure 5.4, we can observe the saturation behavior exhibited by both excitation steps. It becomes evident that while we did not achieve complete saturation using the power output of our lasers, the energy supplied was adequate to yield nearly maximal ionization efficiency. Moreover, the power proved to be sufficient for facilitating on-line ionization processes. These findings are complemented by the data presented in Table 5.2, which outlines the saturation power (inflection point in the curves) corresponding to each transition and the maximum power attainable at the laser ion source.

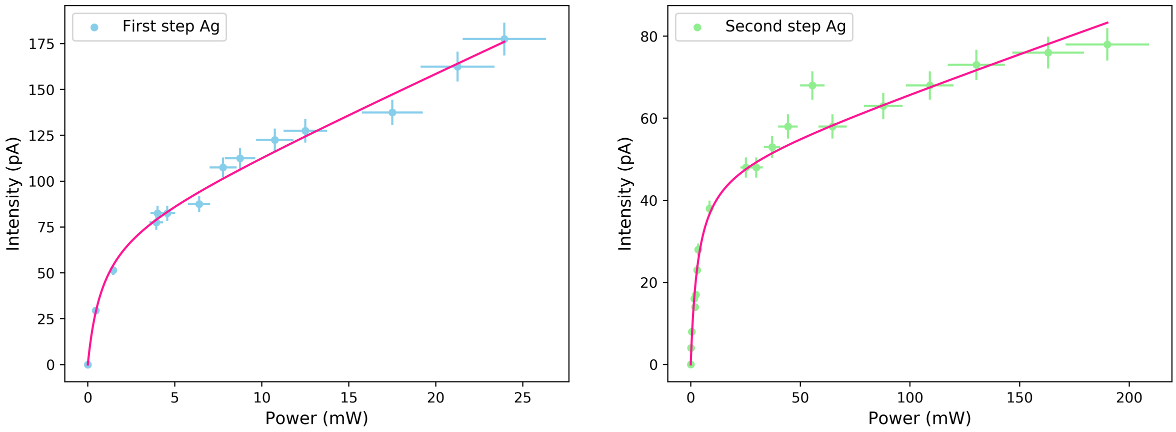

(a) Saturation power P=0.8 ±0.1 mW.

(b) Saturation Power P=3.3 ±0.8 mW

Figure 5.4: Saturation curves for the two resonant steps of silver. The uncertainty on individual measurement points is related to the measurement devices' precision and the recording method. The pink line is the saturation curve fit by Eq. (5.1).

	P_{Sat} [mW]	$P_{\text{Max Available}}$[mW]
First step	0.8	40
Second step	3.3	300
Non-resonant step	n/a	20000

Table 5.2: Saturation and available power of the silver ionization scheme.

We measured the laser on-off effect. Table 5.3 details the effects of blocking the different laser transitions.

L1	L2	YAG	Current (pA)
⋆	⋆	⋆	−110
	⋆	⋆	−14
⋆		⋆	−14
⋆	⋆		−24
		⋆	−14

Table 5.3: Lasers effect on silver, with a heating current on the graphite tube of 11 A. First step power 29 mW, second step power 310 mW. When we block one or both ionization steps, we see a background signal of 14 pA. The pink stars represent which laser we are using.

We observed that the first step or the second step in the scheme are critical since blocking one of these transitions results in the disappearance of the ion signal. However, when the second resonant transition is included, approximately 9.6 % of the total ion signal is achieved, demonstrating that the second step provides sufficient energy per photon to ionize. By using all three lasers, we observed an enhancement of 100 pA due to the YAG laser.

Additionally, we noticed that the YAG laser has a heating effect that may introduce instabilities in ion production and create an ambiguous laser on/off effect. Blocking the YAG laser would also instantaneously reduce the temperature of the graphite tube, where the heating effect of the YAG laser is estimated to be around 200° Celsius.

5.2.3 Nd:YAG Synchronization

While optimizing the Ag ionization scheme, we measured the relationship between pulse synchronization and ion current. The aim was to evaluate the sensitivity to desynchronization and understand the acceptance range of jitter in the system.

We measured the resonance ionization signal as a function of the time delay of the non-resonant step; the result is shown in Fig. 5.5. The possible jitter between the two laser systems does not limit the ionization efficiency.

The Einstein coefficient A represents the spontaneous emission rate (s^{-1}), indicating the probability per unit of time for an excited electron to do a transition between states. The state's lifetime can be approximated as the reciprocal of the transition rate (1/A) [47]. When there is close agreement between the decay time and the state's lifetime, it means normal excitation behavior in vacuum. However, a significant difference suggests the involvement of additional processes, such as collisional de-excitation. In such cases, the decay of the excited state occurs faster than expected based on the Einstein coefficient.

Regarding the state $5d^1\,D_{5/2}$, the reciprocal of the Einstein coefficient A is 11.62 ns [76]. In our measurements, shown in Figure 5.6, we found a 14.1(1) ns decay time. This suggests that our findings align with theoretical expectations.

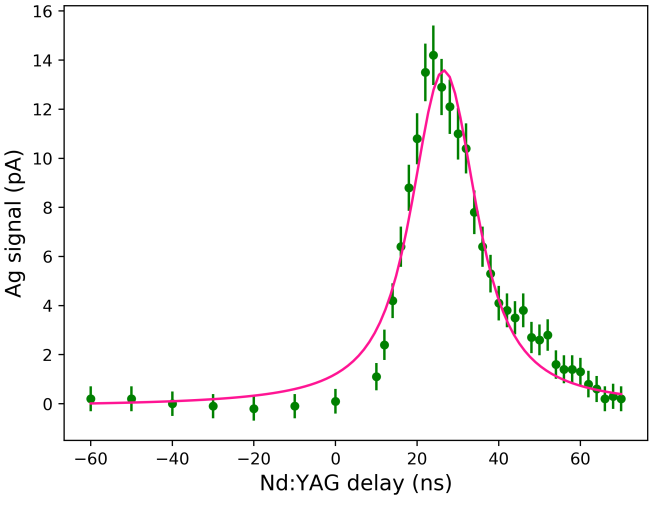

Figure 5.5: Synchronization of the Nd:YAG and the dye laser system. The trigger signal sent to the pump laser was delayed within a range of around 130 ns, and the ion current of Ag was recorded. The data were fitted with a Voigt profile. The FWHM is 18(9) ns.

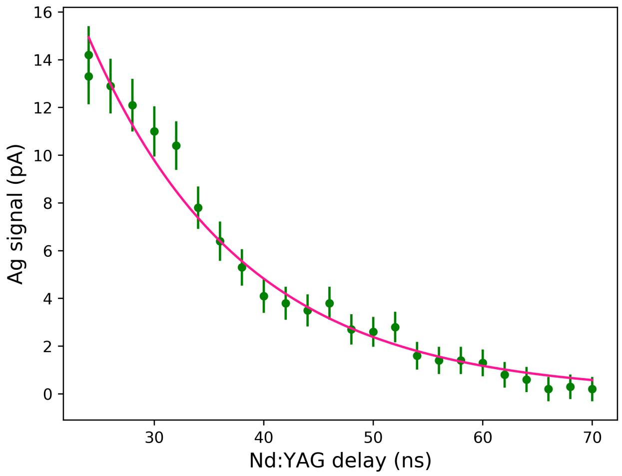

Figure 5.6: Nd:YAG decay. An exponential curve was fitted to the data. The decay time is about 14.1(1) ns, and the 1/A is 11.62 ns [76].

5.3 Online stable Ag ionization at ALTO

In October 2022, an experiment was conducted at ALTO to commission the RIALTO upgraded system with the production of Ag and Ga beams. The study used a laser-ionized radioactive beam generated from uranium fission products. Notably, this experimental campaign marks the first occurrence in the LEB section of the facility following improvements to the front end of the line as part of the FRISAL project [44].

Typically, the laser ion source parameters are optimized off-line (no electron beam on target) using a specially prepared heated sample of the element of interest. This sample is placed in a resistively heated capillary "oven" container connected to the transfer line of the target unit (see Fig. 5.7). An independently controlled oven provides a reliable and adjustable supply of the element during the experiment, facilitating initial and regular optimization of laser parameters. The oven is heated to ensure a steady atom supply, generating an ion current measured by a Faraday cup (CF, in Fig. 5.8). The beam positions, pulse timing, focusing, and wavelengths are then optimized by monitoring the ion current of the mass-separated beam.

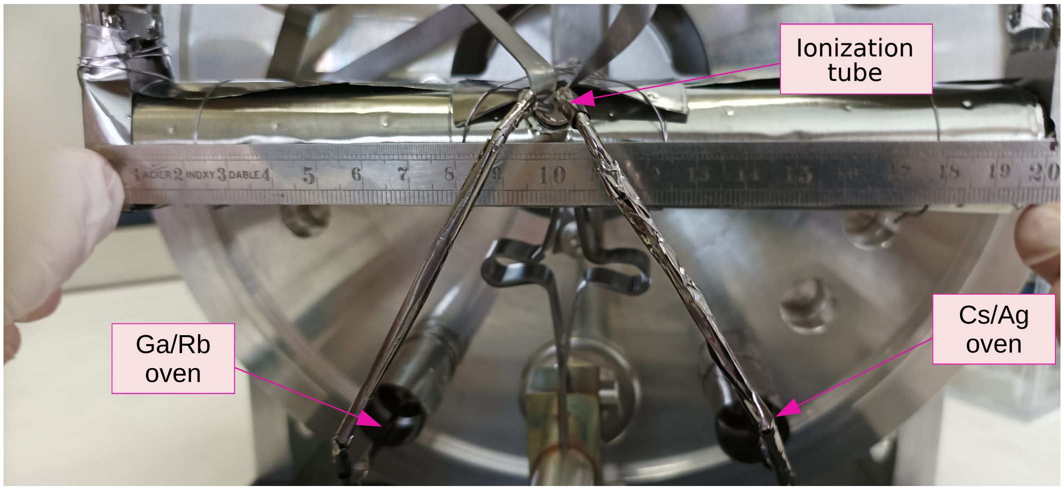

Figure 5.7: Annexe oven for stable beam test.

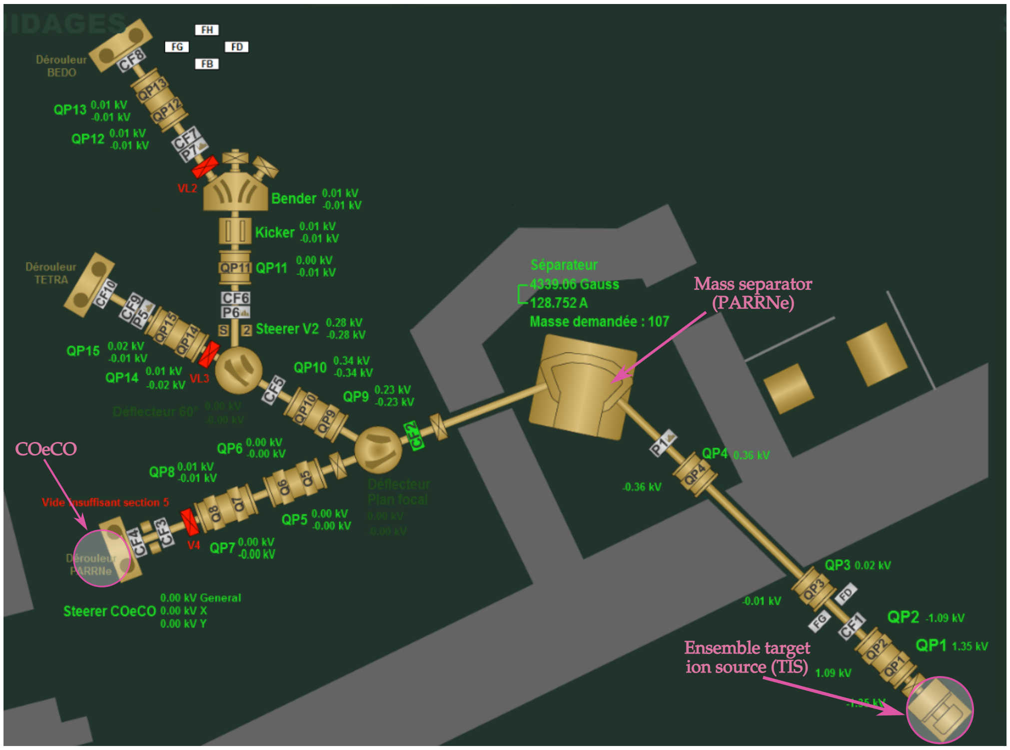

Figure 5.8: ALTO-LEB beamline schematics. The Ga test was performed in the COeCO setup (detailed information is given in 6.5).

The ALTO injection and the transport beamlines were tuned on the stable silver from the Cs and Ag target reservoir, the Ag being ionized by the laser ion source. The oven is installed and heated to initiate tracer evaporation and release into the ion source. Next, the mass separator is adjusted to the stable isotope's mass, and the transmitted ion current is monitored on a Faraday cup at the COeCo setup (CF4).

After the optimization, with the oven conditions described on table 5.4, we performed a mass scan for Ag to observe the effect of the laser ion source. Fig. 5.9 shows the two stable silver isotopes, ^{107}Ag and ^{109}Ag with natural abundances of 51.8% and 48.2%, respectively.

Oven			Cathode		
I(A)	U(V)	P(W)	I(A)	U(V)	P(W)
45	2	200	302	1.9	512

Table 5.4: Oven conditions for the stable Ag measurements.

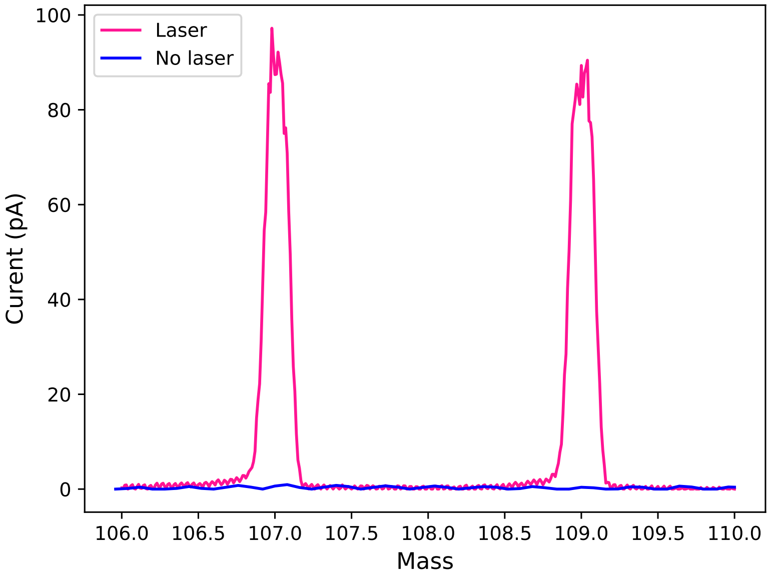

Figure 5.9: Mass scan of stable Ag. The measurements were made on the Faraday cup at the COeCO setup (CF4). The pink line shows the ion current with laser, and the blue line shows the ion current without lasers.

Due to its high ionization potential (~ 7.6 eV), Ag has a very low efficiency for surface ionization, even though the hot cavity temperature was significantly high. Table 5.5 displays the measured current for each isotope, with surface and laser ionization.

Ag	Laser Ionization Current (pA)	Surface Ionization Current (pA)
107	97.21	0.91
109	90.46	0.38

Table 5.5: Laser on/off effect for stable Ag. Measured current for the two stable Ag isotopes, with surface and laser ionization.

We noticed that only two resonant steps were sufficient to induce ionization during the off-line experimental testing at the ABU (as referred to in section 5.2). We replicated the experiment online using a stable beam to expand our results. We performed a mass scan with only the resonant steps, no Nd:YAG, and another without any laser. The outcome of this test is shown in Figure 5.10. We can see a small effect of the resonant steps (~ 0.3 pA).

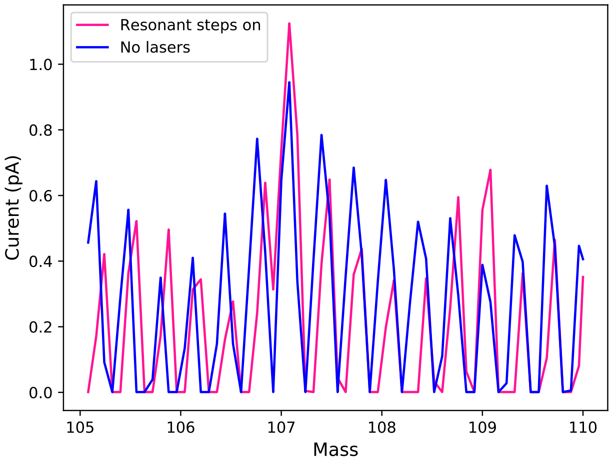

Figure 5.10: The pink line shows the ion current with the first and second step in and no Nd:YAG. The blue line shows the ion current without lasers.

In addition, we noticed a heating effect of the Nd:YAG of 10 W and performed a subsequent online experiment using a stable Cs beam to investigate this effect further. As the surface ionization method is temperature-dependent, we can see the increase in the Cs signal due to the Nd:YAG. The results of this test are shown in Fig. 5.11.

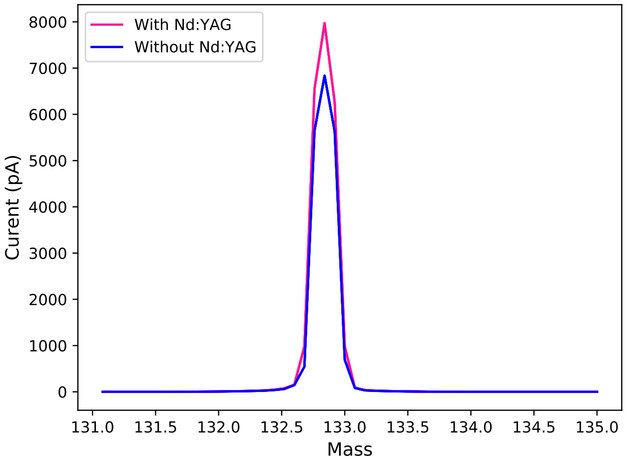

Figure 5.11: Mass scan of stable Cs. The pink line shows the ion current with Nd:YAG, and the blue line shows the ion current without Nd:YAG.

The saturation of each transition level is desired for efficient ion production. Figure 5.12 shows the measured silver ion beam current as a function of the laser power in the hot-cavity ion source for each resonant excitation step.

In contrast to Figure 5.4, Figure 5.12 reveals enhanced saturation behavior, which can be ascribed to the distinct geometries of the two sources. While the ABU configuration permits ions to move freely within the vacuum chamber, the cylindrical confinement of the hot cavity source results in significantly improved saturation behavior.

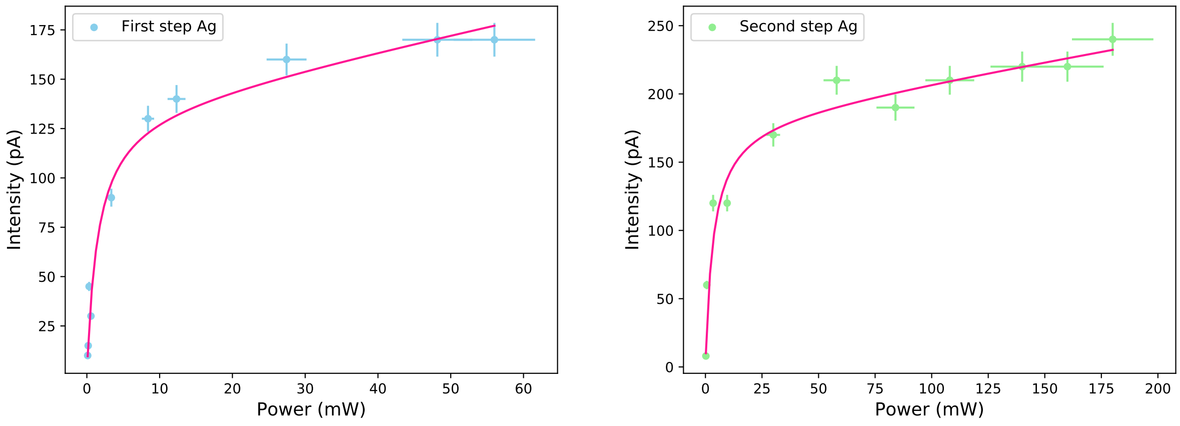

(a) First step saturation power P=1.5 mW±0.4 (b) Second step saturation power P=3.5 mW±1.1

Figure 5.12: Power saturation curves for the two resonant steps of silver measured on-line. The pink line is the saturation curve fit by Eq. (5.1).

The saturation powers measured online and in the ABU exhibit similar values, suggesting that the alignment is effectively achieved in the source despite being performed at different distances. The alignment quality in the source is comparable to that observed in the ABU, where alignment was easily performed.

Thanks to the installation of the PBS (see 4.3), we were able to measure the power saturation for the non-resonant step, which was not possible during the ABU test (section 5.2). The results are shown in Fig. 5.13. It is clear that the transition does not reach saturation, which is expected given its low cross-section. To achieve saturation, we need to increase the power or explore the possibility of exciting autoionizing states near the ionization potential (see 7.2.2).

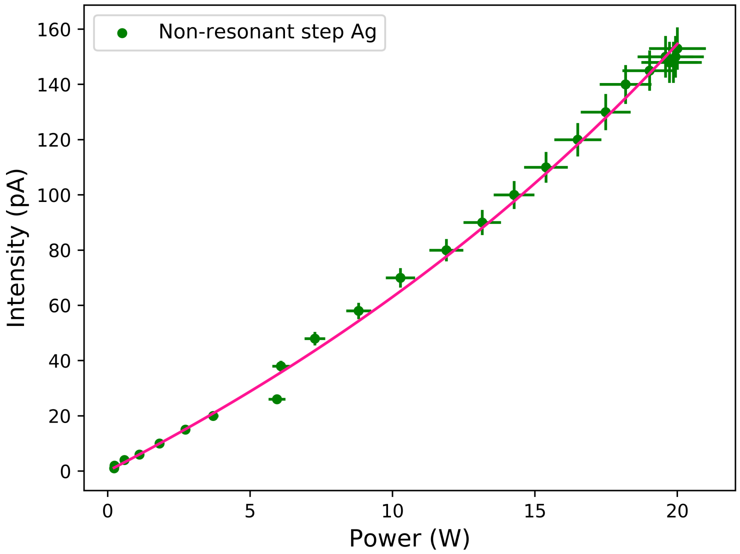

Figure 5.13: Power saturation for the non-resonant step Ag.

Table 5.6 shows the saturation power of each transition and the maximum power available at the laser ion source.

	P_{Sat} [mW]	$P_{\text{Max Available}}$[mW]
First step	1.5	73
Second step	3.5	100
Non-resonant step	n/a	20000

Table 5.6: Saturation power (from the fitting of 5.12) and available power of the silver ionization scheme.

The trigger signal sent to the pump laser was delayed within a range of about 60 ns, and the ion current of Ag was recorded; the result is shown in Fig. 5.14.

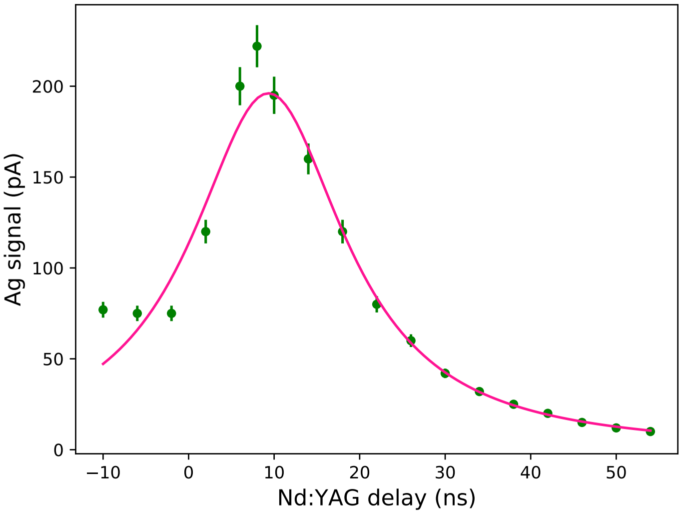

Figure 5.14: Non-resonant step synchronization online. The trigger signal sent to the Nd:YAG laser was delayed within a range of around 60 ns, and the ion current of Ag was recorded. A Voigt curve was fitted to the data. The FWHM is 19(3) ns.

As made for the offline test, we investigated the lifetime of the state $5d^2\,D_{3/2}$, the reciprocal of the Einstein coefficient A is 11.62 ns [76]. In our measurements, shown in Figure 5.15, we found a decay time of 14.15(5) ns; which is consistent with measurements performed in the ABU.

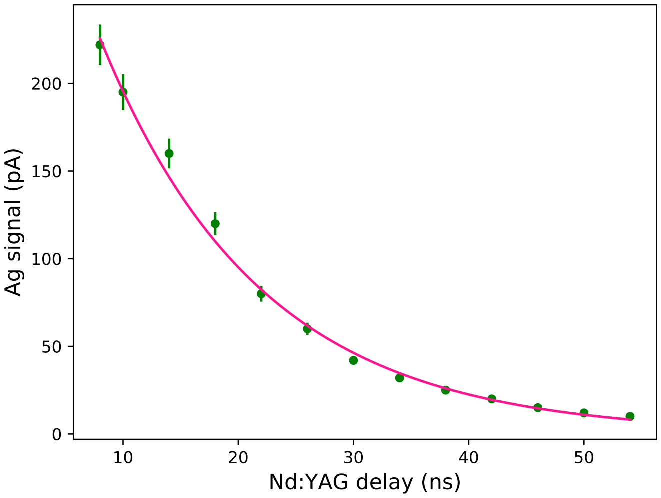

Figure 5.15: Non-resonant step for Ag decay. An exponential curve was fitted to the data. The decay time is about 14.15(5) ns, and the 1/A is 11.62 ns [76].

This work was the first-ever use of this scheme for the on-line production of Ag at ALTO. Difficulties related to the LINAC operation prevented us from performing a test with radioactive isotopes, although the laser system was ready on each occasion.

The off-line optimization of the Ag ionization scheme was done in parallel with the Ga, which will be discussed in the next chapter, allowing us to test the fast switching method with the new waveplate-PBS system (section 4.3).

Chapter 6

Production of Ga beam

6.1 Stable Ga beam

As mentioned in 5, the off-line optimization of the silver beam was made in parallel with the gallium beam. A second oven is available at ALTO to test both schemes (Fig. 5.7).

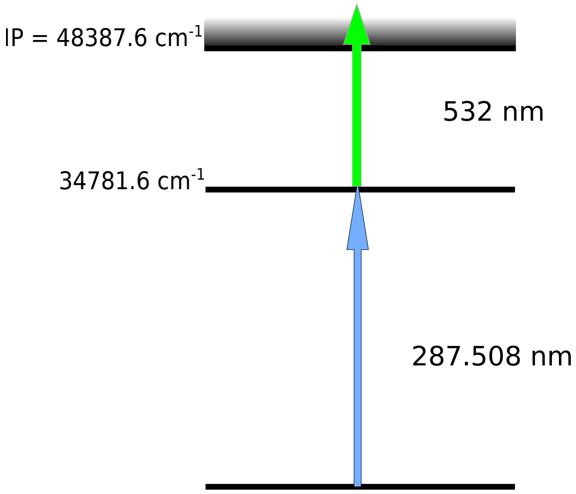

Figure 6.1: Gallium ionization scheme [50].

We used a two-step scheme to ionize Gallium (Fig. 6.1). This scheme has been developed with RILIS at ISOLDE [50, 77]. The first transition is an excitation of the electron from the electronic ground state $4s^2\,4p^1\,P_{1/2}$ to the intermediate excited state $4s^2\,4d^1\,D_{3/2}$. For this step, the UV laser with a wavelength of 287.5 nm is used. The second step is the ionization from the $4s^2\,4d^1\,D_{3/2}$ level to the continuum using a Nd:YAG laser with 532 nm wavelength.

The laser system used for Ga consists of one dye laser (Lioptec) pumped by a high-power Nd:YAG. Lioptec dye laser was used to generate the first step with the help of the BBO non-linear crystal in its FCU unit. The dye used for generating the fundamental wavelength ($\lambda = 574.8$ nm) for the first excitation step ($\lambda = 287.5$ nm) was Rhodamine 6G in ethanol with a concentration of 0.12 g/l for the oscillator and a concentration of 0.04 g/l for the amplifier.

As made for the production of stable Ag, the ALTO injection and the transport beamlines were tuned on the stable gallium from the Rb and Ga target reservoir, Ga being ionized by the laser ion source. The oven is installed and heated to initiate tracer evaporation and release into the ion source. Next, the mass separator is adjusted to the stable isotope's mass, and the transmitted ion current is monitored on a Faraday cup at the COeCo setup (CF4 in Figure 5.8).

The laser foci and positions were adjusted to maximize the ion signal on stable ^{69}Ga from the Ga and Rb target reservoir. The signal is measured in a Faraday cup (CF4) just before the collecting point in the COeCO setup. The transmission of the UV beam to the ionization tube was 78%, with 125 mW at the source and 71%, with 20 W for the Nd:YAG.

After the optimization, with oven conditions of table 6.1, we performed a mass scan for stable Gallium to observe the effect of the laser ion source (Fig. 6.2). The figure shows the two peaks corresponding to two stable Ga isotopes, ^{69}Ga and ^{71}Ga, with natural abundances of 60.1% and 39.9%, respectively. The ratio of laser ionization/surface ionization is very high, suggesting that the ionization tube was not hot enough to enable Ga release.

Oven			Cathode		
I(A)	U(V)	P(W)	I(A)	U(V)	P(W)
780	3.1	3100	200	1.9	400

Table 6.1: Oven conditions for the stable Ga measurements.

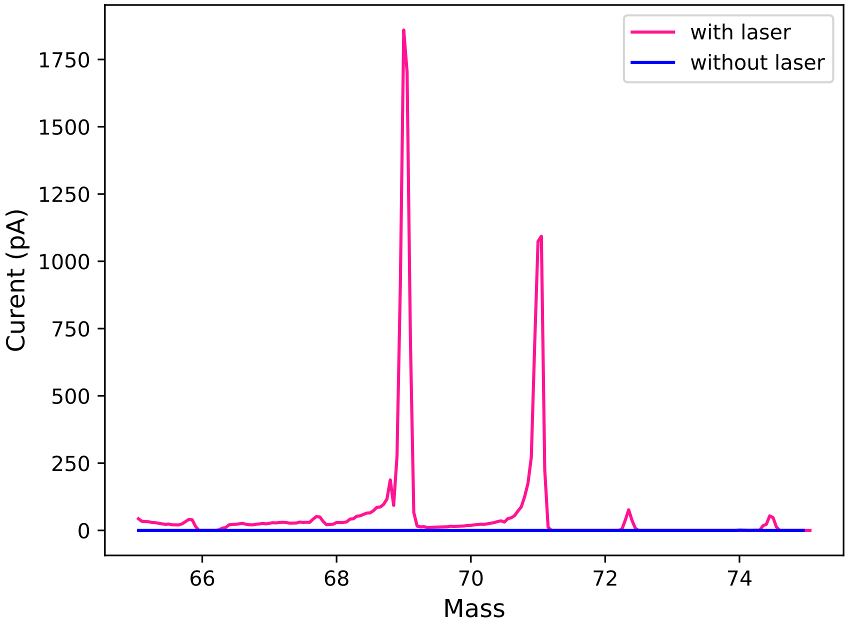

Figure 6.2: Mass scan for stable Ga. The pink line represents the ion current measured with lasers, and the blue line the current without lasers. The hot cavity's temperature was not high enough to allow surface ionization of Ga.

A second test was made in May 2023 for beam diagnostic and transport optimization. During this test, profile measurements were performed.

ALTO is equipped with grid beam scanners that provide horizontal and vertical beam profiles in the transfer lines. A grid scanner beam profiler determines the transverse profile of charged particle beams by placing a mesh-like structure of thin parallel wires or metal plates perpendicular to the beam. The beam's intensity passing through the grid is measured for coarse beam profile measurement. We measured the Ga beam profile with and without the lasers in the beam profiler located after CF9 (Fig. 5.8), where we had a transmission of 70%; Figure 6.3 shows the results. We can see that laser-ionized and surface-ionized beams display similar profile shapes. Horizontally (X position), their sizes are nearly identical, measuring 2.952 mm FWHM without lasers and 2.951 mm with lasers. The surface-ionized beam is vertically (Y position) larger, with an FHWM of 20.17 mm, compared to 15.26 mm for the laser-ionized beam. This observation instills confidence in the alignment precision of the laser beams within the ionizer.

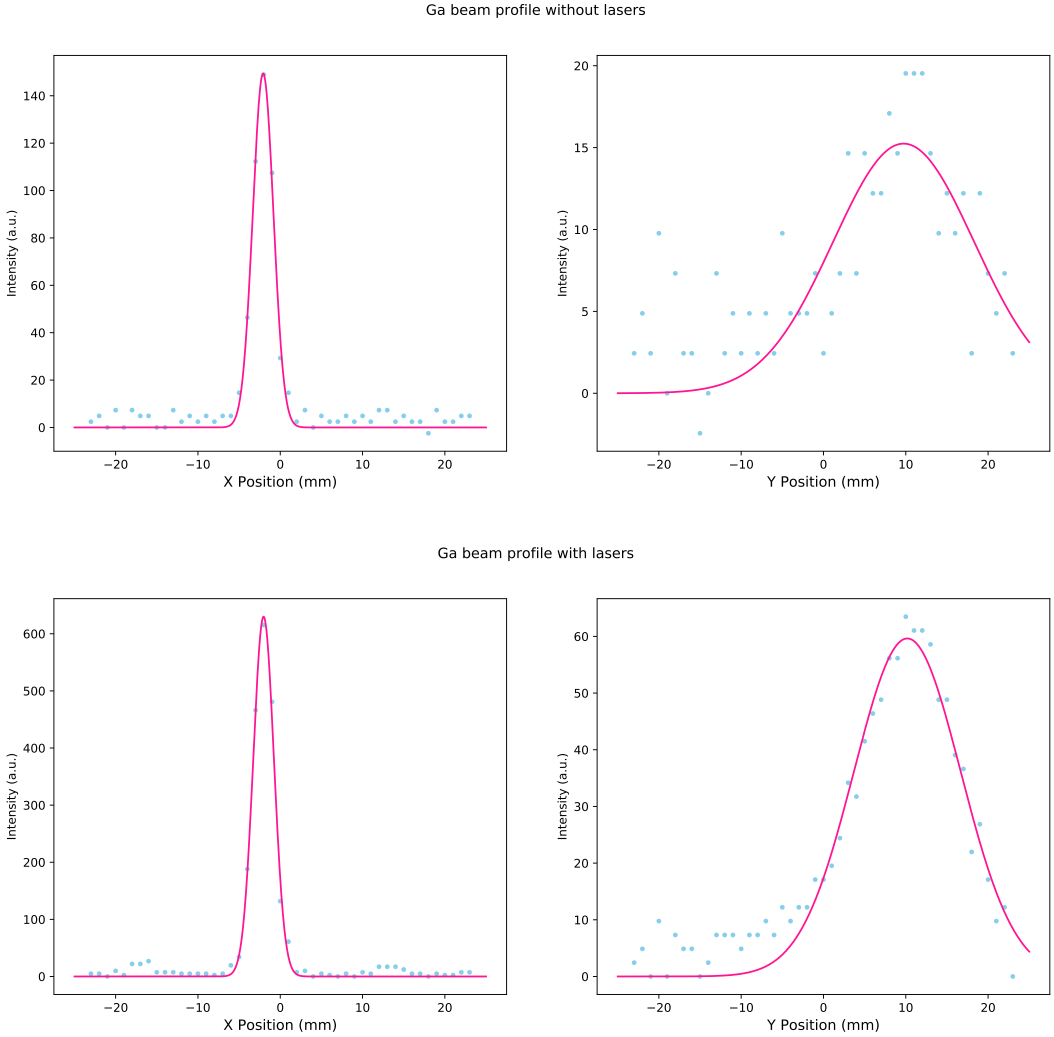

Figure 6.3: Ga transversal beam profiles. The blue points represent the measured values, and the pink line represents the Gaussian fit. For the beam produced by surface ionization, the FHWM of x position is 2.952, and in y is 20.17, while for laser ionization is, for x, 2.951 and 15.26 for y.

6.1.1 Power saturation curves

The saturation power gives an indication of the minimal required power for RILIS operation without losing efficiency. In order to obtain the saturation power, the ion current dependence of the laser power is fitted by equation 5.1.

The power saturation of both steps is shown in Fig. 6.4. From the fits, we found that the first excitation step (λ = 287.4 nm), with the saturation power of 0.48 ± 0.21 mW and we have an operation power of ~ 100 mW. The second step is not saturated; this is expected as the cross-section for non-resonant ionization is low. Table 6.2 resumes the minimal power required for the transitions and the maximum power available at the laser ion source.

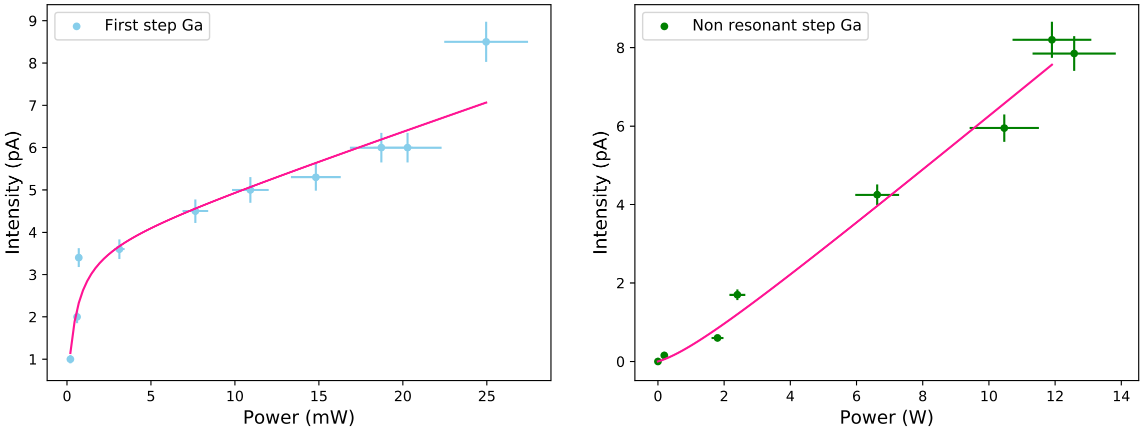

(a) λ = 287.4 nm. Saturation power 0.48 ± 0.21 mW.

(b) Non-resonant step λ = 532 nm.

Figure 6.4: Saturation curves for Gallium. The uncertainty on individual measurement points is related to the measurement devices' precision and the recording method. The pink line is the saturation curve fit by Eq. (5.1).

	P_{Sat} [mW]	$P_{\text{Max Available}}$ [mW]
First step	0.48	125
non resonant step	n/a	20000

Table 6.2: Saturation and available power of the gallium ionization scheme.

The trigger signal sent to the Nd:YAG laser was delayed in 4 ns increments in a range of 60 ns and recording the ion current of Ga, as shown in Fig. 6.6.

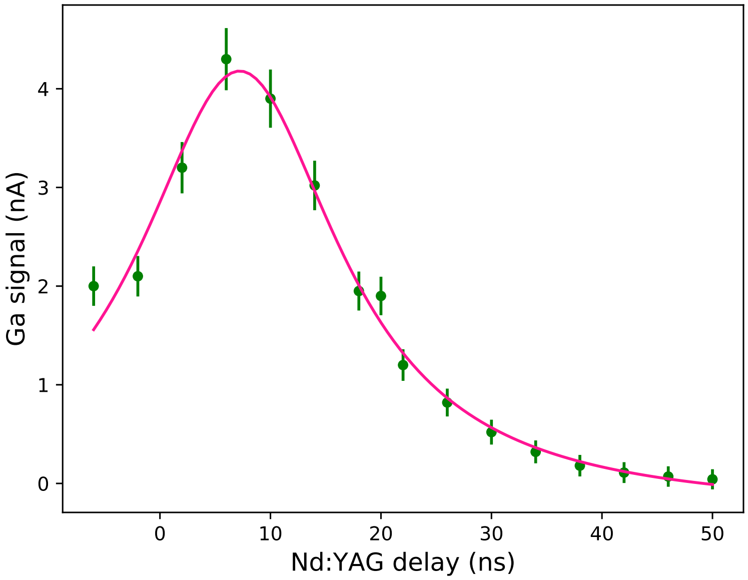

Figure 6.5: Nd:YAG delay for Ga. The green points represent the measured Ga current, and a Voigt curve was fitted to the data. The full width at half maximum (FWHM) is 21(9) ns.

We investigated the lifetime of the states and their reciprocal Einstein coefficient. For the intermediate state $4s^2\,4d^1\,D_{3/2}$, 1/A is 8.54 ns [76], and we found (from Fig. 6.6) a decay time of 9(1) ns, which means that our measurement is coherent with the expectation.

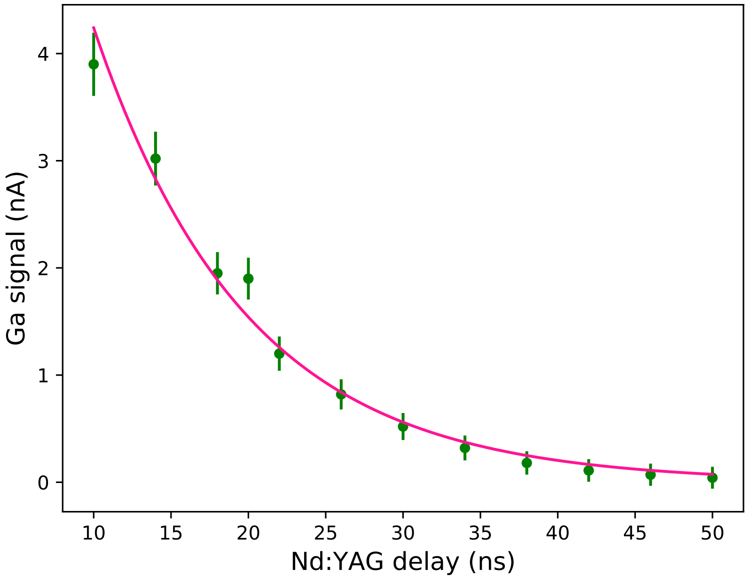

Figure 6.6: Nd:YAG decay. An exponential curve was fitted to the data. The decay time is about 9(1) ns, and the 1/A is 8.54 ns [76].

6.1.2 Radioactive Ga test

During this experiment, we tested the performance of the laser ion source with a radioactive ^{80}Ga beam. The radioactive Ga isotopes were selectively ionized by laser radiation and accelerated from the target/ion source to 30kV to the mass separator. Two Faraday cups, one after the mass separator and the other before the collection point on the tape of COeCO setup [43], were used to measure the current in order to track the number of ions.

We performed a laser on-off test on gammas from ^{80}Ga. The lasers result in a factor 8 enhancement on ^{80}Ga detection/production. This factor can be improved by adjusting the oven temperature or increasing the power of the ionization step. Figure 6.7 shows the γ spectrum measured with surface ionization (purple) compared to the γ spectrum with the laser ion source (pink) at mass 80.

From figure 6.7, we can instantly notice a significant improvement in the statistics and the purity/signal-to-noise ratio of the spectrum, obtained thanks to the laser ion source and the mass separator to avoid mass contamination. The overall laser ionization efficiency for Ga was about 0.01%.

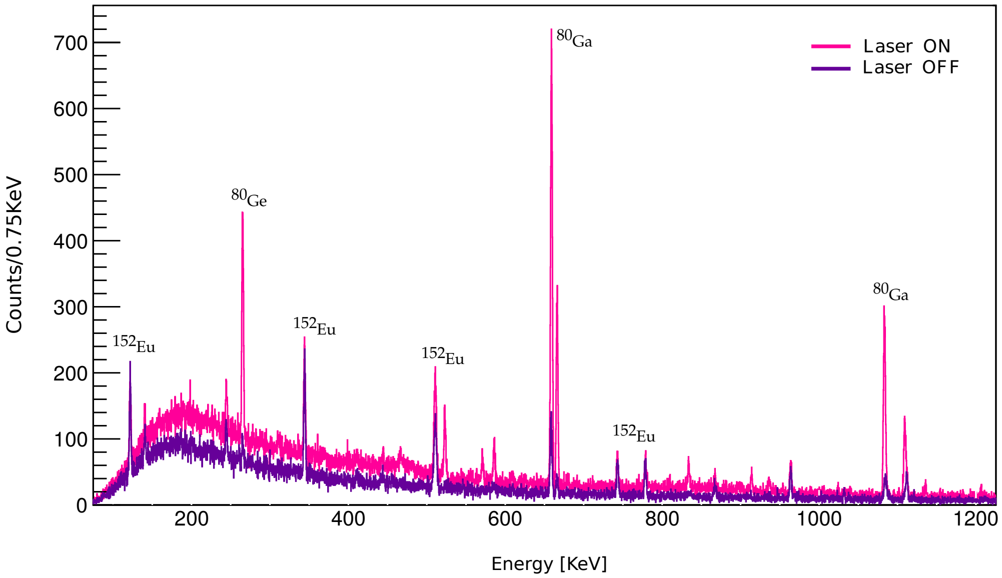

Figure 6.7: Laser ON-OFF effect. Gamma-ray spectrum recorded with HPGe detectors at the COeCO station for ^{80}Ga with surface ionization ion source (purple) and with the laser ionization (pink). We have an enhancement of a factor 8 with lasers.

6.2 Production of radioactive nuclei

Producing more exotic nuclei is necessary to explore the unknown regions of the nuclear chart, and accelerator technology has allowed the development of several methods for this purpose. The ISOL method is usually used to produce exotic nuclei by sending a primary beam in a thick target and adding an ionization source to ionize the atoms. The release time of fission fragments in nuclear fission processes is strongly influenced by the chemical properties of the fragments themselves and the characteristics of the target material. Notably, refractory elements with exceptionally high boiling temperatures exhibit limited release from the target due to their tendency to remain within it. However, a certain degree of chemical selectivity can be achieved by carefully choosing target materials or implementing specific ionization mechanisms. This selectivity enables to selective targeting and manipulation of desired elements while minimizing the release of others, allowing for focused investigations and controlled utilization of specific elements of interest.

The ISOL method combined with the fission mechanism is particularly suitable for studying neutron-rich nuclei in the intermediate mass region. The ALTO facility applies the ISOL technique uniquely by using photons produced from bremsstrahlung radiation to induce uranium fission. This approach results in higher purity of isotopes compared to other methods, as the energetic gamma rays penetrate the target material deeply and produce a more uniform isotope distribution. By focusing exclusively on fission reactions induced by photons, the unwanted isotopes arising from spallation/fragmentation reactions are minimized, leading to an overall increase in the purity of the final product.

Evaluating and reporting yields of isotopes is a critical aspect of nuclear experiments, yet it is often overlooked. The evaluation of yields provides essential information for better planning of experiments, improving target performance, and detecting issues with the experimental setup or beamline transmission. Furthermore, comparing yields with those from other facilities offers insights into the performance of different systems. However, estimating yields from indirect sources poses a significant challenge, and including technical details is necessary for scaling to improved machine parameters.

In the following sections of this chapter, we will describe the method used for production measurements and present the results obtained in 2022 after the upgrade of the front-end of the ALTO facility (FRISAL). These results will be presented for the case of Ga and compared with previous measurements at ALTO and the estimated production. They will be finally compared with the yields obtained by ISOLDE [78].

6.3 Production measurements

Fission production measurements are crucial in understanding the fission process and play an essential role in designing experiments. While mass yields have been measured for many fissioning systems at different excitation energies, isotopic yields are more challenging to obtain experimentally and are available for fewer cases [79]. Improving our knowledge of isotopic fission yields can enhance our understanding of the fission process and have practical applications. Fission is the most promising way to produce very neutron-rich medium-mass isotopes. However, the yields of these rare isotopes are low, making clear isotope identification possible only through good A and Z separation.

The intensity of a radioactive beam depends on several factors and can be calculated using the equation:

$$I = \Phi \cdot \sigma \cdot N \cdot \epsilon_{\mathrm{r}} \cdot \epsilon_{\mathrm{ion}} \cdot \epsilon_{\mathrm{tr}} \tag{6.1}$$

Here, Φ represents the intensity of the primary beam, σ is the effective cross-section of the desired isotope, N denotes the number of target atoms exposed to the primary beam, ϵ_{r} represents the release efficiency of elements from the target to the source, ϵ_{ion} corresponds to the ionization efficiency, and ϵ_{tr} represents the ion-transport efficiency through the beam transport line, including the mass separation. Decay losses are already accounted for within the individual steps' efficiencies, which depend on the specific isotope's lifetime. The production of exotic radioactive nuclei requires considerable effort and is inherently limited in intensity. The extracted nuclei are highly valuable and must be obtained with maximum efficiency. The product of the efficiencies at each step determines the overall efficiency, and losses in individual steps can accumulate, leading to significant total losses. While the equation appears simple, it is more complex due to the interdependence of the factors. Thus, optimizing one part may have a negative impact on the overall efficiency. Additionally, certain factors depend not only on the element or mass of the isotope but also on its lifetime and other nuclear and atomic properties. Ideally, the complete ISOL system should be optimized for each specific isotope. However, in practice, a compromise must be found between individual optimization and the system's universality. In applications involving radioactive ion beams, the high intensity of the desired isotope is meaningless if accompanied by a large amount of other radioactive isotopes. Therefore, the separation process must efficiently isolate the desired isotope while minimizing contamination from other isobars. Decay losses are particularly significant for short-lived isotopes. To minimize these losses, the separation process should be performed quickly compared to the half-life of the nuclides.

Radioactive elements are produced at a rate given by the equation:

$$\phi = N\sigma\Phi \tag{6.2}$$

where ϕ is the production rate, N_a is the number of target atoms interacting with the beam, σ is the reaction cross-section, and I is the flux of incident particles. After the nuclei are formed, they decay according to the exponential law of radioactive decay given by:

$$N(t) = N_0 \mathrm{e}^{-\lambda t} \tag{6.3}$$

where N_0 is the original number of nuclei present at time $t = 0$, λ is the decay constant that is inversely proportional to the nuclei half-life, $t_{1/2}$ is the half-life (the time necessary for half of the nuclei to decay), according to the following equation:

$$\lambda = \frac{1}{\tau} = \frac{ln2}{t_{1/2}} \tag{6.4}$$

6.4 Production formalism

Nuclei can be produced through two distinct processes, as illustrated in Fig. 6.8. Firstly, they can be generated directly (nuclei A), wherein a stable nuclei target is bombarded with a beam of particles, forming N_A nuclei through reactions. Alternatively, nuclei can be produced through disintegration (nuclei B). In this case, nuclei A decay at a rate determined by the decay constant λ_A, ultimately transforming into nuclei B.

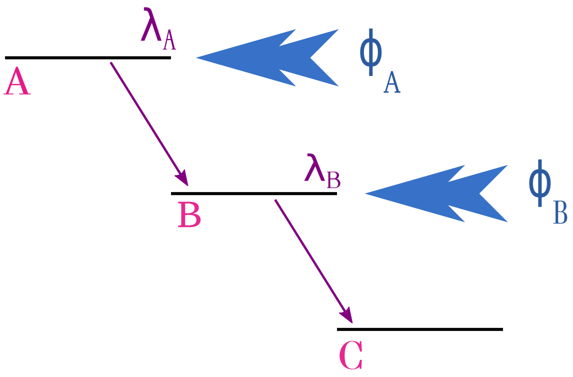

Figure 6.8: Production of radioactive species. This scheme illustrates an isobaric chain comprising three nuclei, with the beam feeding two.

In the case of direct production, the number of nuclei A is calculated as follows:

$$\frac{dN_{\mathrm{A}}(t)}{dt} = \phi_{\mathrm{A}} - \lambda_{\mathrm{A}} N_{\mathrm{A}}. \tag{6.5}$$

where ϕ_{A} is the number of nuclei A produced per second in the target, and λ_{A} is the decay constant of A.

Integration of this equation over the time of collection $(0,\ t_{\mathrm{coll}}\ )$ gives the result:

$$N_{\mathrm{A}}(t_{\mathrm{coll}}) = \frac{\phi_{\mathrm{A}}}{\lambda_{\mathrm{A}}}\left(1 - \mathrm{e}^{-\lambda_{\mathrm{A}} t_{\mathrm{coll}}}\right). \tag{6.6}$$

Since no new activity is formed after collection, the radioactive nuclei will decay according to the exponential law:

$$N_{\mathrm{A}}(t_{\mathrm{wait}}) = \frac{\phi_{\mathrm{A}}}{\lambda_{\mathrm{A}}}\left(1 - \mathrm{e}^{-\lambda_{\mathrm{A}} t_{\mathrm{coll}}}\right)\mathrm{e}^{-\lambda_{\mathrm{A}} t_{\mathrm{wait}}} \tag{6.7}$$

where t_{wait} is the time from the collection's end until the measurement's beginning. Finally, during the period of the measurement, the number of nuclei A present with respect to time t_{meas} is given by:

$$N_{\mathrm{A}}(t_{\mathrm{meas}}) = \frac{\phi_{\mathrm{A}}}{\lambda_{\mathrm{A}}}\left(1 - \mathrm{e}^{-\lambda_{\mathrm{A}} t_{\mathrm{coll}}}\right)\mathrm{e}^{-\lambda_{A} t_{\mathrm{wait}}}\mathrm{e}^{-\lambda_{\mathrm{A}} t_{\mathrm{meas}}} \tag{6.8}$$

We are interested in the number of decays of nuclei A during the whole measurement period (t_0, t_{end}) where t_0 is the end of the waiting time ($t_0 = t_{\text{wait}}$), t_{end} is the time at the end of the measurement. This can be found by integrating Eq. 6.8:

$$N_{\text{A}}(t_{\text{end}}) = \int_0^{t_{\text{end}}} \lambda_{\text{A}} N_{\text{A}}(t)dt \tag{6.9}$$

where $t_0 = 0$. Therefore, the total number of disintegrations for nuclei A is:

$$N_{\text{A}}(t_{\text{end}}) = \frac{\phi_{\text{A}}}{\lambda_{\text{A}}}\left(1 - \mathrm{e}^{-\lambda_{\text{A}} t_{\text{coll}}}\right)\mathrm{e}^{-\lambda_{\text{A}} t_{\text{wait}}}\left(1 - \mathrm{e}^{-\lambda_{\text{A}} t_{\text{end}}}\right) \tag{6.10}$$

In the second case, nuclei B are produced by the disintegration of nuclei A. Therefore, we must also consider the number of decay from the mother nuclei A. The general Bateman equation gives the evolution of the population of all elements issued from the decay.

$$\frac{dN_i(t)}{dt} = \phi_i + \lambda_{i-1}N_{i-1} - \lambda_i N_i(t) \tag{6.11}$$

Therefore, in the case where the second generation of nuclei is also radioactive and has a decay constant λ_{B}, the number of daughter nuclei N_{B} present increases as a result of the decays of the parent and decreases as a result of its own decay:

$$\frac{dN_{\text{B}}(t)}{dt} = \phi_{\text{A}} + \lambda_{\text{A}}N_{\text{A}} - \lambda_{\text{B}}N_{\text{B}} \tag{6.12}$$

By similarly solving this equation as done for the mother nuclei, we can obtain the solution for the number of decays of the daughter nucleus (B) throughout the entire measurement period, which is given by:

$$\begin{aligned} N_{\text{B}}(t_{\text{end}}) = &\frac{\phi_{\text{B}}}{\lambda_{\text{B}}}\left(1 - \mathrm{e}^{-\lambda_{\text{B}} t_{\text{coll}}}\right)\mathrm{e}^{-\lambda_{\text{B}} t_{\text{wait}}}\left(1 - \mathrm{e}^{-\lambda_{\text{B}} t_{\text{end}}}\right) \\ &+ \frac{\phi_{\text{A}}}{\lambda_{\text{A}}\lambda_{\text{B}}(\lambda_{\text{B}} - \lambda_{\text{A}})}\Big[\lambda_{\text{B}}^2\left(1 - \mathrm{e}^{-\lambda_{\text{A}} t_{\text{coll}}}\right)\mathrm{e}^{-\lambda_{\text{A}} t_{\text{wait}}}\left(1 - \mathrm{e}^{-\lambda_{\text{A}} t_{\text{end}}}\right) \\ &- \lambda_{\text{A}}^2\left(1 - \mathrm{e}^{-\lambda_{\text{B}} t_{\text{coll}}}\right)\mathrm{e}^{-\lambda_{\text{B}} t_{\text{wait}}}\left(1 - \mathrm{e}^{-\lambda_{\text{B}} t_{\text{end}}}\right)\Big] \end{aligned} \tag{6.13}$$

The details to obtain equation 6.13 are clearly explained in the thesis of B. Roussière [80].

This approach allows us to extend the analysis to third, fourth, and subsequent generations until we reach a stable nucleus or to a situation where the half-life of the n^{th} daughter is long enough to be negligible.

In the case of this work, we will only use equation 6.10 since we only had production of the mother nucleus with no subsequent generations.

6.5 Experimental set-up

In October 2022, production measurements were conducted to validate the commissioning of the FRISAL project [44]. The experiment aimed to reproduce the same conditions of the target ion source ensemble (TIS) used in 2019 to validate the short target. Contrary to 2019, where the measurements were made in the identification station, the measurements in 2022 were performed on the COeCO detection station located on the PARRNe line. Detailed information on this setup can be found in the thesis of G. Tocabens [43].

In 2019, production measurements were conducted in the identification station, which allowed for the characterization of β decays of elements in the beam using γ and electrons. The studied nuclei were collected on an aluminized mylar tape, and then the tape was moved to the detection region. The collection point was surrounded by a cylindrical plastic 4π scintillator connected to a photomultiplier to detect electrons from the decays. A large volume germanium detector was also placed close by (~ 3 cm from the tape) to detect the decay gamma rays. In the 2022 experiment, the identification station was replaced by COeCO, which has the same functionality as the identification station but eliminates the need to move the source to the detection system. This setup allows the nuclei to be collected and measured at the same place.

The COeCO setup allows the study of nuclei with shorter lifetimes as it performs the measurements at the point of collection of the beam - formerly the upper part of the station - and moves the tape only to evacuate the radioactive source and avoids long-lived species.

The identification station and the COeCO setup are shown in Fig. 6.9.

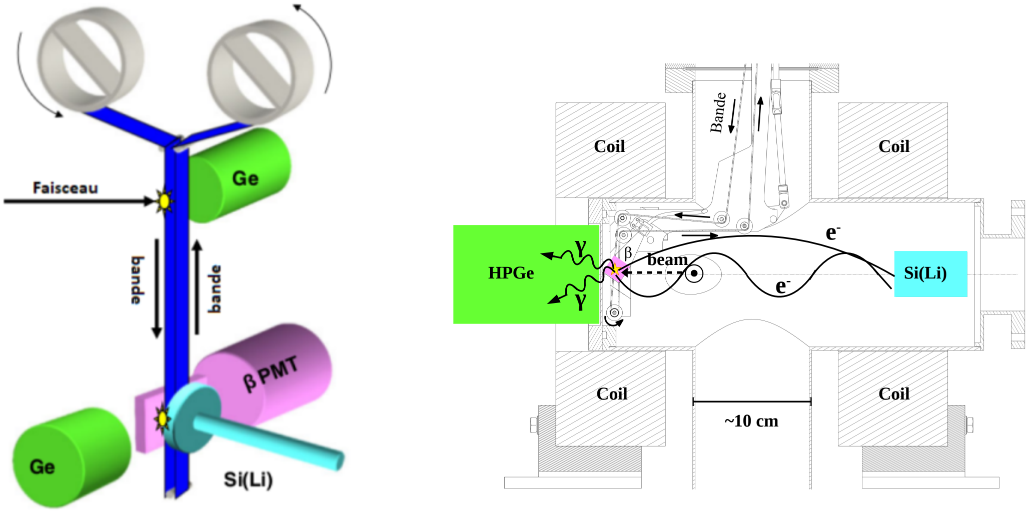

(a) Identification station

(b) COeCO

Figure 6.9: Identification station and COeCO comparison. In the identification station, the collection is made in the top part, and then the tape is moved to make the measurements in the lower part. In COeCO, the collection and detection are made at the same point (pink area).

Detection system

To carry out the COeCO experiment, an HPGe was used with a resolution of 2.9 keV for the 1408 keV line of the ^{152}Eu. However, due to strong cuts on low energies, gammas with energies below 121 keV were not used for determining production.

In order to confirm that the γ-lines observed in the spectrum originate from β-decay events, a β-gated energy spectrum needs to be constructed. The conditioned spectrum, also known as the spectrum γ conditioned on a β, refers to the collection of γ lines observed in coincidence with an electron resulting from a β-decay event. Its purpose is to identify the γ lines originating from the β-decay of a specific element within an isobaric chain. To construct this spectrum, we need to calibrate it in energy and ensure it coincides with an event in the β-detector.

Two spectra are created: a γ energy spectrum at the collection point and a spectrum of γ-rays coinciding with β events. These spectra are obtained through measurement cycles dedicated to a specific mass. On the conditioned spectrum, we identify the origin of each line to an isobar (Fig. 6.10).

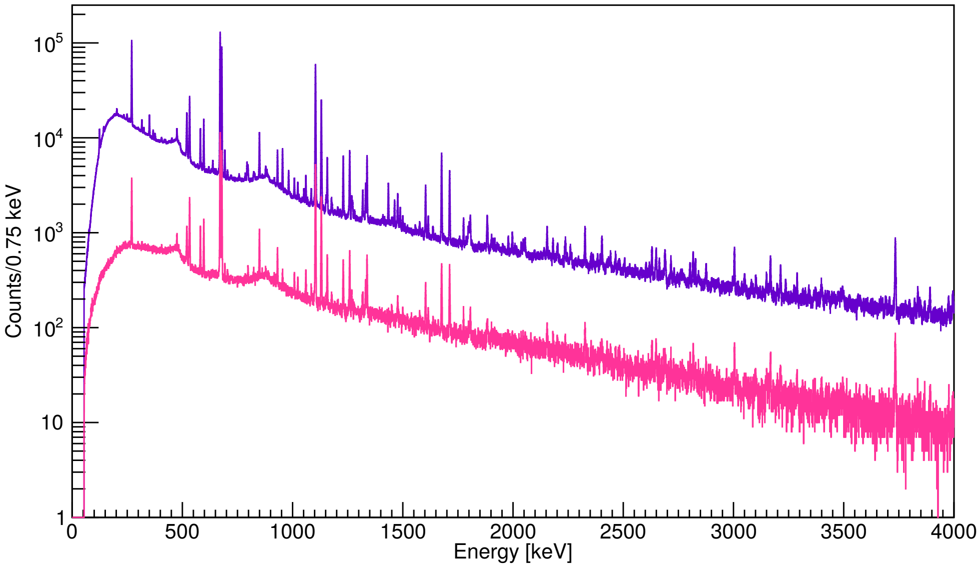

Figure 6.10: Energy spectrum of γ-rays detected by the HPGe detector. The spectrum without condition is shown in purple, and in pink, the coincidence condition is applied.

Using the conditioned spectrum, we identified the members of each line to an isobar, as only the γ resulting from a decay β appears in this spectrum. This method lets us remove pollutants collected outside the band during previous measurements. Then, on the unconditioned γ spectrum, we measure the intensity of the identified lines to evaluate the production of the corresponding nuclei.

For efficiency calibration, a ^{152}Eu source was placed at the collection point in the “near” configuration of the Ge detector. A copper-lined lead shield was added to the tip of the Ge detector to limit background noise.

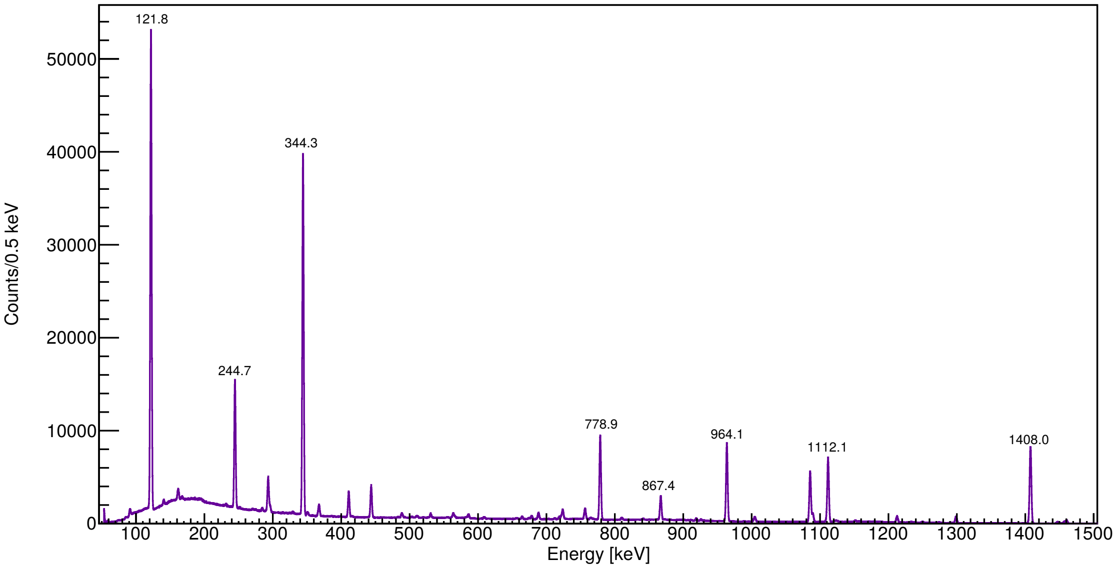

Figure 6.11: γ spectrum obtained with a ^{152}Eu source placed on the source holder near the collection point. The spectrum displays the peak values in keV, used for energy and efficiency calibration. Below 50 keV, a distinct and sharp cutoff is evident, notably influencing the low-energy background's shape.

Time cycle adjustment of the tape

The production rates of nuclei are characterized by measuring their β-decays for the set of masses produced. Each measured mass includes a group of isobars with known γ transitions. The intensity of these γ transitions can be measured to track the production rate of the corresponding isotope.

During typical production measurements, the mass-separated beam is collected on the mylar tape for a time t_{coll}, followed by a cut-off period t_{decay}, during which the nuclei are decaying. Finally, the measurement is stopped after a time $t_{\mathrm{end}} = t_{\mathrm{coll}} + t_{\mathrm{decay}}$. This beam collection and cut-off cycle constitutes a measurement cycle (see Fig. 6.12).

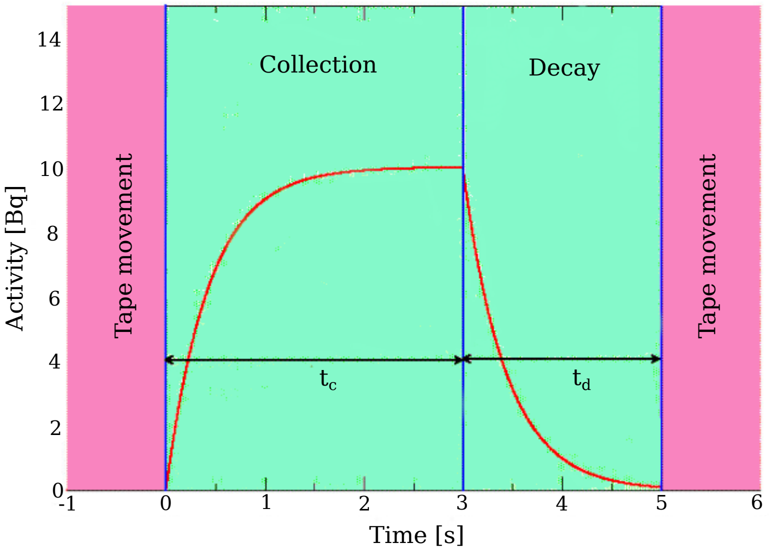

Figure 6.12: Diagram representing the evolution of the activity of the source collected on the tape as a function of time with the different acquisition phases. The acquisition is stopped in pink, and in green, the acquisition is allowed.

The choice of the two times, t_{coll} and t_{decay}, is based on the lifetime of the nucleus under investigation. The aim is to achieve an activity balance between beam feeding and radioactive decay before deflecting the beam. Specifically, t_{coll} is selected to be approximately 5 to 10 times the half-life ($\tau_{1/2}$) of the nucleus. This approach maximizes the ratio of beam activity to decay activity since the decay activity typically has a longer lifetime than the beam activity.

6.6 Analysis

During the experiment in October 2022, the data were recorded only during the collection time. Therefore, the incident flux is obtained by integrating, between $t = 0$ and t_{coll}, the activity ($A = \lambda N$) obtained with equation 6.6 and $t_{\text{wait}} = 0$. The production of the nuclei for measurement between $t = 0$ and t_{coll} obtained, is therefore given by:

$$\phi = \frac{N_d}{t_{\text{coll}} - \frac{1}{\lambda}(1 - e^{-\lambda t_{\text{coll}}})} \tag{6.14}$$

where t_{coll} is the collection time in a measurement cycle, and $\lambda = \frac{ln2}{t_{1/2}}$ is the decay constant of the nucleus. N_{d} is the number of disintegrations of the nucleus of interest during n_{cy} cycles of measurements and is given by:

$$N_{\text{d}} = \frac{\mathcal{A}}{n_{\text{cy}} \varepsilon I_{\gamma}(1 - DT)} - N_m \tag{6.15}$$

where $\mathcal{A}$ is the number of decay in function of the area of the γ peak, n_{cy} is the number of cycles chosen for the measurement, DT is the dead time of the channel of the germanium detector, ε is the efficiency of the gamma detection, I_{γ} is the absolute intensity of the gamma transition taken from literature and N_m is the number of decay induced by the feeding of the mother nuclei.

In our case, we do not consider the second-generation isotopes since the productions were only performed on the mother elements and not on their descendants. Thus, to determine ϕ, we use Equation 6.14 and Equation 6.15 with $Nm = 0$.

6.6.1 Number of cycle (n_{cy})

The determination of a particular cycle was required for studying each isobaric chain. The influence of the half-lives of each isobaric chain helped to choose the optimum cycle to maximize its activity during the measurement. All simulations conducted to determine the cycles and the expected productions were determined by B. Roussière [81] with the help of the FLUKA code (for the number of fission products present in the target), taking into account the ionization efficiencies of the elements and their release time. As the measurements were performed at the collection point, the measurement time indicated in column 3 of table 6.3 included the collection time (counting occurred during the collection).

A	$T_{1/2}$ [s]	T_{col}	T_{mes}	n_{cy}	e beam (µA)
76	32.6	100	100	6	8
78	5.09	100	100	6	8.5
79	2.85	30	30	20	8
80	1.9	30	30	20	8.3
81	1.22	30	30	20	8.2
82	0.6	30	30	20	8
83	0.3	30	30	20	8.3
84	0.085	600	600	1	8
85	0.092	600	600	1	8

Table 6.3: Tape station conditions for Ga production measurements.

In the Fluka calculations, a UCx target with dimensions of 13 mm diameter, 6 cm length, and a density of 3.82 g/cm^3 was used, with an incident electron energy of 50 MeV and a total of 6×10^8 electrons. The independent and cumulative production rates were normalized to a 10 µA electron beam. The latest version of Fluka has corrected the photofission cross sections [82]. However, there is still an underestimation (approximately a factor of 1.9) of the photon flux and the calculated number of fissions in the target. Since Fluka provides results based on A and Z without specifying the state (ground state or isomeric state) formed, we assumed that only the ground state is produced or that different isomers are formed in equal proportions. The productions at the target exit were estimated based on the expected values in the target, considering release and ionization efficiencies. The release times and main release mechanisms were determined in previous work [83, 34]. Ionization efficiencies were calculated for a Ta source at 2000 °C [81]. To determine the optimal measurement conditions, we have calculated gamma spectra that should be observed for various collection and counting time values.

Detection efficiency (ε)

The efficiency ε of the detector at a given energy E_γ is determined using the following equation:

$$\varepsilon(E_\gamma) = \frac{N(E_\gamma)}{A(t_{\text{measure}}) \cdot T_{\text{measure}} \cdot I_\gamma} \tag{6.16}$$

where N(E_γ) represents the area of the photopeak at energy E_γ above the background, $A(t_{\text{measure}})$ denotes the activity of the source at the time of the measurement, T_{measure} refers to the time of measurement, and I_γ represents the absolute branching ratio of the transition under consideration.

To extrapolate the data, a linear regression is applied between $\ln \varepsilon(E_\gamma)$ and $\ln E_\gamma$, resulting in the equation:

$$\ln \varepsilon(E_\gamma) = \alpha \ln E_\gamma + \beta \tag{6.17}$$

The corresponding α and β values for both energy ranges are shown in table 6.4.

	$\geq$ 244 keV	< 244 keV
α	−0.9297	0.2443
β	1.6505	−4.8478

Table 6.4: Coefficients of the extrapolation line of the efficiency.

The detector's efficiency for production measurements is shown in Fig. 6.13. We can see from the curve that the efficiency differs from the expected power-law form typically observed in similar scenarios. This deviation can be attributed to the high threshold setting of the constant fraction discriminator employed in the detection system. Applying this threshold reduces the detector's sensitivity to low-energy events in the spectrum, particularly for energies up to 244.7 keV, corresponding to the second peak of the ^{152}Eu calibration source, as shown in Fig. 6.11. Furthermore, an undesired noise source caused saturation in the COMET acquisition channel, resulting in a loss due to the dead time of approximately 20%.

To address this issue, a decision was made to eliminate the noise, even though it carries the potential risk of disregarding low-energy γ events.

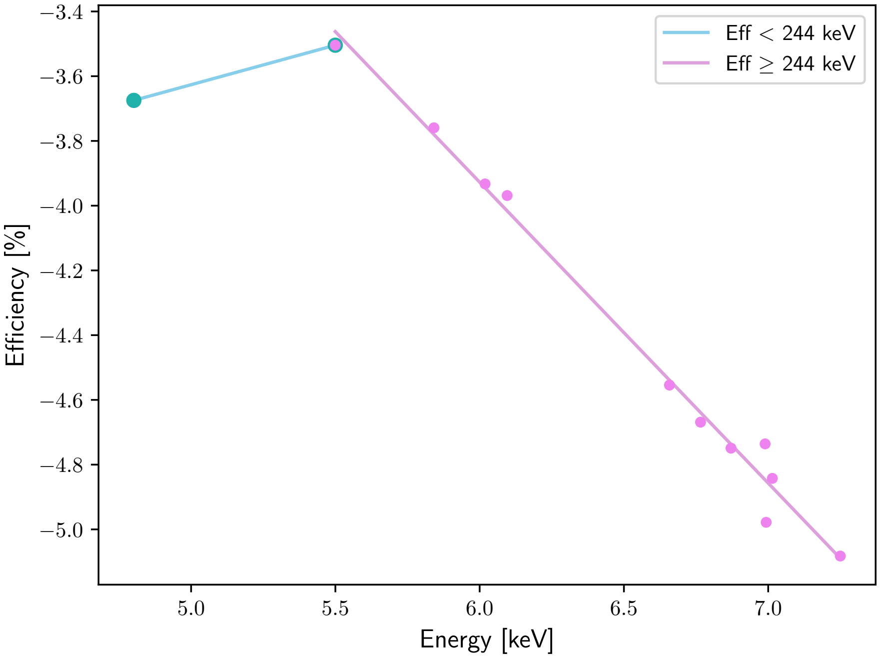

Figure 6.13: HPGe efficiency calibration curve. In blue, we have the efficiency below 244 keV, and in pink, the efficiency above 244 keV. The points are measurements, and the lines are the extrapolation.

Dead Time (DT)

The detector needs a minimum amount of time to process the events. Events that occur during the dead period are lost. To determine the dead time, we used the following expression:

$$DT = \frac{\text{True count rate - Measured count rate}}{\text{True count rate}} \tag{6.18}$$

In order to evaluate the dead time during the production measurements, we used a pulse generator operating at a frequency of $f_{\text{gen}} = 10$ Hz as shown in Fig. 6.14. The equation 6.18 can be written :

$$DT = \frac{T_{\text{meas}} \times n_{\text{cy}} \times f_{\text{gen}} - A_{\text{gen}}}{T_{\text{meas}} \times n_{\text{cy}} \times f_{\text{gen}}} \tag{6.19}$$

where T_{meas} is the time of measurements, n_{cy} the number of cycle, f_{gen} the frequency of the generator, and A_{gen} the area of the generator events recorded (Fig. 6.14).

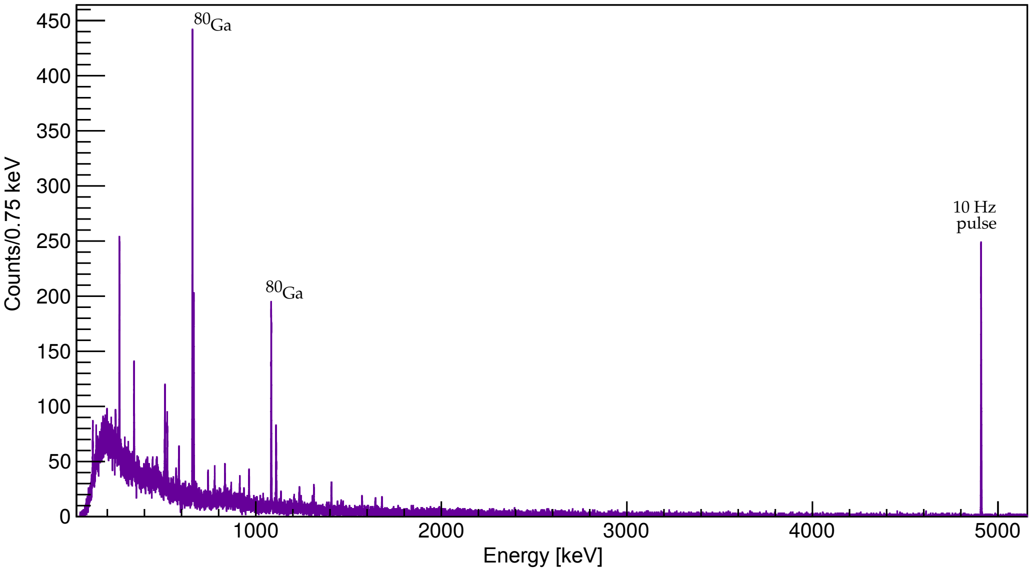

Figure 6.14: Gamma spectrum of ^{80}Ga. We can see the peak generated by the pulse of 10 Hz. We use the peak area to determine the dead time.

6.6.2 Gallium production

The beam of Ga ions used in the experiment was produced using the resonance ionization laser ion source at ALTO. Initially, radioactive species were generated by subjecting a high-temperature UCx target to photofission. These species were then transported as vapor to a closely coupled ion source and extracted as positive ions at an energy of 30 keV. To ensure the desired isobaric separation, the PARRNe mass separator dipole magnet was utilized to selectively choose ions within the mass range from 76 to 85.

The COeCO setup collection point (Fig. 5.8) was used for the production measurements. This line offers better accessibility for adjusting the ion optics elements than other lines. Additionally, previous production measurements have consistently been carried out on this line, facilitating easier comparisons.

Morover, in order to ensure that the production measurements obtained from the COeCO detection station during the 2022 experiment were comparable to those obtained in 2019, efforts were made to place the ensemble target ion source (TIS) under similar conditions. Specifically, a short target type PARRNe was used, and the oven power was set to approximately 3050 W while keeping the cathode at around 600 W. An extraction electrode with a voltage of 30 kV was also used. These parameters were chosen to replicate the conditions of the previous experiment and enable an accurate comparison of the production measurements obtained and are shown in table 6.5.

Year	Target	Oven			Cathode		
		I(A)	U (V)	P(W)	I(A)	U (V)	P(W)
2015	Long CNT-CERN 20 cm	810	4	3240	380	2.2	820
2019	Short (PARRNe) 6 cm	780	3.9	3047	320	1.9	600
2022	Short (PARRNe) 6 cm	985	3.2	3090	459	1.4	648

Table 6.5: Target ion source heating conditions.

6.7 Results

The intensities of $^{76-85}$Ga production (ϕ_n) obtained in this work are displayed in Table 6.6. These values have been normalized with respect to a 10 µA electron beam to enable direct comparisons with the production reported in the 2019 [84], 2015 [85], and the expected calculations [81].

Ga	ϕ_n Laser ionization	ϕ_{2022} Surface ionization	ϕ_{expected} Surface ionization	ϕ_{2019} Laser ionization	ϕ_{2015} Surface ionization
76	$1.53{\times}10^4$	-	9.8×10^2	-	-
78	$2.70{\times}10^4$	-	2.24×10^3	-	-
79	$3.93{\times}10^4$	-	2.73×10^3	-	-
80	$2.80{\times}10^4$	$3.49{\times}10^3$	2.5×10^3	$3{\times}10^4$	$1{\times}10^4$
81	$1.26{\times}10^4$	-	2.39×10^3	-	-
82	$1.19{\times}10^3$	-	7.43×10^2	-	-
83	$1.50{\times}10^2$	-	3.53×10^2	-	10
84	-	-	39	-	-
85	-	-	23.2	-	-

Table 6.6: Ga yields. The value of the beam intensities for each mass measured in previous experiments [84, 85], as well as the values obtained from the current experiment and calculated values for surface ionization [81].

Figure 6.15 shows the Ga production measurements obtained in previous experimental studies, as well as the expected yields and the intensities achieved within the scope of this work.

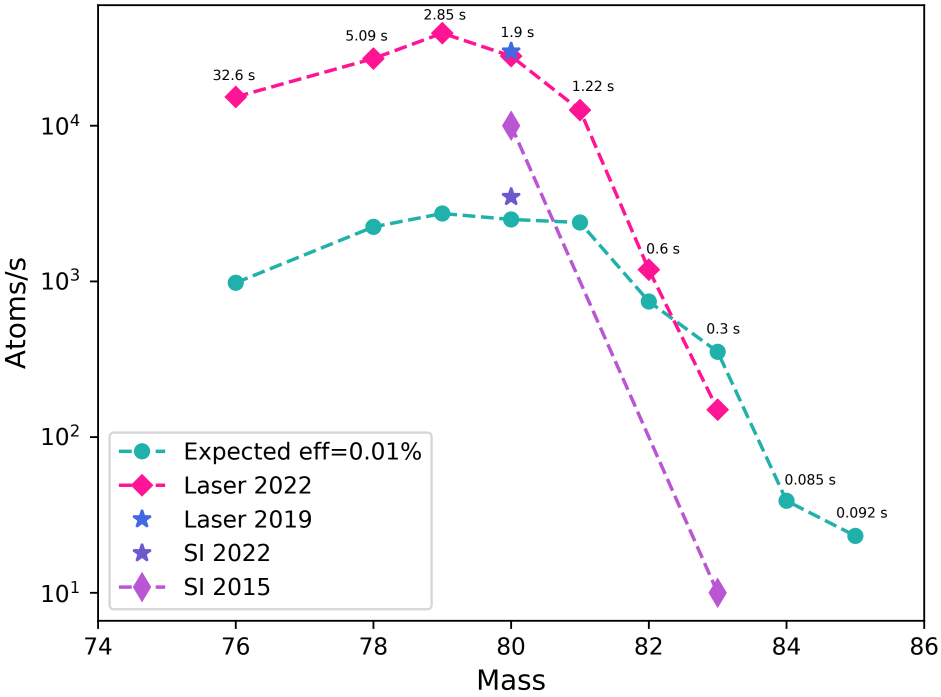

Figure 6.15: Gallium production.

Gallium, being predominantly effusion-governed, poses challenges for ionization through surface ionization. In 2019, Li et al. [84] studied the decay of ^{80}Ga and reported data that allowed the estimation of the production of ^{80}Ga ionized by laser at 3×10^4 pps.

The values are identical in comparing the ^{80}Ga production obtained by laser ionization in 2019 and 2022. After correcting by a factor of 8, due to the difference in ionization efficiency between the laser source and the surface ionization source that we determined, the obtained production of ^{80}Ga is in agreement with the expected production for an ionization efficiency of 0.01%. The production value of ^{80}Ga obtained in 2015 by Gottardo et al. [85] is higher because the target had been heated to 3240 W and the cathode to 820 W. The low production value of ^{83}Ga that they obtained can be explained by using a long CNT target which increases the path of particles, and a uranium density lower by a factor of 3 which reduces the number of fissions produced.

From Fig. 6.15, we can see a different behavior than the expected one starting in mass 81. The production values of ^{81}Ga, ^{82}Ga, and ^{83}Ga that we obtain, falls sharply and ^{83}Ga is below the expected value even when comparing yields for surface ionization. We think that this effect can be explained by several parameters.

The release time of Gallium from the target is approximately 2 seconds, and for isotopes beyond mass 81, their half-lives are less than 1 second. This explains the significant decrease in production observed beyond A=81. It is evident that the power of 3090 W applied to the TIS is insufficient, and increasing it to at least 3240 W could potentially maximize the release of Gallium. If the release of these isotopes from the target is slow, their yield will decline faster than the production cross-section predicted. This is because the isotopes will undergo decay while still within the target rather than being fully released. It is worth noting that a mass shift may have occurred within the PARRNe separator during the measurements, further influencing the observed results.

The productions of Ga isotopes demonstrate the success of commissioning the new FRISAL Front-End. The productions measured for gallium isotopes show reproducibility with the 2019 experiment performed under similar target-source conditions. This reproducibility rules out parameters related to linac (I_{P}), target (N and ϵ_{r}), and TIS (ϵ_{r} and ϵ_{ion}).

6.8 Comparison with ISOLDE productions

The Ga production results obtained at ALTO are compared with the one obtained at ISOLDE [78] as shown in Table 6.7.

Ga	ϕ_n ALTO 2022	ϕ_n ISOLDE
76	1.53×10^4	7×10^5
78	2.70×10^4	7.5×10^5
79	3.93×10^4	6.5×10^5
80	2.80×10^4	3.1×10^5
81	1.26×10^4	1.9×10^5
82	1.19×10^3	3×10^4
83	1.50×10^2	4.5×10^3

Table 6.7: Ga yields comparison between ALTO production in 2022 and ISOLDE [78].

A notable observation is that the Ga production at ISOLDE is approximately 10 times higher compared to ALTO. Two factors can account for this significant difference. Firstly, the choice of ionization tube material plays a crucial role. At ALTO, the ionization tube is composed of Tantalum, while at ISOLDE, it is made of Tungsten, demonstrating a higher efficiency of approximately a factor of 10 [77]. Secondly, the total thickness of the UCx target at ISOLDE is twice that of ALTO, which contributes to the increased production yield.

Despite these variations, it is noteworthy that the ratio of laser on to laser off effect (Laser ionization/Surface ionization) remains the same at both facilities [78], even though with RILIS at ISOLDE, they add up a second resonant step (from a metastable state) in the scheme of Ga ionization.

However, photofission offers a notable advantage in terms of beam purity. Comparing the yields of ALTO and ISOLDE using 500W of photofission alone, the difference is only a factor of 10, which is actually quite remarkable. It's worth noting that to achieve a similar level of beam purity, ISOLDE requires the use of the n converter, resulting in a yield loss of approximately a factor of 10.

Chapter 7

Conclusions and perspectives

7.1 Conclusions

RIALTO upgrade

This work addressed a number of optimizations, refinements, and developments that improved the performance of the RIALTO system and the radioactive ion beam production.

The laser system of the ALTO laser ion source was upgraded with a second Nd:YAG, a new beam distribution system, and a pointing stabilization system for two beams, one UV and one Nd:YAG. Implementing an Edgewave electro-optical Q-switched diode-pumped Nd:YAG laser for non-resonant ionization has improved the quality of the non-resonant step, resulting in increased ionization efficiency and reduced background noise.

Moreover, including two beam-pointing stabilization systems in the setup has enhanced the beam stability of RIALTO, minimizing the effects of environmental fluctuations and ensuring consistent and stable ion beam production.

The changes made to the beam distribution system, including the use of half-wave plates ($\lambda/2$) and polarized beam-splitter cubes, have enabled more precise control over the direction and polarization of the laser beams, leading to improved beam quality and higher ionization efficiency.

Notably, the ability to study multiple elements simultaneously has been achieved due to this improvements, enabling having two different element schemes in optimal conditions for online operation. Usually, up to one week of preparation is needed if a different element is requested (if the scheme is known and has been tested prior); this includes a change of the dye solution, laser setup, and alignment of the beams into the ion source.

Switching between Ag and Ga was successfully demonstrated within a remarkably short time of less than an hour. This achievement holds significant importance as it introduces the possibility for the simultaneous use of separate laser beams by two users in the same target without any time loss. Moreover, this breakthrough enables the implementation of a streamlined approach, wherein one laser scheme can be dedicated to experimental measurements while another laser beam remains available for scheme development or yield measurements. Previously, switching schemes was risky due to misalignment hazards, restricting beam diagnostic to Rb. However, recent improvements facilitate safe verification using Ga without compromising the experimental setup.

Ga production

The successful commissioning of the new FRISAL Front-End and the technical upgrade of RIALTO are validated by the Ga production achievements across different isotopes. Notably, the productions measured on gallium isotopes show reproducibility with the 2019 experiment under similar target-source conditions.

To further enhance Ga production, several factors should be considered. Firstly, the applied power of 3090 W to the TIS is insufficient; the power of 3240 W, as used during production in 2019, has the potential to maximize Ga release and improve production efficiency.

Some difficulties were also encountered in effectively driving the separated beam to the COeCO tape station. Addressing this issue would require a better understanding of the source's emittance and the incorporation of diagnostics to transport the beam effectively.

Moreover, replacing the Tantalum ionization tube with a Tungsten one can enhance production. Tungsten has demonstrated approximately 10 times higher efficiency, offering an opportunity to improve Ga production yields [77].

Silver production

This work implemented a three-step resonant photoionization scheme for Ag and will be used for the on-line production of neutron-rich radioactive Ag ions in the ALTO facility. It is noteworthy that silver was successfully ionized for the first time in ALTO using this scheme.

The production of silver was carried out both off-line and on-line. Although no test with radioactive silver could be performed, the on-line measurements effectively replicated the power saturation measurements and the laser on-off effect, thereby instilling confidence in the feasibility of this approach for future on-line experiments. Furthermore, the production of stable silver was achieved without encountering any difficulties during two separate beam times. However, a test using a quantified silver sample is required to evaluate the efficiency of the laser ion source using this specific level scheme.

7.2 Perspectives

7.2.1 Neutron rich radioactive silver program

The astrophysical rapid neutron capture process (r-process) is believed to produce half of the neutron-rich stable or long-lived nuclides heavier than iron. These nuclides have been observed not only in stars of various metallicities but also in the solar system [86]. Despite this, the exact path of the r-process remains unclear, and accurate nucleosynthesis modeling requires precise nuclear data across a wide range of fundamental properties. Masses, lifetimes, decay and neutron capture rates, and β-delayed neutron emission probabilities are essential to these models.

Obtaining a complete set of fundamental nuclear properties, including masses, is crucial to understand stellar nucleosynthesis. The observed solar r-process elemental abundance distribution peaks at A=130 and is connected to the shell closure at N=82. Thus, the N=82 isotones below ^{132}Sn are crucial in modeling stellar nucleosynthesis. This region also covers predicted waiting-point nuclei, where neutron capture rates and photodisintegration processes are in equilibrium, and meaningful calculations for these scenarios require accurate fundamental nuclear properties.

To this end, an experiment for the high-precision mass measurement of silver isotopes (A=113-129) towards the N=82 shell closure with MLLTRAP at ALTO is planned. The experiment aims to explore the possible weakening of the shell gap for $Z < 50$ and its impact on A=130 r-process nucleosynthesis. The study will focus on measuring neutron-rich silver isotopes (Z=47, $A > 121$). The ground-state light silver masses ($A < 121$), which are known with a precision below 20 keV, will be used for the online commissioning of MLLTRAP and to characterize the performance of the detection system. By conducting this experiment, we aim to better understand fundamental nuclear properties and their role in stellar nucleosynthesis.

The neutron emission probability following β decay, known as P_n, is an essential parameter in nuclear science. This probability plays a significant role in understanding various nuclear processes, including the r-process of nucleosynthesis, reactor power control, and nuclear waste management. P_n values also provide valuable information about the nuclear structure and help identify systematics along isotopic or isotonic chains [87].

This study aims to measure the β-delayed neutron emission probability of neutron-rich silver isotopes with Z=47. The investigation will cover the isotopes ranging from the first known neutron emitter, ^{122}Ag (N=75), to the magic isotope ^{129}Ag (N=82). To verify the feasibility of the measurement, a production yield measurement of ^{130}Ag will also be performed.

To carry out this experiment, the study will take advantage of the unique possibilities offered by the TETRA [42] facility and the intense neutron-rich radioactive beams provided by ALTO. The data obtained will be compared to empirical formulae and the most advanced r-process modelization values, expecting to contribute to a better understanding of nuclear structure and properties.

Combining the RILIS technique with decay detection shows great promise for future experiments on exotic beams. An important asset for these experiments is a versatile decay station, which can be used to separate isomeric and ground state structures and improve background suppression. These areas can now be explored with the help of the work developed during this thesis.

The availability of a high-profile beam at ALTO holds significant scientific implications, as silver has gained importance as a subject of study in numerous ISOL facilities worldwide. ALTO can now enter the competitive field and contribute to the advancements in neutron-rich silver research. This beam provides a unique opportunity to perform precise mass measurements and decay spectroscopy experiments, enabling a deeper understanding of nuclear properties.

7.2.2 The future of RIALTO

New Nd:YAG laser

RIALTO has recently ordered a third Nd:YAG laser with green/UV output that will be installed soon. This acquisition will allow us to expand the wavelength range using a UV pump laser to access the blue range and access the Third Harmonic Generation (THG) through the already available frequency triple conversion unit. This unit was jointly developed by

Johannes Gutenberg-Universität Mainz in Germany and CERN [88]. The fundamental laser radiation is introduced from the right; then, its frequency is doubled with a BBO crystal. The resulting doubled frequency laser beam and the remaining IR laser are then divided into two paths by a dichroic mirror. They are subsequently recombined to generate tripled-frequency light in another BBO crystal (Fig. 7.1).

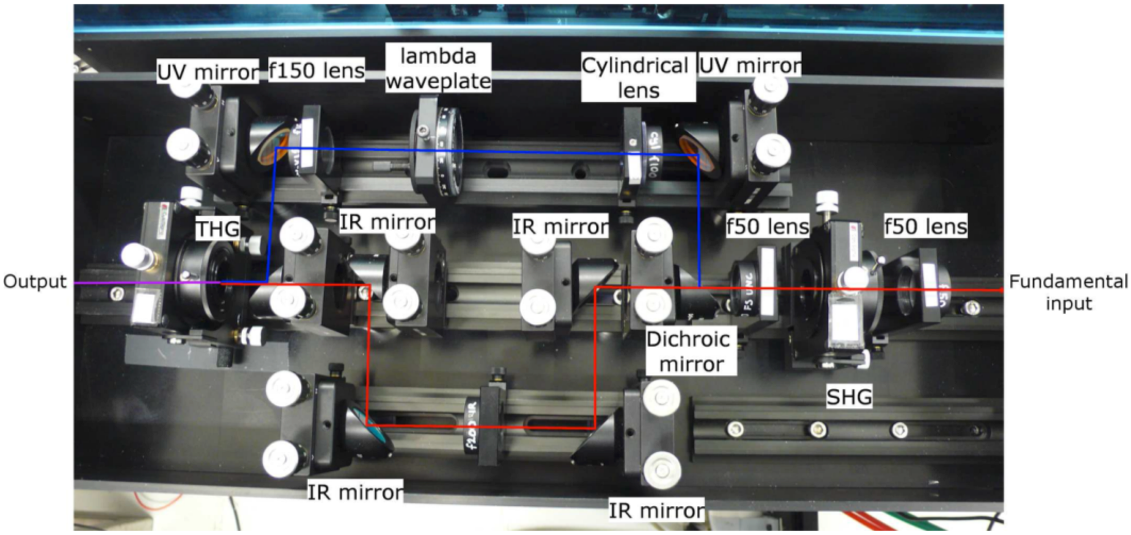

Figure 7.1: Third Harmonic Generator (THG) unit.

Combining this new pump laser and the frequency triple conversion unit will extend RIALTO's wavelength range and give us access to ionization schemes where the first steps require THG, notably Zn ($\lambda = 213.9\,\text{nm}$), and Sb ($\lambda = 217.6\,\text{nm}$). The UV pumping will also allow the production of the $\lambda = 530\,\text{nm}$ needed to develop a Ge beam.

Furthermore, during silver production, it was noted that non-resonant transitions were not saturated, which could be improved by increasing the available power. This new laser will help us address this issue by providing additional power for non-resonant transitions. In addition to these benefits, the new laser will serve as a backup pump laser with the same operating parameters as the non-resonant laser, minimizing downtime in the event of malfunction or urgent maintenance. This is a crucial consideration given the complexity of the experiments conducted at ALTO.

Ionization scheme research for Ag

RIALTO has demonstrated significant progress in producing radioactive ion beams and developing new element schemes in the Atomic Beam Unit (ABU) process, resulting in improved production efficiency.

In addition to its current use in ionization scheme development, the ABU can also be utilized for spectroscopy measurements and exploring AI states.

To develop a new ionization scheme, we need to conduct a comprehensive search involving database and bibliographical research and experimental tests of a wide range of possibilities. To create an effective ionization scheme, we need to ensure that the atomic transitions are strong enough to result in the highest population of excited levels, that the transition scheme follows the selection rules of quantum mechanics, and that the frequency of the transitions can be achieved using the radiation of the dye laser, including high harmonics.

Thanks to the improved layout of RIALTO, we can now leverage the ABU to develop novel-level schemes. By using the current dye in the Lioptec laser, Rhodamine 6G with ethanol, we have access to a wavelength range of approximately ~ 552 – 600 nm fundamental and ~ 276 – 300 SHG. One of our primary goals is to identify new ionization schemes that could be more efficient or locate silver autoionizing states. We plan to explore a range of different scenarios in order to test our hypotheses, which are detailed in Figure 7.2.

We have identified three different scenarios to investigate:

1. In the first case, we plan to use the fundamental wavelength of Ga instead of Nd:YAG in the existing scheme, with the goal of identifying AI states with a different parity than the ground state.

2. The second scenario will involve a two-step scheme, with the SHG of Ga as the second step. We will be looking for AI states with the same parity as the ground state.
3. In the third case, we will use the fundamental of Ga as the second step in our process.
4. Change dye to styryl 9M and scan around 810 nm (transition needed to reach IP).

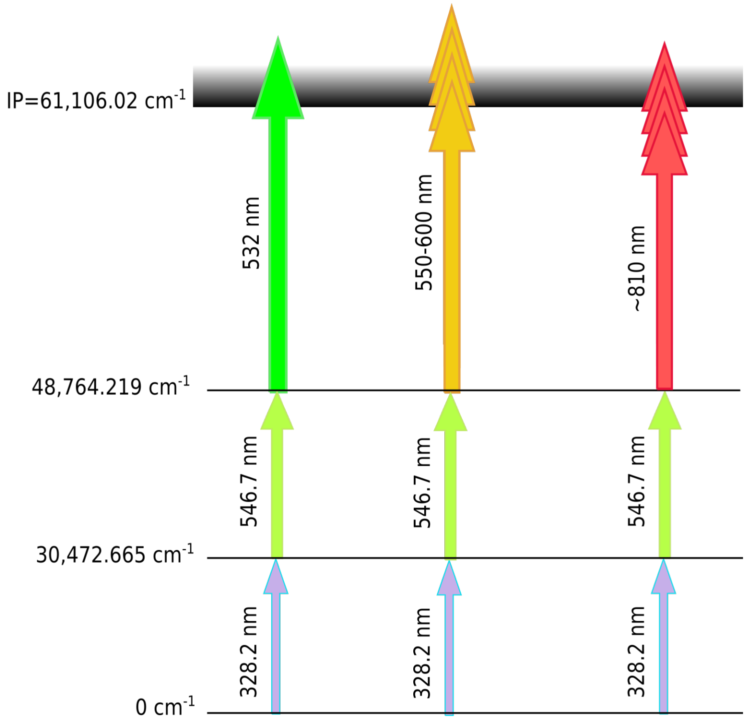

Figure 7.2: Ag new ionization schemes. Possible ionization scheme to test with the current RIALTO laser system. The orange beam represents the fundamental wavelength of Ga, and the cyan beam is the second harmonic.

The use of UV light to search for autoionizing states presents a significant challenge due to the propensity of even low-power outputs to produce contaminants, such as Cs. For this, an alternative approach involves exploring the possibility of changing the dye of the Lioptec laser to investigate the wavelength range in the vicinity of 810 nm.

Future element ionization schemes

With the RIALTO laser system upgrade, we aim to explore the feasibility of developing new beams for ALTO. We have considered as candidates the following elements: Zn (3-steps-3 color ionization scheme), Cu (2-steps-2 color ionization scheme), Sb (3-steps-3 color ionization scheme), Sn (3-steps-3 color ionization scheme), and Ge (3-steps-3 color ionization scheme). The ionization schemes are shown in Fig. 7.3

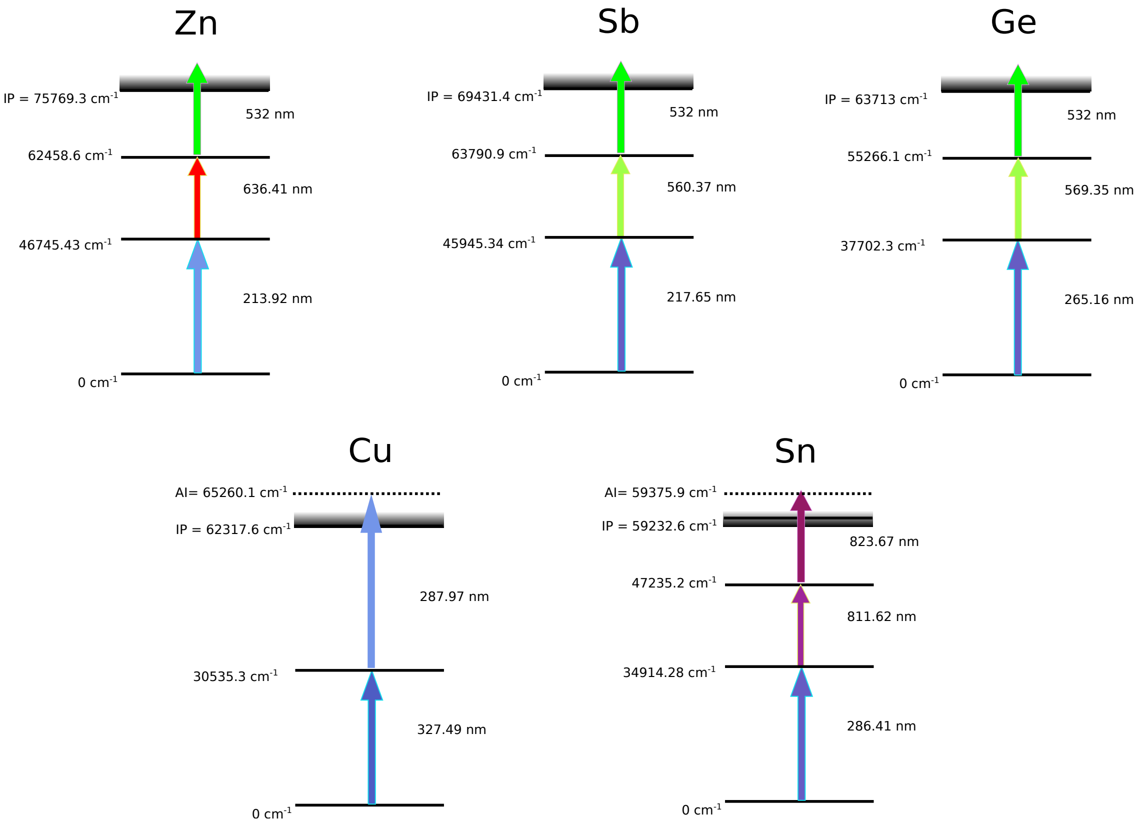

Figure 7.3: Future element schemes to develop with RIALTO. Zn, Sb, and Ge will use a 3-steps-3 color ionization scheme with a non-resonant last step, for Cu, a 2-steps-2 color scheme) and for Sn, a 3-steps-3 color resonant scheme.

Résumé en Français

Introduction

L'étude des noyaux exotiques (caractérisés par des rapports déséquilibrés entre les protons et les neutrons, loin de la stabilité β) permet de comprendre le comportement de la matière hadronique dans des conditions extrêmes. Les faisceaux d'ions radioactifs (RIB) offrent une opportunité unique pour étudier ces noyaux et sont essentiels dans de nombreux domaines de la physique nucléaire. .

Cependant, leurs productions est complexe en raison des faibles sections efficaces et des productions bien inférieurs aux isotopes stables. Il est donc essentiel de séparer efficacement les noyaux exotiques des noyaux stables

Pour produire des RIB,différentes méthodes et réactions nucléaires sont utilisées, telles que la fission, la spallation, la fragmentation (côté cible et côté projectile), l'évaporation de fusion et les collisions profondément inélastiques. Deux approches complémentaires ont été développées pour obtenir des faisceaux radioactifs intenses et énergétiques : la méthode In-Flight [22] et la technique de séparation isotopique en ligne (ISOL, de son acronyme anglais). La méthode In-Flight consiste à bombarder une cible fine avec un faisceau lourd de haute intensité, tandis que la technique ISOL que consiste à bombarder une cible épaisse par un faisceau léger.

La méthode ISOL

La méthode ISOL est utilisée pour produire et sélectionner un grand nombre de noyaux exotiques avec une grande pureté, afin de les étudier dans des expériences [28]. Elle implique le bombardement d'une cible épaisse avec un faisceau de lumière intense ou de partcules legères, ce qui génère des réactions nucléaires et des atomes radioactifs. Ces atomes sont extraits de la cible, ionisés et accélérés pour former un faisceau de quelques dizaines de keV, qui est ensuite séparé en fonction de la masse. Cette méthode nécessite des sources d'ions efficaces, sélectives et stables pour minimiser les contaminations et les pertes.

La méthode d'ionisation dépend fortement des propriétés chimiques de chaque élément, telles que sa volatilité et, surtout, son potentiel d'ionisation (IP).

En gros, les sources d'ions de surface sont efficaces pour ioniser les éléments du premier groupe du tableau périodique, tandis que la source de plasma est utilisée pour les derniers groupes et les métaux de transition. Cependant, les sources de plasma ont l'inconvénient d'être indiscriminées, ce qui compromet la pureté du faisceau d'ions. La source d'ions par ionisation résonante laser (RILIS, de son acronyme anglais) peut être utilisée pour surmonter cette limitation.

ALTO

ALTO (Accélérateur Linéaire et Tandem d'Orsay) est un ensemble de deux accélérateurs situé à l'IJCLab sur le campus d'Orsay de l'Université Paris-Saclay, en France. Il comprend un accélérateur Van de Graff pour les faisceaux stables et un accélérateur linéaire d'électrons (LINAC [32]) utilisé pour produire des faisceaux d'ions radioactifs riches en neutrons à l'aide de la technique ISOL.

À ALTO, les atomes radioactifs sont produits par photo-fission en utilisant un faisceau d'électrons accéléré à 50 MeV avec une intensité de 10 µA [21]. Ce faisceau bombarde une cible d'UCx pour induire la photo-fission par rayonnement de Bremsstrahlung [33]. La cible est placée dans un four et chauffée à des températures ($> 2000\,°C$) pour favoriser la diffusion et l'extraction des atomes radioactifs [34].

Les atomes sont ensuite ionisés par différentes techniques en fonction des besoins (ionisation de surface, laser, plasma). À la sortie de la source d'ions, une différence de potentiel de 30 kV extrait les atomes ionisées pour les envoyer vers le spectromètre magnétique PARRNe avec une résolution de R=$\frac{A}{\Delta A}$=1500. Une fois sélectionnés, les ions sont guidés par un ensemble de déflecteurs et de lentilles électrostatiques vers les plates-formes expérimentales.

Pour mener des expériences dans ces installations, il est nécessaire d'utiliser des faisceaux isotopiques purs. Cependant, les fragments de fission induits par des électrons à ALTO peuvent encore entraîner une contamination isobare significative, car une ionisation thermique non désirée des atomes peut se produire à la surface chaude. Afin de résoudre ce problème et maximiser la sélection en Z, une source d'ions par ionisation résonante au laser (RILIS) est disponible à ALTO.

RILIS

La méthode de RILIS (Ionisation Résonante au Laser) repose sur la photoionisation des atomes par des faisceaux laser, offrant une sélectivité élevée et une efficacité d'ionisation supérieure à d'autres techniques d'ionisation non spécifiques. Le processus d'ionisation résonante implique l'excitation progressive des électrons de valence par absorption résonante de la lumière laser, suivie de transitions atomiques intenses vers des états excités supérieurs et éventuellement l'ionisation. Les schémas d'ionisation dépendent de facteurs tels que la valeur des transitions atomiques et le nombre d'étapes d'excitation résonante et le type d'ionisation.

Compte tenu des avantages de RILIS,une source laser a été mise en place avec succès auprès d'ALTO, permettant une source spécifique d'ions pour des études avancées.

RIALTO

La source d'ions laser d'ALTO (RIALTO) [55], située au-dessus du séparateur de masse PARRNe, vise à produire des faisceaux d'ions purs en utilisant la technique d'ionisation résonante.

La salle laser est équipée d'un laser "neodymium-doped yttrium aluminum garnet" (Nd:YAG) à haute puissance et doublé en fréquence (532 nm, 100 W), fonctionnant à une cadence de 10 kHz et une largeur d'impulsion (FWHM) d'environ 10 ns. Ce laser pompe trois lasers à colorant à cadence élevée réglés par réseau (540-850 nm), deux de la marque Radiant Dyes [56] et un de la marque Lioptec [57], avec leurs unités de doublage en fréquence par cristal en BBO (Borate de Baryum BaB_2O_4) (270-425 nm), afin de réaliser des schémas d'ionisation à deux et trois étapes.

RIALTO upgrade

Afin d'améliorer les performances de la source d'ions laser à ALTO, nous nous sommes concentrés sur quatre aspects :

- Qualité de l'étape non résonante.
- Système de distribution du faisceau.
- Stabilité du faisceau.
- Capacité à étudier plusieurs éléments en même temps.

Nous avons acquis un laser Nd:YAG à pompage diode (Modèle INNOSLAB, BX 80-2-G [66]) de la marque Edgewave, que nous utilisons exclusivement pour l'ionisation non résonante. Pour le transport de faisceau Nd:YAG, nous avons opté pour une combinaison de lames demi-onde ($\lambda/2$) et de cubes séparateurs de faisceau polarisés. Deux systèmes de stabilisation en position du faisceau sont utilisés dans l'installation.

Nd:YAG laser

Un laser Nd:YAG de type INNOSLAB, modèle BX 80-2-G de la marque Edgewave [66], a récemment été installé à RIALTO. Ce laser présente un faisceau de profil gaussien adapté à l'ionisation.

Système d'asservissement du faisceau

Les faisceaux laser peuvent subir des déplacements spatiaux en raison de facteurs tels que la température, la densité de l'air, les variations de puissance et les effets de chauffage. Maintenir un alignement précis du laser est crucial pour une source d'ions laser, en particulier pour un fonctionnement à long terme dans des zones expérimentales à haut risque et donc inaccessibles.

Pour résoudre ce problème, un système d'asservissement de positionnement de faisceau TEM Messtechnik (Aligna/BeamLock 4D) a été intégré. Il utilise une stabilisation en 4 dimensions pour compenser les variations et maintenir l'alignement du faisceau laser sur une longue distance (~ 20 m).

Production de faisceaux de Ga et Ag

En octobre 2022, une expérience a été menée à ALTO pour mettre en service le système amélioré de RIALTO et mesurer la production de Ga et de Ag. Cette campagne expérimentale marque notamment la première utilisation de la section LEB de l'installation suite aux améliorations apportées à l'avant de la ligne dans le cadre du projet FRISAL.

Pour ioniser le Ga nous avons utilisé un schéma en deux étapes, comprenant une longueur d'onde fondamentale (λ = 574.8 nm) pour la première étape d'excitation (λ = 287.5 nm) et ionisation non résonante avec un laser Nd:YAG.

Pour l'Ag, un schéma à 3 étapes et 3 couleurs, comprenant pour la première étape d'excitation (λ =328,2 nm), la longueur d'onde fondamentale (λ =656,326 nm), Pour la deuxième étape (λ =546,7 nm) et la derniere étape non résonante à λ =532 nm . Lors de la première production d'un faisceau d'argent à ALTO, l'efficacité du schéma d'ionisation a été évaluée à l'aide de banc de test hors ligne (ABU pour Atomic Beam Unit).

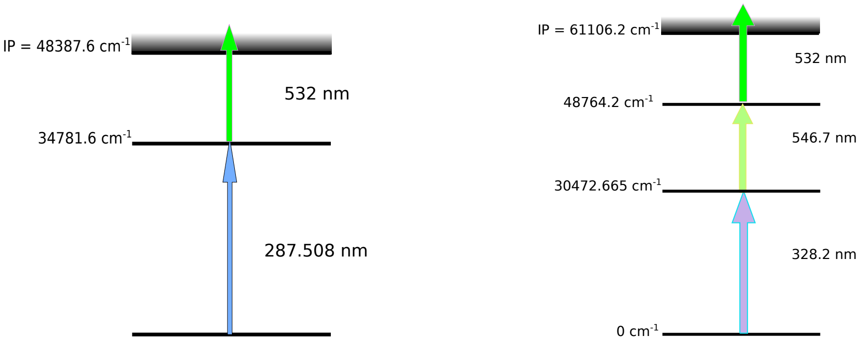

(a) Schèma pour Ga. (b) Schèma pour l'Ag.

Figure 7.4: Schèma d'ionisation d'Ag [89] et Ga[77]

Nous avons effectué un balayage des masses pour le gallium et argent stable afin d'observer l'effet de la source d'ionisation laser

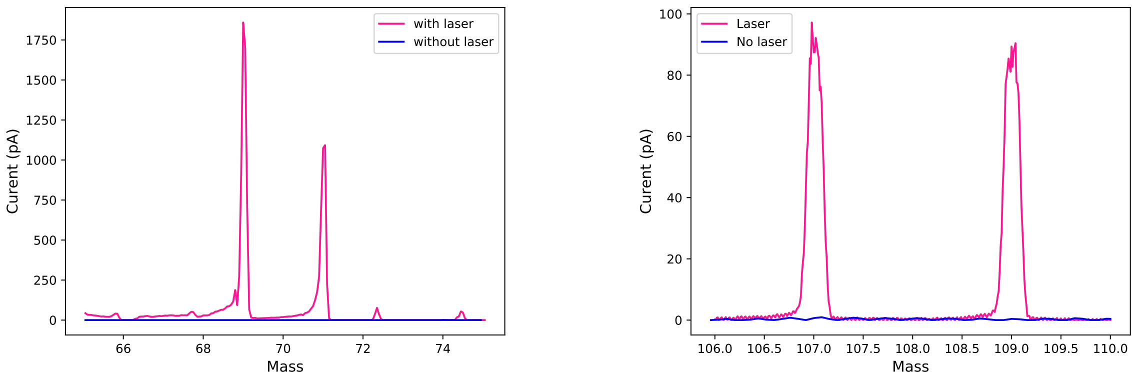

(a) Balayage de masse de Ga.

(b) Balayage de masse de l'Ag.

Figure 7.5: Balayage de masse de l'Ag et Ga stable. Les mesures ont été effectuées sur la cage de Faraday dans l'installation COeCO. La ligne rose montre le courant ionique avec laser, et la ligne bleue montre le courant ions sans laser.

Des mesures de saturation ont été effectuées en variant la puissance du laser et en observant le courant d'ions pour évaluer l'efficacité des transitions. Comprendre la saturation des étapes d'excitation est crucial pour estimer l'impact des variations de puissance du laser sur l'efficacité d'ionisation lors de la production de faisceau d'ions.

Nous avons effectué un test laser ON/OFF sur les gammas de ^{80}Ga, montrant une amélioration de facteur 8. Le spectre γ mesuré avec l'ionisation de surface (violet) est comparé au spectre avec la source d'ionisation laser (rose) à la masse 80 (Figure 7.6).

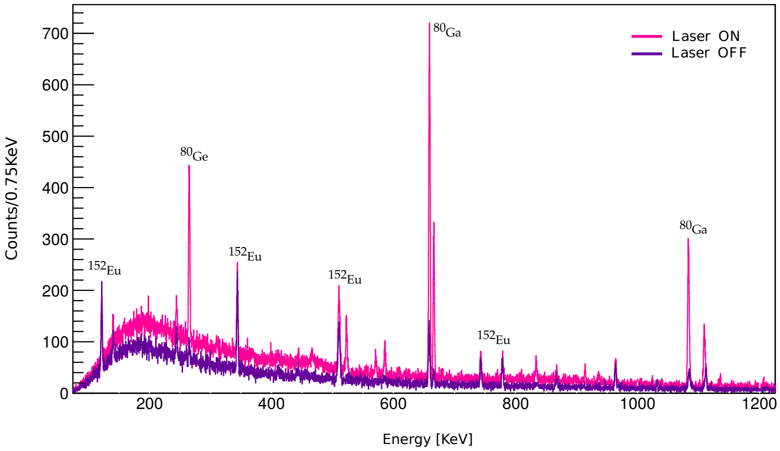

Figure 7.6: Effect laser ON-OFF pour ^{80}Ga.

Production de noyaux radioactifs

Les mesures de production de fission sont cruciales pour comprendre le processus et ont des applications pratiques. Améliorer notre connaissance des productions isotopiques de fission permet une identification précise des isotopes riches en neutrons de masse moyenne. Évaluer et rapporter les productions isotopiques est essentiel pour la planification des expériences nucléaires, l'amélioration des performances et la comparaison avec d'autres installations.

Production de Ga

Les intensités de production de $^{76-85}$Ga (ϕ_n) obtenues dans cette étude sont affichées dans la Figure 7.7. Ces valeurs ont été normalisées par rapport à un faisceau d'électrons de 10 µA pour permettre des comparaisons directes avec la production rapportée en 2019 [84], 2015 [85], et les calculs prévus [81].

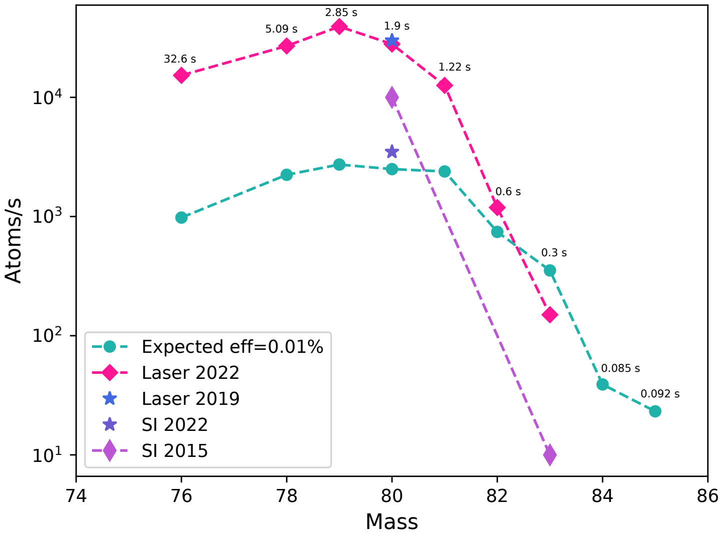

Figure 7.7: Production de Ga.

Conclusions

RIALTO upgrade

Le système laser de la source d'ions laser ALTO a été amélioré avec un second Nd:YAG, un nouveau système de distribution de faisceau et une stabilisation de la position pour deux faisceaux, un UV et un Nd:YAG.

De plus, l'inclusion de deux systèmes de stabilisation de la position du faisceau dans l'installation a amélioré la stabilité du faisceau de RIALTO, réduisant les effets des fluctuations environnementales et garantissant une production plus stable de faisceau d'ions.

Les modifications apportées au système de distribution de faisceau, notamment l'utilisation de lames demi-onde ($\lambda/2$) et de cubes séparateurs de faisceau polarisés, ont permis un contrôle plus précis de la direction et de la polarisation des faisceaux laser, ce qui permet d'améliorer la qualité du faisceau et l'efficacité d'ionisation.

Il est important de noter que grâce à ces améliorations, nous avons désormais la possibilité d'étudier plusieurs éléments simultanément et d'avoir deux schémas d'éléments différents disponibles dans des conditions optimales pour une utilisation en ligne. Auparavant, le changement d'éléments nécessitait une semaine entière de préparation (si le schéma était connu et testé à l'avance). Cela comprend le changement de la solution de colorant, le règlement du laser et l'alignement des faisceaux dans la source d'ions.

Le passage de Ag au Ga été réalisé en moins d'une heure, ce qui est une réalisation remarquable. Cette avancée permet désormais l'utilisation simultanée de faisceaux laser séparés par deux utilisateurs sur la même cible, sans perte de temps. De plus, elle permet la mise en place d'une approche efficace, dans laquelle un schéma laser peut être dédié aux mesures expérimentales tandis qu'un autre faisceau laser reste disponible pour le développement du schéma ou les mesures de production.

Prouction du Ga

La mise en service réussie du nouveau Front-End FRISAL et la mise à niveau de RIALTO sont confirmées par les réalisations de production de Ga sur différents isotopes. Les isotopes de gallium montrent une reproductibilité par rapport à l'expérience de 2019. Pour améliorer la production de Ga, il faut augmenter la puissance à 3240 W, améliorer le transport du faisceau et remplacer le tube d'ionisation en tantale par du niobium pour une plus grande efficacité (facteur 3 à 10 de plus).

Prouction d'Ag

Ce travail a mis en place un schéma de photoionisation résonante en trois étapes pour l'argent et sera utilisé pour la production en ligne d'ions radioactifs d'argent riches en neutrons dans l'installation ALTO. Il est remarquable que l'argent ait été ionisé avec succès pour la première fois dans ALTO en utilisant ce schéma.

La production d'argent a été réalisée à la fois hors ligne et en ligne. Bien qu'aucun test avec de l'argent radioactif n'ait pu être effectué, les mesures en ligne ont reproduit efficacement les mesures de saturation de puissance et l'effet marche/arrêt du laser, ce qui inspire confiance quant à la faisabilité de cette approche pour les futures expériences en ligne. De plus, la production d'argent stable a été réalisée sans rencontrer de difficultés lors de deux périodes distinctes d'utilisation du faisceau.

Perspective

Programme d'Ag radioactif riche en neutrons

Le r-process est crucial pour produire des noyaux riches en neutrons. Une expérience est prévue à ALTO pour mesurer les masses précises des isotopes d'argent près de la fermeture de la couche N=82. L'étude explore l'affaiblissement de l'écart de couche pour Z=50 et son impact sur la nucléosynthèse du r-processus pour A=130. Les isotopes d'argent riches en neutrons seront mesurés, avec un accent sur ceux ayant Z=47 et A> 121. L'expérience utilisera les masses connues des isotopes légers d'argent (A< 121) pour la caractérisation du système. De plus, la probabilité d'émission neutronique retardée β des isotopes d'argent riches en neutrons sera mesurée de N=75 à N=82. Les installations TETRA à ALTO seront utilisées pour ces expériences

La combinaison de la technique RILIS avec la détection de désintégration montre un potentiel pour les futures expériences sur les faisceaux exotiques. Une station de désintégration polyvalente peut séparer les structures isomériques et les états fondamentaux, améliorant la suppression du bruit de fond.

Finalement, la disponibilité d'un faisceau très en vue à ALTO a d'importantes implications scientifiques, car l'Ag a gagné en importance en tant que sujet d'étude dans de nombreuses installations ISOL à travers le monde. ALTO peut désormais entrer dans le domaine compétitif et contribuer aux avancées dans la recherche sur l'Ag riche en neutrons. Ce faisceau offre une opportunité unique de réaliser des mesures précises de masse et des expériences de spectroscopie de désintégration, permettant une compréhension plus approfondie des propriétés nucléaires.

L'avenir de RIALTO

Nouvel Nd:YAG

RIALTO a commandé un troisième laser Nd:YAG avec sortie en vert/UV, qui sera bientôt installé. Cette acquisition permettra d'étendre la gamme de longueurs d'onde en utilisant un laser de pompe UV et une unité de conversion de fréquence triple. Le laser de pompe UV ouvrira l'accès à des schémas d'ionisation nécessitant la Génération de Troisième Harmonique (THG), tels que Zn (213.9 nm) et Sb (217.6 nm), et Ge (265.16). De plus, le nouveau laser fournira une puissance supplémentaire pour améliorer les transitions non résonantes lors de la production d'argent. Il servira également de laser de pompe de secours avec les mêmes paramètres que le laser principal, minimisant les temps d'arrêt en cas de panne ou de maintenance urgente.

Recherche d'un nouveau schéma d'ionisation

En plus de son utilisation actuelle dans le développement de schémas d'ionisation, l'ABU peut également être utilisé pour des mesures spectroscopiques et l'exploration des états autoionisants.

Grâce au sytème amélioré de RIALTO, nous pouvons maintenant exploiter l'ABU pour développer de nouveaux schémas de niveaux. En utilisant le colorant actuel dans le laser Lioptec, le Rhodamine 6G avec de l'éthanol, nous avons accès à une plage de longueurs d'onde d'environ 552 - 600 nm en fondamental et 276 - 300 nm en SHG. L'un de nos objectifs principaux est d'identifier de nouveaux schémas d'ionisation qui pourraient être plus efficaces ou de localiser des états d'auto-ionisation de l'Ag. Nous prévoyons d'explorer différentes situations pour tester nos hypothèses.

Nouveaux schémas d'ionisation avec RIALTO

Avec la mise à niveau du système laser RIALTO, nous avons pour objectif d'explorer la faisabilité du développement de nouveaux faisceaux pour ALTO. Nous avons envisagé les éléments suivants comme candidats : Zn (schéma d'ionisation à 3 étapes et 3 couleurs), Cu (schéma d'ionisation à 2 étapes et 2 couleurs), Sb (schéma d'ionisation à 3 étapes et 3 couleurs), Sn (schéma d'ionisation à 3 étapes et 3 couleurs) et Ge (schéma d'ionisation à 3 étapes et 3 couleurs).

Bibliography

[1] Evaluated nuclear structure data file (ensdf). https://www.nndc.bnl.gov/ensdfarchivals/.

[2] Y Blumenfeld, T Nilsson, and P Van Duppen. Facilities and methods for radioactive ion beam production. *Physica Scripta*, 2013(T152):014023, jan 2013.

[3] Adamian, G. G., Antonenko, N. V., Diaz-Torres, A., and Heinz, S. How to extend the chart of nuclides? *Eur. Phys. J. A*, 56(2):47, 2020.

[4] S. Grévy. High intensity ion guides and purification techniques for low energy radioactive ion beams. *Nuclear Instruments and Methods in Physics Research Section B: Beam Interactions with Materials and Atoms*, 376:200–206, 2016. Proceedings of the XVIIth International Conference on Electromagnetic Isotope Separators and Related Topics (EMIS2015), Grand Rapids, MI, U.S.A., 11-15 May 2015.

[5] K. R. Anton, S. L. Kaufman, W. Klempt, G. Moruzzi, R. Neugart, E. W. Otten, and B. Schinzler. Collinear laser spectroscopy on fast atomic beams. *Phys. Rev. Lett.*, 40:642–645, Mar 1978.

[6] G.D. Alkhazov, A.E. Barzakh, V.P. Denisov, K.A. Mezilev, Yu.N. Novikov, V.N. Panteleyev, A.V. Popov, E.P. Sudentas, V.S. Letokhov, V.I. Mishin, V.N. Fedoseyev, S.V. Andreyev, D.S. Vedeneyev, and A.D. Zyuzikov. A new highly efficient method of atomic spectroscopy for nuclides far from stability. *Nuclear Instruments and Methods in Physics Research Section B: Beam Interactions with Materials and Atoms*, 69(4):517–520, 1992.

[7] G. D. Sprouse and L. A. Orozco. Laser trapping of radioactive atoms. *Annual Review of Nuclear and Particle Science*, 47, Mar 1997.

[8] S.L. Kaufman. High-resolution laser spectroscopy in fast beams. *Optics Communications*, 17(3):309–312, 1976.

[9] VS Letokhov. Comments atomic mol. *Phys*, 7:93, 1977.

[10] G. S. Hurst, M. H. Nayfeh, and J. P. Young. One-atom detection using resonance ionization spectroscopy. *Phys. Rev. A*, 15:2283–2292, Jun 1977.

[11] I. Budinčević, J. Billowes, M. L. Bissell, T. E. Cocolios, R. P. de Groote, S. De Schepper, V. N. Fedosseev, K. T. Flanagan, S. Franchoo, R. F. Garcia Ruiz, H. Heylen, K. M. Lynch, B. A. Marsh, G. Neyens, T. J. Procter, R. E. Rossel, S. Rothe, I. Strashnov, H. H. Stroke, and K. D. A. Wendt. Laser spectroscopy of francium isotopes at the borders of the region of reflection asymmetry. *Phys. Rev. C*, 90:014317, Jul 2014.

[12] R. V. Ambartzumian and V. S. Letokhov. Selective two-step (sts) photoionization of atoms and photodissociation of molecules by laser radiation. *Appl. Opt.*, 11(2):354–358, Feb 1972.

[13] G.D. Alkhazov, L.Kh. Batist, A.A. Bykov, V.D. Vitman, V.S. Letokhov, V.I. Mishin, V.N. Panteleyev, S.K. Sekatsky, and V.N. Fedoseyev. Application of a high efficiency selective laser ion source at the iris facility. *Nuclear Instruments and Methods in Physics Research Section A: Accelerators, Spectrometers, Detectors and Associated Equipment*, 306(1):400–402, 1991.

[14] U Köster. Resonance ionization laser ion sources. *Nucl. Phys. A*, 701:441–451, 2002.

[15] Marcin Turek. Surface ionization of radioactive nuclides - numerical simulations. *Acta Physica Polonica A*, 123:847–850, 05 2013.

[16] Piet Van Duppen, P. Dendooven, M. Huyse, Ludo Vermeeren, Zeid Qamhieh, R. Silverans, and E. Vandeweert. A laser ion source for on-line mass separation. *Hyperfine Interactions*, 74:193–204, 01 1992.

[17] Yuri Kudryavtsev, Józef Andrzejewski, Nathalie Bijnens, Serge Franchoo, Johnny Gentens, Mark Huyse, Andreas Piechaczek, Jurek Szerypo, Ils Reusen, Piet Van Duppen, Paul Van Den Bergh, Ludo Vermeeren, Jan Wauters, and Andreas Wöhr. Beams of short lived nuclei produced by selective laser ionization in a gas cell. *Nuclear Instruments and Methods in Physics Research Section B: Beam Interactions with Materials and Atoms*, 114(3):350–365, 1996.

[18] L. Vermeeren, N. Bijnens, M. Huyse, Y. A. Kudryavtsev, P. Van Duppen, J. Wauters, Z. N. Qamhieh, P. Thoen, E. Vandeweert, and R. E. Silverans. An on-line laser ion source based on resonance photoionization in a gas cell. *Phys. Rev. Lett.*, 73:1935–1938, Oct 1994.

[19] B. A. Marsh. Resonance ionization laser ion sources for on-line isotope separators (invited). *Review of Scientific Instruments*, 85(2):02B923, 2014.

[20] X.F. Yang, S.J. Wang, S.G. Wilkins, and R.F. Garcia Ruiz. Laser spectroscopy for the study of exotic nuclei. *Progress in Particle and Nuclear Physics*, 129:104005, 2023.

[21] Saïd Essabaa and et al. The radioactive beam facility alto. *Nuc. In. Meth. B*, 317, 2013.

[22] David J. Morrissey and Brad M. Sherrill. *In-Flight Separation of Projectile Fragments.* Springer Berlin Heidelberg, 2004.

[23] HIE-ISOLDE Project. `https://hie-isolde-project.web.cern.ch`.

[24] The TRIUMF Isotope Separator and Accelerator (ISAC):. `https://www.triumf.ca/research-program/research-facilities/isac-facilities`.

[25] GANIL. `https://www.ganil-spiral2.eu/`.

[26] IGISOL. `https://www.jyu.fi/science/en/physics/research/infrastructures/accelerator-laboratory/nuclear-physics-facilities/the-exotic-nuclei-and-beams`.

[27] SPES. `https://web.infn.it/spes/index.php`.

[28] P. Van Duppen. *Isotope Separation On Line and Post Acceleration*, pages 37–77. Springer Berlin Heidelberg, Berlin, Heidelberg, 2006.

[29] M. Lindroos. Review of the ISOL-type radioactive beam facilities. In *9th European Particle Accelerator Conference (EPAC 2004)*, 7 2004.

[30] T. Bjørnstad, E. Hagebø, P. Hoff, O.C. Jonsson, E. Kugler, H.L. Ravn, S. Sundell, and B. Vosicki. Recent development of high-temperature metal targets for isolde. *Nuclear Instruments and Methods in Physics Research Section B: Beam Interactions with Materials and Atoms*, 26(1):174–182, 1987.

[31] M. Dombsky, L. Buchmann, J.M. D'Auria, P. McNeely, G. Roy, H. Sprenger, and J. Vincent. Targets and ion sources at the tisol facility. *Nuclear Instruments and Methods in Physics Research Section B: Beam Interactions with Materials and Atoms*, 70(1):125–130, 1992.

[32] Maher Cheikh Mhamed. *Production de noyaux exotiques par photofission,Le projet ALTO : Premiers Résultats.* PhD thesis, Université d'Evry Val d'Essonne, 2006.

[33] William T Diamond. A radioactive ion beam facility using photofission. *Nuclear Instruments and Methods in Physics Research Section A: Accelerators, Spectrometers, Detectors and Associated Equipment*, 432(2):471–482, 1999.

[34] B Roussière and et. al. Release properties of UCx and molten U targets. *Nuclear Instruments and Methods in Physics Research Section B: Beam Interactions with Materials and Atoms*, 194(2):151–163, 2002.

[35] Alto-leb. https://alto.ijclab.in2p3.fr/installation/alto-leb/.

[36] Julien Guillot and et. al. Development of radioactive beams at ALTO: Part 2. influence of the ucx target microstructure on the release properties of fission products. *Nuclear Instruments and Methods in Physics Research Section B: Beam Interactions with Materials and Atoms*, 440:1–10, 2019.

[37] Julien Guillot and et. al. Influence of density and release properties of UCx targets on the fission product yields at ALTO. *Nuclear Instruments and Methods in Physics Research Section B: Beam Interactions with Materials and Atoms*, 468:1–7, 2020.

[38] V.S. Kolhinen and et. al. MLLTRAP: A penning trap facility for high-accuracy mass measurements. *Nuclear Instruments and Methods in Physics Research Section B: Beam Interactions with Materials and Atoms*, 266(19):4547–4550, 2008.

[39] Asénath Étilé. *Etude de la structure nucléaire de noyaux exotiques à ALTO : développements et résultats de deux nouvelles installations*. PhD thesis, Université Paris Sud - Paris XI, December 2014.

[40] D.T. Yordanov and et al. Instrumentation for high-resolution laser spectroscopy at the alto radioactive-beam facility. *Journal of Instrumentation*, 15(06):P06004, jun 2020.

[41] A. Etilé and et. al. Low-lying intruder and tensor-driven structures in ^{82}As revealed by β decay at a new movable-tape-based experimental setup. *Phys. Rev. C*, 91:064317, Jun 2015.

[42] Dmitry Testov. *Effect of shell closure N=50 and N=82 on the structure of very neutron-rich nuclei produced at ALTO. Measurements of neutron emission probabilities and half-lives of nuclei at astrophysical r-process path.* PhD thesis, Université Paris Sud, 2014.

[43] Guillem Tocabens. *Conception et exploitation d'un dispositif pour la spectroscopic d'électrons de conversion β-retardés, application à l'étude de la région riche en neutrons de masse A~100.* PhD thesis, Université Paris-Saclay, December 2022.

[44] Frisal project : Front-end robotisé pour isol alto. https://alto.ijclab.in2p3.fr/en/current-developments/frisal-phase-en/.

[45] James A.R Samson. Photoionization of atoms and molecules. *Physics Reports*, 28(4):303–354, 1976.

[46] A. Temkin. *Autoionization: Recent developments and applications.* Springer New York, 1985.

[47] W. Demtröder. *Atoms, Molecules and Photons.* Springer Berlin Heidelberg, 2010.

[48] NIST Atomic Spectra Database. `https://www.nist.gov/pml/atomic-spectra-database`.

[49] Atomic Line Data: (R.L. Kurucz and B. Bell) Kurucz CD-ROM. `https://lweb.cfa.harvard.edu/amp/ampdata/kurucz23/sekur.html`.

[50] RILIS Database. `http://rilis.web.cern.ch/elements`.

[51] W. Demtröder. *Laser Spectroscopy: Basic Concepts and Instrumentation.* Springer Berlin Heidelberg, 2013.

[52] A.E. Barzakh, V.P. Denisov, D.V. Fedorov, S.Yu. Orlov, and M.D. Seliverstov. A mass-separator laser ion source. *Nuclear Instruments and Methods in Physics Research Section B: Beam Interactions with Materials and Atoms*, 126(1):85–87, 1997. International

Conference on Electromagnetic Isotope Separators and Techniques Related to Their Applications.

[53] V.N. Fedosseev, L.-E. Berg, N. Lebas, O.J. Launila, M. Lindroos, R. Losito, B.A. Marsh, F.K. Österdahl, T. Pauchard, G. Tranströmer, and J. Vannesjö. Isolde rilis: New beams, new facilities. *Nuclear Instruments and Methods in Physics Research Section B: Beam Interactions with Materials and Atoms*, 266(19):4378–4382, 2008. Proceedings of the XVth International Conference on Electromagnetic Isotope Separators and Techniques Related to their Applications.

[54] N. Lecesne. Laser ion sources for radioactive beams. *Review of Scientific Instruments*, 83(2):02A916, 2012.

[55] Ruohong Li and et al. The resonance laser ion source at ipn-atlo. *International Symposium on Exotic Nuclei EXON-2014*, pages 635–644, 2014.

[56] Radiant dyes laser. `https://www.radiant-dyes.com/PDF/Dye_Laser_NarrowScan.pdf`.

[57] LIOPSTAR-HQ. `http://www.liop-tec.com/resources/LiopStar-HQ+2021.pdf`.

[58] Edgewave IS-series. `https://www.edge-wave.de/web/en/produkte/short-pulse-systeme/is-serie/`.

[59] Keming Du, Nianle Wu, Jiandong Xu, J. Giesekus, P. Loosen, and R. Poprawe. Partially end-pumped nd:yag slab laser with a hybrid resonator. *Opt. Lett.*, 23(5):370–372, Mar 1998.

[60] Piet Van Duppen. Laser ion sources for on-line isotope separators. *Nuclear Instruments and Methods in Physics Research Section B: Beam Interactions with Materials and Atoms*, 126(1):66–72, 1997. International Conference on Electromagnetic Isotope Separators and Techniques Related to Their Applications.

[61] Mark Csele. . *Fundamentals of Light Sources and Lasers.* John Wiley and Sons, 2011.

[62] K. Blaum, C. Geppert, H.-J. Kluge, M. Mukherjee, S. Schwarz, and K. Wendt. A novel scheme for a highly selective laser ion source. *Nuclear Instruments and Methods in Physics Research Section B: Beam Interactions with Materials and Atoms*, 204:331–335, 2003. 14th International Conference on Electromagnetic Isotope Separators and Techniques Related to their Applications.

[63] Michael G. Littman and Harold J. Metcalf. Spectrally narrow pulsed dye laser without beam expander. *Appl. Opt.*, 17(14):2224–2227, Jul 1978.

[64] WS6 600 Series. `https://www.highfinesse.com/en/wavelengthmeter/wavelengthmeter-ws-6-600.html`.

[65] Stabilized helium neon laser system model: N-STP-910. `https://www.newport.com/mam/celum/celum_assets/np/resources/N-STP-910_Spec_Sheet.pdf?0`.

[66] Edgewave BX-series. https://www.edge-wave.de/web/en/produkte/short-pulse-systeme/bx-serie/.

[67] Model 577 Pulse/Digital Delay Generator. `https://www.berkeleynucleonics.com/sites/default/files/product-downloads/577_datasheet_v1.1_08-25-2020.pdf`.

[68] Polarizing beamsplitter cube. `https://www.thorlabs.com/thorproduct.cfm?partnumber=CCM1-PBS25-532-HP/M`.

[69] Multi-order half-wave plate. `https://www.thorlabs.com/search/thorsearch.cfm?search=WPMH10M-532`.

[70] E. Hecht. *Optics.* Pearson education. Addison-Wesley, 2002.

[71] What are beamsplitters. `https://www.edmundoptics.com/knowledge-center/application-notes/optics/what-are-beamsplitters`.

[72] Jarom S. Jackson, James L. Archibald, and Dallin S. Durfee. Light splitting with imperfect wave plates. *Appl. Opt.*, 56(4):1062–1068, 2017.

[73] TEM Messtechnik GmbH. *“User Manual uAligna”*.

[74] V.I. Mishin, V.N. Fedoseyev, H.-J. Kluge, V.S. Letokhov, H.L. Ravn, F. Scheerer, Y. Shirakabe, S. Sundell, and O. Tengblad. Chemically selective laser ion-source for the CERN-ISOLDE on-line mass separator facility. *Nuclear Instruments and Methods in Physics Research Section B: Beam Interactions with Materials and Atoms*, 73(4):550–560, 1993.

[75] Sebastian Rothe. *An all-solid state laser system for the laser ion source RILIS and in-source laser spectroscopy of astatine at ISOLDE, CERN.* PhD thesis, Johannes Gutenberg-Universität, 2012.

[76] Nist atomic spectra database. `https://www.nist.gov/pml/atomic-spectra-database`.

[77] U Koester. *Yields and spectroscopy of radioactive isotopes at LOHENGRIN and ISOLDE; Ausbeuten und Spektroskopie radioaktiver Isotope bei LOHENGRIN und ISOLDE.* PhD thesis, Tech. U. Mnchen, Jul 2000.

[78] Isolde yield database. `https://isoyields2.web.cern.ch/Yield_Home.aspx`.

[79] U. KÖSTER and et. al. Fission Yield Measurements with the Isol Method. In *Seminar on Fission*, February 2004.

[80] B. Roussière. *Recherche des premiers états excités 0+ dans les noyaux* ^{108}Cd *et* ^{106}Cd. Other thesis, Paris 6, 1981.

[81] B. Roussière. Préparation des mesures de productions prévues en 2022. `https://atrium.in2p3.fr/nuxeo/nxpath/default/Atrium/Laboratoires/IJCLab/PLATEFORMES/ALTO/PRODUCTION/Production%20ALTO-LEB/Cibles%20exploitattion/Productions@view_documents?tabIds=%3A&conversationId=0NXMAIN1`, 2022.

[82] Alfredo Ferrari, Paola R. Sala, Alberto Fasso, and Johannes Ranft. FLUKA: A multi-particle transport code (Program version 2005). 10 2005.

[83] B. Roussière, O. Bajeat, N. Barré, Camille Bourgeois, F. Clapier, E. Cottereau, C. Donzaud, M. Ducourtieux, S. Essabaa, D. Guillemaud-Mueller, Fadi Ibrahim, C. Lau, F. Blanc, H. Lefort, Chih-Fu Liang, Alex Mueller, J. Obert, N. Pauwels, J.C. Potier, and A. Wojtasiewicz. Release of kr, ag, sn, i and xe from ucx targets. *Nuclear Instruments and Methods in Physics Research Section B: Beam Interactions with Materials and Atoms*, 246:288–296, 05 2006.

[84] Ren Li. *First attempt toward a quasi-Pandemonium free β-delayed spectroscopy of 80Ge using PARIS at ALTO.* PhD thesis, Université Paris-Saclay, 2022.

[85] A. Gottardo and et. al. Unexpected high-energy γ emission from decaying exotic nuclei. *Physics Letters B*, 772:359–362, 2017.

[86] M. Arnould, S. Goriely, and K. Takahashi. The r-process of stellar nucleosynthesis: Astrophysics and nuclear physics achievements and mysteries. *Physics Reports*, 450(4):97–213, 2007.

[87] G. Lorusso and et. al. β-decay half-lives of 110 neutron-rich nuclei across the $n = 82$ shell gap: Implications for the mechanism and universality of the astrophysical r process. *Phys. Rev. Lett.*, 114:192501, May 2015.

[88] S. Rothe, B. A. Marsh, C. Mattolat, V. N. Fedosseev, and K. Wendt. A complementary laser system for ISOLDE RILIS. *J. Phys. Conf. Ser.*, 312:052020, 2011.

[89] Valentin Fedosseev and et al. Study of short-lived silver isotopes with a laser ion source. *Z. Phys.*, 353:9–10, 01 1995.